

OPTIMIZATION OF ELECTROMAGNETIC DEVICES AND MATERIALS

By

Kazuko Fuchi

A DISSERTATION

Submitted to
Michigan State University
in partial fulfillment of the requirements
for the degree of

DOCTOR OF PHILOSOPHY

Mechanical Engineering

2012

ABSTRACT

OPTIMIZATION OF ELECTROMAGNETIC DEVICES AND MATERIALS

By

Kazuko Fuchi

Topology optimization is a computational design methodology that is used to find topologies of optimal design, that match design goals. Application of topology optimization in the area of electromagnetics is extremely interesting, since for many electromagnetic design problems the topology of inclusion structures in materials or components in devices can have a dramatic effect on the interaction of the designed structure with the electromagnetic waves. The success of the use of topology optimization for design of metamaterials, antennas, waveguides, etc. reported in literature suggests the importance of research into effective uses of topology optimization in electromagnetic design problems.

The purpose of this dissertation is to investigate efficient electromagnetic analysis methods that can be combined with the method of topology optimization, as well as to develop a new way of using topology optimization to design electromagnetic devices with transformable complex surface geometry, using the concept of origami.

The first part of the dissertation focuses on the investigation of a topology optimization framework for design of periodic structures for electromagnetic applications, using a rigorous and efficient finite element analysis method. The second part introduces a topology optimization based design method for origami folding patterns. To illustrate its use, the origami design method is employed to design frequency selective surfaces for electromagnetic applications, that can transform in their surface geometry to alter their working frequency through folding and unfolding.

To my parents, Hiroyuki Fuchi and Kyoko Makino

ACKNOWLEDGMENTS

I have been supported and encouraged by many people throughout my time at Michigan State University. I would like to acknowledge those who have directly helped me through my Ph.D. program.

Foremost, I would like to express my deepest gratitude to my academic advisor, Prof. Alejandro R. Diaz. He has given me all that I could asked for, and far beyond. He has taken me around the world for professional meetings; he has taught me everything about research and being an academic that I know now; and he has been an exceptional friend.

The best thing about my research project was its multidisciplinary nature. I had the honor to work with Prof. Edward Rothwell from electrical engineering, who has kept me ecstatic with his numerous insightful and creative suggestions. I am very appreciative of the members of the Metamaterials Group, Dr. Raoul Ouedraogo and Junyan Tang for the shared enthusiasm towards our collaborative work, and Khoa Nguyen and Benjamin Crowgey for their help on parts of the project. Extended thanks to my fellow students, John Tam, Isil Berkun, Xiankai Song, Tingli Cai, and Smruti Panigrahi for their continuous encouragement and invaluable friendship. Special thanks to Prof. Alan Haddow, who was my mentor for my first TA assignment, Prof. Jongeun Choi and Prof. Seungik Baek, who agreed to serve on my Ph.D. committee, and the graduate coordinator, Prof. Andre Benard, for their generous support and helpful discussions. My sincere gratitude goes to my collaborators, Prof. Shinji Nishiwaki and Prof. Takayuki Yamada, who have introduced me to a new topology optimization method and stimulated me.

I am grateful to Prof. Martin Berz for offering me a tremendous amount of help getting adopted to the life in the US, my mother, Prof. Kyoko Makino, for being an extraordinary

role model and an inspiration, and my father, Dr. Hiroyuki Fuchi, for always understanding me and motivating me towards a meaningful life. Finally, my boyfriend, Eric Wolf deserves my loving thanks for being on my side and leading me to becoming a happier and better person, and the Wolf family for making me feel at home.

TABLE OF CONTENTS

List of Tables	ix
List of Figures	xi
Chapter 1 Introduction	1
Chapter 2 Finite Element Formulation for Time Harmonic Electromagnetic Waves	7
2.1 Constitutive Equations	7
2.2 Analysis of Periodic Media	9
2.2.1 Two-dimensional domain, 1-D periodicity	9
2.2.2 Three-dimensional domain, 2-D periodicity	10
2.3 Finite Element Mesh Truncation Techniques	11
2.3.1 Absorbing boundary condition	12
2.3.2 Perfectly matched layer	13
2.3.3 Plane wave expansion	14
2.4 Finite Element Formulation	17
Chapter 3 Topology Optimization of 2D Periodic Dielectric Structures .	18
3.1 Problem Setup	19
3.2 Level Set Approach	20
3.2.1 Material distribution	20
3.2.2 Optimization problem	21
3.2.3 Numerical examples	24
3.2.3.1 Example 1	25
3.2.3.2 Example 2	26
3.2.4 Conclusion	29
3.3 Density Approach	29
3.3.1 Material distribution	29
3.3.2 Optimization problem	30
3.3.3 Optimality condition	31
3.3.4 Sensitivity analysis	32
3.3.5 Influence of parameter p	33
3.3.6 Numerical examples	34

3.3.6.1	Example 1	35
3.3.6.2	Example 2	38
3.3.6.3	Example 3	40
3.3.7	Designs with parallel bands	44
3.3.8	Conclusion	48
Chapter 4	Topology Optimization of 3D Periodic Structures	50
4.1	Problem Setup	50
4.2	Material distribution	52
4.3	Optimization problem	53
4.3.1	Sensitivity analysis	54
4.3.2	Projection of the effective density	56
4.3.3	Numerical example	56
4.3.4	Conclusions	61
Chapter 5	Origami Tunable Surfaces for Electromagnetic Applications	62
5.1	Origami Tunable Frequency Selective Surfaces	63
5.1.1	Miura-ori	63
5.1.2	Performance evaluation	65
5.1.3	Choice of conducting element types	67
5.1.3.1	Concentric double ring copper prints	67
5.1.3.2	Cross-shaped copper prints	69
5.1.3.3	Summary	70
5.1.4	Angle dependency	71
5.1.5	Polarization dependency	71
5.1.6	Experiment	74
5.1.7	Conclusions	77
5.2	Origami Tunable Metamaterials	77
5.2.1	Design of an origami tunable metamaterial	78
5.2.2	Demonstration of tuning of a metamaterial	80
5.2.3	Principle of operation	84
5.2.4	Experiment	92
5.2.5	Conclusions	94
Chapter 6	Topology Optimization for Origami Design	98
6.1	Construction of the Ground Structure	100
6.2	Crease Type Assignment and a Folded State	102
6.3	Foldability Conditions	104
6.4	Optimization of Origami Design	105
6.4.1	Geometric properties	106
6.4.2	Objective function	106
6.4.3	Optimization problem	107
6.4.4	Sensitivity analysis	110
6.5	Numerical examples	112

6.5.1	Example 1	113
6.5.2	Example 2	115
6.6	Application: design of polarization insensitive tunable FSS	117
6.7	Conclusions	120
Chapter 7	Conclusions	122
Chapter A	Finite Element Equations for 2D Periodic Structures	126
Chapter B	Finite Element Equations for 3D Periodic Structures	132
Bibliography	141

LIST OF TABLES

Table 3.1	Parameters for example 1	25
Table 3.2	Parameters for example 2	26
Table 3.3	Parameters used in Example 1	35
Table 3.4	Parameters used in Example 2	38
Table 3.5	Parameters used in Example 3	41
Table 3.6	Parameters used for the angle dependency	47
Table 4.1	Parameters used in the example	58
Table 5.1	Parameters used in sample F-band design	81
Table 5.2	Resonance frequencies found using HFSS	83

LIST OF FIGURES

Figure 1.1	Design of an SRR	2
Figure 2.1	A two-dimensional representative cell	10
Figure 2.2	A three-dimensional representative cell	11
Figure 2.3	PML setup for 1-D and 2-D periodic structures	13
Figure 3.1	Design Domain	19
Figure 3.2	Optimal structure and the field distribution for example 1. For interpretation of the references to color in this and all other figures, the reader is referred to the electronic version of this thesis (or dissertation).	26
Figure 3.3	Optimal structure and the field distribution for example 2.	27
Figure 3.4	Frequency sweep for the optimum structure for example 2.	27
Figure 3.5	A known band-gap structure and the frequency sweep.	28
Figure 3.6	Example 1. Optimum solution and iteration history	36
Figure 3.7	Example 1. Optimum solution with vacuum background material . .	37
Figure 3.8	Example 2. Solution and its wavelength sweep	39
Figure 3.9	Example 3. Initial design and optimum solution after postprocessing	41
Figure 3.10	Example 3. Wavelength and angle sweeps ($N_m = 10$)	42
Figure 3.11	Example 3. Angle sweep computed using one mode only ($N_m = 0$) .	43

Figure 3.12	Example 3. Optimum structure starting from a homogeneous material distribution	44
Figure 3.13	Wave propagation through vertical and inclined bands	45
Figure 3.14	Optimization using slanted bands for the initial guess	46
Figure 3.15	Angle dependency of the path length d_L	47
Figure 4.1	Design Domain	51
Figure 4.2	Projection function	57
Figure 4.3	Optimal solution and iteration history	59
Figure 4.4	Processed solutions	60
Figure 5.1	Miura-ori	64
Figure 5.2	Unit cell of Miura-ori	64
Figure 5.3	Analysis setup	66
Figure 5.4	Concentric ring conducting element	67
Figure 5.5	Simulated transmission coefficient $ S_{21} $ for concentric rings at normal incidence	68
Figure 5.6	Skewed cross-shaped conducting element	69
Figure 5.7	Simulated (Sim.) and measured (Exp.) transmission coefficient $ S_{21} $ at normal incidence	70
Figure 5.8	Simulated and measured transmission coefficient $ S_{21} $ at oblique incidence at $\theta=30^\circ$	72
Figure 5.9	Simulated and measured resonance frequencies, f_{res} in GHz	73
Figure 5.10	Fabricated origami tunable FSS	74

Figure 5.11	Experiment setup for normal incidence	75
Figure 5.12	Experiment setup for oblique incidence at $\theta = 30^\circ$	76
Figure 5.13	Corrugated sheet with SRRs, $\alpha = 0^\circ$	78
Figure 5.14	Corrugated sheet with SRRs, $\alpha = 10^\circ$	79
Figure 5.15	Origami metamaterial unit cell design	80
Figure 5.16	Transmission coefficient, $ S_{21} $	81
Figure 5.17	Reflection coefficient, $ S_{11} $	82
Figure 5.18	Equivalent circuit of an SRR	85
Figure 5.19	Electric field magnitude in one unit cell for $\alpha = 0^\circ$	86
Figure 5.20	Electric field magnitude in one unit cell for $\alpha = 2^\circ$	86
Figure 5.21	Electric field magnitude in one unit cell for $\alpha = 8^\circ$	87
Figure 5.22	Electric field magnitude in one unit cell for $\alpha = 10^\circ$	87
Figure 5.23	Geometry of offset parallel conducting strips	89
Figure 5.24	Geometry of unfolded origami metamaterial unit cell	89
Figure 5.25	Relative change in resonance frequency (dashed curves are best-fit lines)	90
Figure 5.26	Derivative of relative change in resonance frequency	91
Figure 5.27	Two halves of fabricated origami metamaterial unit cell with the unit cell width $w = 6.85$ mm	93
Figure 5.28	Origami metamaterial unit cell placed into an F-band waveguide sample holder	93

Figure 5.29	Measured transmission coefficients for an origami metamaterial unit cell placed into an F-band waveguide	95
Figure 5.30	Resonance frequency of an origami metamaterial unit cell placed into an F-band waveguide	96
Figure 5.31	Transmission coefficients for an origami metamaterial unit cell placed into an F-band waveguide from HFSS simulations	97
Figure 6.1	Origami grid systems	101
Figure 6.2	Variations of ground structures	101
Figure 6.3	Flat and folded states of a single-vertex crease	103
Figure 6.4	Single-vertex crease	105
Figure 6.5	Objective function f	107
Figure 6.6	Flowchart of foldline elimination algorithm	111
Figure 6.7	Labeled vertices	113
Figure 6.8	Candidates of fixed folding angles	114
Figure 6.9	Design 1, Example 1	114
Figure 6.10	Design 2, Example 1	114
Figure 6.11	Design 1, Example 2	116
Figure 6.12	Design 2, example 2	116
Figure 6.13	Conducting decoration for FSS	118
Figure 6.14	Transmission coefficient	119
Figure 6.15	Transmission coefficient for the two-layer design	120
Figure B.1	Brick element	137

Chapter 1

Introduction

Topology optimization is a computational design methodology that is used to find topologies of optimal designs that match design goals. It was first introduced in the context of structural design by Bendse and Kikuchi in [1]. Optimal topologies of structures are found through indicator functions, used to represent the effective “density” of a material in each element in the finite element formulation. In [1] effective material properties of each element are computed using a homogenization method and used in the constitutive equations. Within the last two decades, the use of topology optimization has been extended to material design [2] with target properties involving many different physics [3], including thermal [4] and fluid mechanics [5] [6] [7], acoustics [8] [9], photonics and electromagnetics [10]-[26].

Application of topology optimization in the area of electromagnetics is extremely interesting, since for many electromagnetic design problems the topology can have a dramatic effect on the interaction of the designed structure with the electromagnetic waves. An example of such instance is design of metamaterials. Metamaterials are engineered materials composed of metallic or dielectric inclusions within a unit cell of a periodic array, and they exhibit

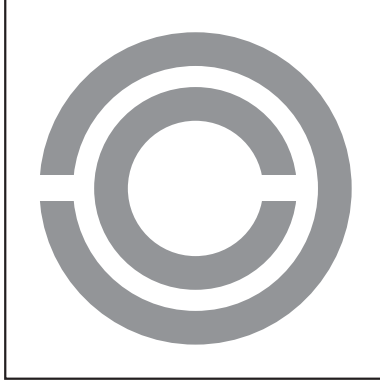


Figure 1.1: Design of an SRR

extraordinary electromagnetic properties. A particular type of metamaterial is known to exhibit negative index of refraction, a property that is not possessed by any natural occurring material. The negative index of refraction material is theorized by Pendry in [27], and a composite design in the radio frequency (RF) range was proposed by Smith [28] and fabricated and tested in [29] where the possibility of synthesizing such materials was demonstrated.

In [28] and [29], a combination of metallic elements; a wire for negative electric permittivity and a split ring resonator (SRR) for negative magnetic permeability, is used to achieve a negative index of refraction. One example of SRRs is the concentric rings with gaps, shown in Fig.1.1. The topology of such an element is of crucial importance, and a small variation to its topology could alter the design's electromagnetic behavior dramatically. For instance, filling the gaps of the SRRs and closing the rings would create a short, and the negative magnetic permeability will no longer be observed. The ability to find the topology of one design with such a unique character is of significant value, as the design can be modified through e.g., parametric or shape optimization, to be incorporated into various applications. In case of the negative index refraction metamaterial in [28] and [29], the topology of the original design was found through physical insights. Topology optimization can be an effi-

cient alternative to finding the starting point of a design process. The work done by Diaz and Sigmund in [19] revealed that metamaterials with negative permeability can be designed via topology optimization, and not all the negative permeability elements have to have a similar geometry as the SRRs.

A popular choice of a design optimization algorithm for electromagnetic problems is a genetic algorithm (GA). Its main advantage is simplicity in implementation, especially for design of advanced electromagnetic devices that requires complex analysis. An introduction to GA for electromagnetic problems and details on the implementation of sample problems are provided in [30]. In [31] Ouedraogo et al. use a GA-based topology optimization method to design a miniaturized antenna. A rectangular section placed above a loop antenna is treated as a design domain, which is divided into rectangular subdomains. Each subdomain is assigned a 1 or 0, which indicates whether copper should be placed(1) or not(0). A combination of 1's and 0's constitutes a chromosome, and a best fit chromosome is selected by means of natural selection through mating, mutation and selection of best performing chromosomes at each iteration. Similar approaches have been used to design frequency selective surfaces, metamaterials and antennas in [32]-[34]. A notable disadvantage of designing electromagnetic devices using GA-based topology optimization is that many iterations are necessary to obtain an acceptable design. Moreover, the stopping criteria are not based on optimality conditions, and the solution is not guaranteed to be optimal.

Rigorous topology optimization methods using gradient-based algorithms have also been used to design electromagnetic devices in [10]-[26]. Gradient-based topology optimization methods can lead to faster convergence, and solutions satisfy optimality conditions. The challenge in using gradient-based methods is the computation of sensitivity of the perfor-

mance with respect to the design. Special care needs to be taken in choosing the design control and performance measure, and analysis methods that allow for efficient computation of sensitivity need to be selected. Finite element methods (FEM) and finite difference time domain (FDTD) methods are the two common analysis methods that have been used for analysis in the frequency domain and time domain, respectively, when using topology optimization as the design method. Earlier works employ the finite element method for the availability of an efficient sensitivity analysis method based on an adjoint variable problem formulation. A typical choice of the design variable is an indicator function used to describe the constituent dielectric or conducting material distributed within the design domain. Examples of the use of topology optimization in conjunction with the finite element analysis include the design of patch antenna substrates by Kiziltas et al. [11], photonic waveguides by Jensen and Sigmund [12], [14], and periodic structures for transmission power control by Nomura et al. [20]. In those works the density function describing the dielectric material distribution is defined over two-dimensional domains and used to control the design through an interpolation scheme. Aage et al. [25] and Erentok and Sigmund [26] used a similar formulation but with the density function defined over a three dimensional domain describing the distribution of conducting material for design of antennas. Development of the adjoint variable method for the sensitivity analysis for FDTD in [35]-[37] let us to choose FDTD as an analysis method when appropriate. In [16] Nomura et al. designed dielectric antennas via topology optimization using a density function as the design variable that describes the dielectric distribution within a 3D design domain, and the FDTD method to find the electric and magnetic fields, which are used in the performance measure.

Increasing demand for an improved performance in advanced electromagnetic devices

and materials indicates the importance of the development of topology optimization methods suited for electromagnetic design problems. To work with state of the art systems, an efficient use of the available computational resources is essential. The purpose of this dissertation is to investigate efficient electromagnetic analysis methods that can be combined with the method of topology optimization, as well as the effective use of topology optimization in solving electromagnetic design problems e.g., a good choice of design variables.

This dissertation consists of two parts. Chapters 2-4 focus on the investigation of a topology optimization framework for design of periodic structures for electromagnetic applications, using a rigorous and efficient finite element analysis method. Chapters 5-6 discuss a new design method that incorporates topology optimization and the concept of origami for design of electromagnetic devices involving a complex 3D geometry. A short description of each chapter is given below.

In chapter 2, the finite element framework for the electromagnetic analysis is discussed. The focus is on the analysis of the electromagnetic wave propagation through periodic media. The discussion extends to the implementation of a rigorous and efficient mesh truncation technique based on plane wave expansions.

In chapter 3, topology optimization problems for design of two dimensional periodic dielectric structures are discussed. Two variations of the topology optimization problem solved in [20] are solved using alternative formulations. The goal of the problem is to find periodic dielectric structures that exhibit desired electromagnetic wave transmission/reflection characteristics in the frequency domain. The first variation uses a level set function for the representation of the material distribution, and the second variation uses a different type of mesh truncation method in the finite element formulation.

In chapter 4, topology optimization problems for design of three dimensional periodic dielectric structures are discussed.

In chapter 5, a new approach to designing tunable electromagnetic devices is introduced, which makes use of a transformation of complex surface geometry through folding. Sample designs of frequency selective surfaces (FSSs) that can be tuned in the working frequency through a folding and unfolding motion are provided.

In chapter 6, a method to design origami folding patterns based on topology optimization is introduced. The mathematics of origami is used to carry out the analysis of the transformation of a foldable sheet from its flat configuration to the folded configuration. The design method follows the “ground structure” approach of structural topology optimization, where optimal folding patterns are found by assigning presence and type of folds to a set of lines drawn on a two-dimensional domain. The origami design method is then applied to the design of origami-based tunable FSSs. Folding patterns with desired geometric properties for the design of tunable FSSs are obtained using the origami design method, and conducting elements are added as a decoration to the foldable surface to achieve FSSs that can be folded and unfolded to tune the working frequency.

Chapter 2

Finite Element Formulation for Time Harmonic Electromagnetic Waves

Finite element methods can be used to analyze many complex systems and to efficiently compute the sensitivity of the performance of the system with respect to the design, which is essential in topology optimization. In this chapter a finite element formulation for the analysis of electromagnetic wave propagation in the frequency domain is discussed, with an emphasis on the mesh truncation method based on a plane wave expansion for periodic problems. There are books available on finite element analysis of time harmonic electromagnetic waves with details of the formulation and implementation, for example, refer to [38]-[40].

2.1 Constitutive Equations

The electromagnetic wave behavior is governed by Maxwell's equations:

$$\nabla \times \mathbf{E} = -\frac{\partial \mathbf{B}}{\partial t} \quad (2.1)$$

$$\nabla \times \mathbf{H} = \frac{\partial \mathbf{D}}{\partial t} + \mathbf{J} \quad (2.2)$$

$$\nabla \bullet \mathbf{D} = \rho \quad (2.3)$$

$$\nabla \bullet \mathbf{B} = 0 \quad (2.4)$$

$$\nabla \bullet \mathbf{J} = -\frac{\partial \rho}{\partial t} \quad (2.5)$$

where \mathbf{E} and \mathbf{H} are the electric and magnetic fields, \mathbf{D} and \mathbf{B} are the electric and magnetic flux density, \mathbf{J} is the electric current density, and ρ is the electric charge density.

When the time dependency is assumed to take the form $\exp(j\omega t)$, Maxwell's equations reduce to vector wave equations

$$\begin{aligned} \nabla \times \mathbf{E} + j\omega\mu\mathbf{H} &= 0 \\ \nabla \times \mathbf{H} - j\omega\epsilon\mathbf{E} &= 0 \end{aligned} \quad (2.6)$$

where $j = \sqrt{-1}$ and ω is the angular frequency. Relevant material properties are described by μ and ϵ , which denote magnetic permeability and electric permittivity, respectively. These equations can be decoupled and solved as a problem of finding either the electric field or magnetic field. If the electric field is taken as unknown, the governing equation becomes

$$\nabla \times \left(\frac{1}{\mu_r} \nabla \times \mathbf{E} \right) - k_0^2 \left(\epsilon_r - \frac{j\sigma}{\omega\epsilon_0} \right) \mathbf{E} = 0 \quad (2.7)$$

where k_0 , σ , ϵ_r and μ_r are the wavenumber in vacuum, electrical conductivity, relative

permittivity and relative permeability such that $\epsilon = \epsilon_r \epsilon_0$ and $\mu = \mu_r \mu_0$ with

$$\begin{aligned}\epsilon_0 &\approx 8.854 \times 10^{-12} F/m \\ \mu_0 &\approx 4\pi \times 10^{-7} A \cdot m\end{aligned}\tag{2.8}$$

For a polarized wave, Maxwell's equations can be simplified to a scalar Helmholtz equation. For a TM^z (transverse magnetic to z) polarization, the z -component of the electric field E_z can be taken as the unknown variable and found by solving the Helmholtz equation

$$\nabla^2 E_z + k_0^2 \epsilon_r E_z = 0\tag{2.9}$$

Other electric field components can be expressed in terms of E_z and found by postprocessing.

2.2 Analysis of Periodic Media

Numerical analysis of electromagnetic wave propagation through periodic media has a great importance as its applications are found in various areas such as modeling of radar, communication and sensing systems as well as design of engineered materials such as metamaterials. Analysis setup of structures with 1-D and 2-D periodicity are described here.

2.2.1 Two-dimensional domain, 1-D periodicity

A dielectric medium with a periodicity in one direction (1-D periodicity) can be described by a distribution of electric permittivity ϵ in a two-dimensional representative domain Ω shown

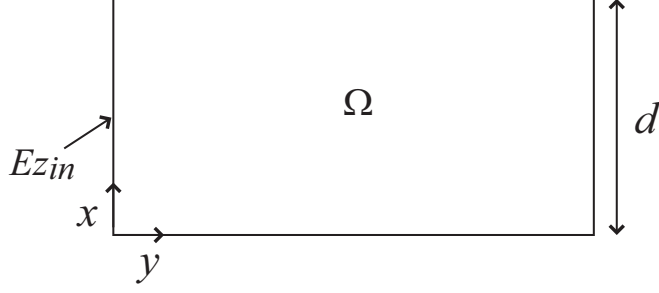


Figure 2.1: A two-dimensional representative cell

in Fig.2.1. The material is assumed periodic in the x -direction with a tiling vector $\mathbf{e} = (d, 0)$.

A transverse magnetic polarization can be assumed with the electric field component E_z taken as the unknown variable. The constitutive equation is the scalar Helmholtz equation in Eq.2.9. To describe a field distribution in a periodic medium with a tiling vector $\mathbf{e} = (d, 0)$, E_z is constrained to follow a Bloch-Floquet condition:

$$E_z(x + md, y) = E_z(x, y)e^{-jm\alpha_0 d}, \quad m \in \mathbb{Z} \quad (2.10)$$

where $\alpha_0 = k_0 \sin \theta$ is the x -component of the propagation vector \mathbf{k} of the incident field $E_{zin} = \exp(-j\alpha_0 x)$.

2.2.2 Three-dimensional domain, 2-D periodicity

A medium with a periodicity in two directions (2-D periodicity) can be described by a distribution of constituent materials in a three-dimensional representative domain Ω shown in Fig.2.2. The structure is periodic in the x - and y -directions with tiling vectors $\mathbf{e}_x = (Tx, 0, 0)$ and $\mathbf{e}_y = (0, Ty, 0)$. Constituent materials are described by values of electric permittivity ϵ , magnetic permeability μ and conductivity σ .

For the 2-D periodic structure, the full-wave analysis is necessary. The electric field

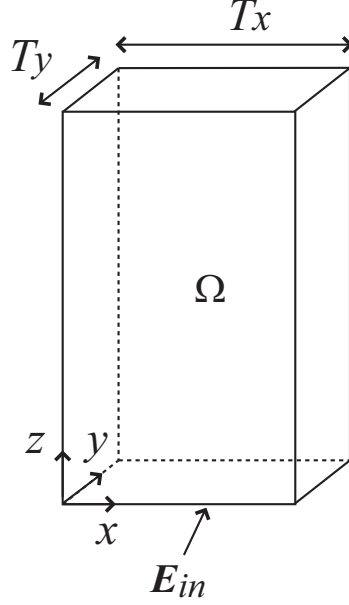


Figure 2.2: A three-dimensional representative cell

formulation of Maxwell's equations can be adopted, and the vector wave equation in Eq.2.7 can be solved for the electric field $\mathbf{E} = E_x\hat{\mathbf{x}} + E_y\hat{\mathbf{y}} + E_z\hat{\mathbf{z}}$. The Bloch-Floquet condition for the electric field in this case is

$$\mathbf{E}(x + mT_x, y + nT_y, z) = \mathbf{E}(x, y, z) \exp(-jm\alpha_0T_x - jn\beta_0T_y), \quad m, n \in \mathbb{Z} \quad (2.11)$$

where α_0 and β_0 are x - and y -components of the propagation vector \mathbf{k} of the incident field $\mathbf{E}_{in} = \exp[-j(\alpha_0x + \beta_0y)]$.

2.3 Finite Element Mesh Truncation Techniques

In the numerical formulation discussed above, an incident electric field is applied at the input boundary and exits at the output boundary, where no physical boundary exists. To avoid

artificial reflections at the input and output boundaries, a mesh truncation technique with appropriate boundary conditions must be used. Some of the frequently used mesh truncation techniques are discussed in [39].

2.3.1 Absorbing boundary condition

A relatively simple method is to use an absorbing boundary condition, in which boundary conditions ensure that any plane wave normally incident to the boundaries is absorbed.

Absorbing boundary condition is formulated as an approximation to Sommerfeld radiation condition as

$$\hat{n} \times (\nabla \times \mathbf{E}) + jk_0 \hat{n} \times (\hat{n} \times \mathbf{E}) \approx 0 \quad (2.12)$$

where \hat{n} is the unit vector normal to the truncation boundary.

When choosing absorbing boundary condition as the mesh truncation technique, the corresponding (input and output) boundaries must be placed far enough from scatterer or sources inside of the analysis domain. A rule of thumb is to place the input or output boundary at least a half wavelength from any scatterer or sources.

For the scalar formulation with the E_z as the unknown variable, Eq.2.12 can be written explicitly as

$$\hat{n} \bullet E_z + jk E_z = jk (1 + \cos \theta) E_{zin} \quad (2.13)$$

at the input boundary, with the incident electric field E_{zin} and

$$\hat{n} \bullet E_z + jk E_z = 0 \quad (2.14)$$

at the output boundary.

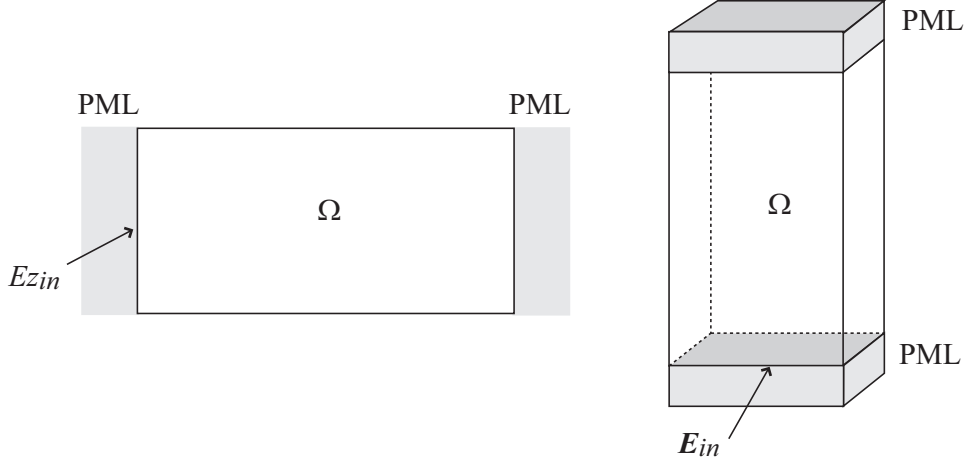


Figure 2.3: PML setup for 1-D and 2-D periodic structures

2.3.2 Perfectly matched layer

Another commonly used mesh truncation technique is to place layers of theoretical materials called perfectly matched layers (PMLs) at boundaries. Examples of PML setups for 1-D and 2-D periodic structures are illustrated in Fig.2.3, where PMLs are placed at the input and output boundaries, shown in gray.

A PML is a theoretical material designed so that reflection is reduced for a wide range of frequencies, polarizations and angles of incidence. Reduction of absolute value of reflection coefficient

$$|R(\theta)| = \exp \left[-2k_x \int_0^L s(z) dz \cos \theta \right] \quad (2.15)$$

can be achieved by increasing the integral $\int_0^L s(z) dz$. For analysis with a wide range of frequencies, choosing

$$s(z) = \frac{\sigma(z)}{\omega \epsilon} \quad (2.16)$$

will eliminate the frequency dependency of the PML. PMLs can be combined with a perfect electric conductor boundary condition

$$\hat{n} \times \mathbf{E} = 0 \quad (2.17)$$

at the outer ends of the PML regions to truncate the mesh. In the case of a TM polarized formulation with E_z as the variable, Eq.2.17 can be written simply as:

$$E_z = 0 \quad (2.18)$$

2.3.3 Plane wave expansion

A rigorous mesh truncation technique is to use a plane wave expansion at the truncation boundaries, a method discussed in [41] and used to solve an inverse problem.

In this approach, the electric field \mathbf{E} at the input boundary is expressed as a combination of the incident and reflected field as

$$\mathbf{E}(x, y, z_{in}) = \mathbf{E}_{in} + \mathbf{E}_{ref} \quad (2.19)$$

where the incident field is written in terms of the propagation vector $\mathbf{k}_0 = \alpha_0 \hat{\mathbf{x}} + \beta_0 \hat{\mathbf{y}} + \gamma_0 \hat{\mathbf{z}}$ and a constant unit vector $\hat{\mathbf{p}}$ along the polarization direction of the electric field as

$$\mathbf{E}_{in} = \exp \left\{ -j \left[\alpha_0 x + \beta_0 y + \gamma_0 (z - z_{in}) \right] \right\} \hat{\mathbf{p}} \quad (2.20)$$

The reflected field is expressed as a Fourier series as

$$\mathbf{E}_{ref} = \sum_{m=-\infty}^{+\infty} \sum_{n=-\infty}^{+\infty} \mathbf{r}_{mn} \exp [j\gamma_{mn} (z - z_{in})] \exp [-j (\alpha_m x + \beta_n y)], \quad n, m \in \mathbb{Z} \quad (2.21)$$

At the output boundary, there is only the transmitted field

$$\mathbf{E}(x, y, z_{out}) = \mathbf{E}_{tr} \quad (2.22)$$

which is also expressed as a Fourier series as

$$\mathbf{E}_{tr} = \sum_{m=-\infty}^{+\infty} \sum_{n=-\infty}^{+\infty} \mathbf{t}_{mn} \exp[-j\gamma_{mn} (z - z_{out})] \exp[-j (\alpha_m x + \beta_n y)], \quad n, m \in \mathbb{Z} \quad (2.23)$$

In the three-dimensional formulation, the coefficients \mathbf{r}_{mn} and \mathbf{t}_{mn} are constant vectors, and they become scalars for the two-dimensional formulation.

The propagation constant for each mode γ_{mn} can be found by

$$\gamma_{mn} = \begin{cases} \sqrt{k_0^2 - \alpha_m^2 - \beta_n^2} & ; \quad \alpha_m^2 + \beta_n^2 \leq k_0^2 \\ -j\sqrt{\alpha_m^2 + \beta_n^2 - k_0^2} & ; \quad \alpha_m^2 + \beta_n^2 > k_0^2 \end{cases} \quad (2.24)$$

where

$$\begin{aligned} \alpha_m &= \alpha_0 - \frac{2\pi m}{T_x} \\ \beta_n &= \beta_0 - \frac{2\pi n}{T_y} \end{aligned} \quad (2.25)$$

It can be seen that only a finite number of modes are propagating modes, and higher modes will be evanescent. This mesh truncation technique is rigorous since higher modes as well as the dominant ($m = n = 0$) mode are included in the analysis. In particular, it is important to include higher propagating modes, if there are any, as those modes can potentially have a significant effect. All the propagating modes and some of the evanescent modes should be included, but in practice any higher modes may be eliminated from the computation of the sums in Eq.2.21 and 2.23, as they will have a negligible effect on the analysis accuracy.

In the two-dimensional formulation, a similar expansion can be used to truncate the mesh. At the input boundary E_z can be expressed with reflection coefficients r_m as

$$E_z(x, y) = \exp[-j\chi_0(y - y_{in})] \exp(-j\alpha_0 x) + \sum_{m=-\infty}^{\infty} r_m \exp[j\chi_m(y - y_{in})] \exp(-j\alpha_m x) \quad (2.26)$$

Similarly, at the output boundary, E_z can be expressed with transmission coefficients t_m as

$$E_z(x, y) = \sum_{m=-\infty}^{\infty} t_m \exp[-j\chi_m(y - y_{out})] \exp(-j\alpha_m x) \quad (2.27)$$

Coordinates y_{in} and y_{out} are the y -coordinates of the incidence and exit boundaries, and α_m and χ_m are defined as

$$\alpha_m = \alpha_0 + \frac{2\pi m}{d}$$

and

$$\chi_m = \begin{cases} \sqrt{(n_L k_0)^2 - \alpha_m^2} & ; \quad (n_L k_0)^2 - \alpha_m^2 \geq 0 \\ -j\sqrt{\alpha_m^2 - k_0^2} & ; \quad k_0^2 - \alpha_m^2 < 0, \quad m \in \mathbb{Z} \end{cases} \quad (2.28)$$

2.4 Finite Element Formulation

The finite element equations can be obtained, following [42], by deriving the weak form associated with Eq.2.7 or 2.9 and using an approximation

$$\mathbf{E}^e \approx \sum_{i=1}^{N_e} \mathbf{N}_i^e \mathbf{E}_i^e \quad (2.29)$$

within each element e . The details of the derivation of the weak form and the finite element equations are given in appendices A and B.

In the following chapters, finite element formulations will be used to analyze electromagnetic wave propagation in periodic structures.

Chapter 3

Topology Optimization of 2D Periodic Dielectric Structures

In this chapter, topology optimization methods are used to design structures with periodicity in one direction. The goal is to find 1-D periodic structures that exhibit desirable transmission and reflection characteristics by distributing two dielectric materials of distinct electric permittivity values over a rectangular representative cell. The wave propagation is along the orthogonal direction of the direction of periodicity, and the material is assumed to be uniform in the third direction. For a polarized time-harmonic electromagnetic wave, the analysis reduces to finding a two-dimensional distribution of one of the electric field components by solving a scalar Helmholtz equation. This is a problem solved in [20] for minimum power transmission using a density function to describe the design and the finite element method as the analysis method. The problem can be solved as a minimization or maximization problem of transmission (or reflection) to design structures that can be used for many potential applications, e.g., frequency selective surfaces and radomes.

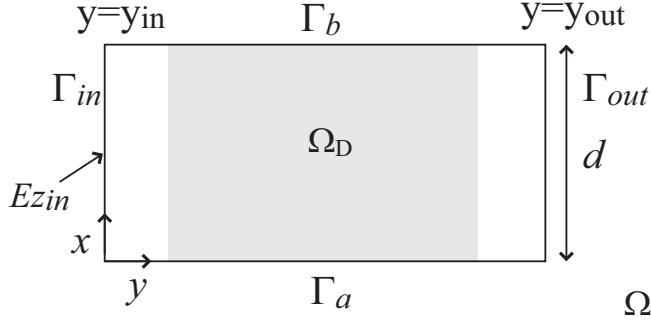


Figure 3.1: Design Domain

In this chapter, variations of the problem are solved using different design description and analysis methods to investigate an efficient way to solve this relatively simple problem. In section 1, an approach based on a level set function to describe the distribution of the constituent materials is used, combined with the finite element method with absorbing boundary condition for the mesh truncation. The analysis method employed here is the same as in [20]. In section 2, a standard density approach is used to describe the material distribution, combined with the finite element method using the plane wave expansion at the mesh truncation boundaries.

3.1 Problem Setup

The optimization problem is set up as follows. The objective of the problem is to find a 1-D periodic structure, described by the distribution of a material with relative electric permittivity ϵ_a in a background material of relative electric permittivity ϵ_b , that minimizes/maximizes the electromagnetic power flow. The problem is modeled on a 2D rectangular domain Ω shown in Fig.3.1. An incident field E_{zin} enters the domain from the left at Γ_{in} , and the power flow through the structure is measured at the right boundary Γ_{out} .

3.2 Level Set Approach

First, a level set function is used to represent the material distribution. Allaire, et al. [43] and Wang, et al. [44] are among the first authors that proposed a formulation of topology optimization problems based on level set methods. Level set methods use a so-called level set function to assign a material at each location in the problem domain. While a “classical” density approach permits the use of a mixture of two constituent materials in regions of intermediate density (“gray” regions), a level set function is combined with a step function to express material distribution, permitting no regions with intermediate material properties. However, in computations, even in level set methods there will be mixtures of the two phases near material interfaces, as a smoothed approximation of a step function is used. To facilitate convergence to binary solutions while avoiding complex designs, the work here follows the phase-field method introduced by Bourdin and Chambolle in [45], using a density approach, combined with a level-set representation of the design.

3.2.1 Material distribution

A level set function $\Phi(x, y) : \Omega \rightarrow \mathfrak{R}$ is used to describe the distribution of dielectric material ϵ_r within domain Ω as

$$\epsilon_r(\Phi) = \epsilon_b + H(\Phi) (\epsilon_a - \epsilon_b) \quad (3.1)$$

Here H is the Heaviside function defined as

$$H(\Phi) = \begin{cases} 1 & \text{if } \Phi \geq 0 \\ 0 & \text{if } \Phi < 0 \end{cases} \quad (3.2)$$

In summary, we have $\epsilon_r = \epsilon_a$ wherever the value of the function Φ is positive and $\epsilon_r = \epsilon_b$ wherever the value of is negative. The zero-level set of Φ defines the interfaces between ϵ_a and ϵ_b . In computation, a smooth approximation of the Heaviside function is used to avoid numerical difficulties.

3.2.2 Optimization problem

The goal of the optimization problem is to find a structure that minimizes power flow through it. The problem is stated as follows: Find $\Phi(x, y) : \Omega \rightarrow \Re$ that

minimizes

$$J(E_z) = \frac{1}{2} \int_{\Gamma_{out}} E_z E_z^* d\Gamma \quad (3.3)$$

subject to

$$A(\Phi) = \int_{\Omega} H(\Phi) d\Omega = A_0$$

where E_z^* is the complex conjugate of E_z , $A(\Phi)$ is the total area covered by material ϵ_a and A_0 is the prescribed area specifying the amount of material where ϵ_a is used.

A penalty term is added to the objective function to facilitate convergence to binary solutions while avoiding rapid variations in Φ that may result in complex shapes and poor convergence. The augmented objective function \bar{J} is defined as:

$$\bar{J} = J + \frac{1}{2} \int_{\Omega} \tau |\nabla \Phi|^2 + \tau \frac{\pi}{4\sqrt{2}} H(\Phi) (1 - H(\Phi)) d\Omega \quad (3.4)$$

The penalty parameter τ is adjusted according to the relative importance of the penalty term. A larger value of τ will result in a solution with simpler features or a slower variation in a material distribution. The Lagrangian associated with the optimization problem using

\bar{J} as the objective is:

$$L = \bar{J} + \lambda \left\{ \int_{\Omega} H(\Phi) d\Omega - A_0 \right\} \quad (3.5)$$

where a Lagrange multiplier λ associated with the are constraint is introduced. A gradient-based method is used to evolve the level set function Φ as

$$\frac{\partial \Phi}{\partial t} = -K \frac{\delta L}{\delta \Phi} = -K \left[\beta + \lambda \frac{\partial \epsilon_r}{\partial \Phi} - \tau \nabla^2 \Phi + \tau \frac{\pi}{4\sqrt{2}} (\delta(\Phi) - 2\delta(\Phi)H(\Phi)) \right] \quad (3.6)$$

where $K > 0$ is a proportionality constant that may be used to control the step size, and β is

$$\beta = k_0^2 \frac{\partial \epsilon_r}{\partial \Phi} E_z W = k_0^2 (\epsilon_a - \epsilon_a) \delta(\Phi) E_z W \quad (3.7)$$

Here W is the solution of the adjoint problem

$$-\nabla^2 W - k_0^2 \epsilon_r W = 0 \quad (3.8)$$

with boundary conditions:

$$\hat{n} \bullet \nabla W + jk_0 W = 0 \quad (3.9)$$

on the input boundary Γ_{in} and

$$\hat{n} \bullet \nabla W + jk_0 W = E_z \quad (3.10)$$

on the output boundary Γ_{out} , and δ is the Dirac-delta function.

Time evolution corresponds to an iterative scheme if the derivative of Φ is discretized as

$$\frac{\partial \Phi}{\partial t} \approx \frac{1}{\Delta t} \left(\Phi^{t+\Delta t} - \Phi^t \right) \quad (3.11)$$

with time increment Δt . The discretized version of Eq.3.6 is then:

$$\begin{aligned} \frac{1}{\Delta t} \left(\Phi^{t+\Delta t} - \Phi^t \right) = \\ - K \left[\beta + \lambda \Delta \epsilon \delta \left(\Phi^t \right) - \tau \nabla^2 \Phi^{t+\Delta t} + \tau \frac{\pi}{4\sqrt{2}} \left(\delta \left(\Phi^t \right) H \left(\Phi^t \right) \right) \right] \end{aligned} \quad (3.12)$$

Collecting terms with $\Phi^{t+\Delta t}$ on the left-hand side, we obtain an equation to update $\Phi^{t+\Delta t}$:

$$\begin{aligned} - \alpha \nabla^2 \Phi^{t+\Delta t} + \Phi^{t+\Delta t} = \\ \left\{ -K \Delta t \beta - \frac{\alpha \pi}{4\sqrt{2}} \left(\delta \left(\Phi^t \right) - 2 \delta \left(\Phi^t \right) H \left(\Phi^t \right) \right) + \Phi^t \right\} - \lambda \left(K \Delta t \Delta \epsilon \delta \left(\Phi^t \right) \right) \end{aligned} \quad (3.13)$$

with the Dirichlet boundary condition:

$$\Phi^{t+\Delta t} = c_0 \quad (3.14)$$

on the left and right boundaries of the design domain, where c_0 is a constant, fixing the material on the left and right boundaries of Ω_D and the periodicity condition

$$\nabla \Phi^{t+\Delta t}(x, y = 0) = \Phi^{t+\Delta t}(x, y = d) \quad (3.15)$$

and $\alpha = K \tau \Delta t$ controls the step size.

To solve Eq.3.13 for $\Phi^{t+\Delta t}$, first f_0 and f_1 are defined as follows.

$$\begin{aligned} f_0 &= -K\Delta t\beta - \frac{\alpha\pi}{4\sqrt{2}} \left(\delta \left(\Phi^t \right) - 2\delta \left(\Phi^t \right) H \left(\Phi^t \right) \right) + \Phi^t \\ f_1 &= K\Delta t\Delta\epsilon\delta \left(\Phi^t \right) \end{aligned} \quad (3.16)$$

The solution of Eq.3.13 can be expressed as

$$\Phi^{t+\Delta t} = \Phi_0 - \lambda\Phi_1 \quad (3.17)$$

where Φ_0 and Φ_1 are the solutions to:

$$\begin{aligned} -\alpha\nabla^2\Phi_0^{t+\Delta t} + \Phi_0^{t+\Delta t} &= f_0 \\ -\alpha\nabla^2\Phi_1^{t+\Delta t} + \Phi_1^{t+\Delta t} &= f_1 \end{aligned} \quad (3.18)$$

The Lagrange multiplier λ is determined by finding λ that satisfies

$$A \left(\Phi^{t+\Delta t} \right) = A_0 \quad (3.19)$$

3.2.3 Numerical examples

The governing equation Eq.2.9 is solved for the electric field component E_z . The problem is modeled and solved using the finite element method in a commercial software COMSOL [46] using the absorbing boundary condition, as described in Sec2.3.1. In all of the numer-

Table 3.1: Parameters for example 1

Parameter	d	D	ϵ_a	θ	A_0
Value	$0.3\lambda_0$	$4d$	5.0	0°	40%

ical examples investigated here, vacuum is used as the background material i.e. $\epsilon_b = 1$. Homogeneous regions with $\epsilon_r = \epsilon_b$ and depth $0.5d$ are placed to the right and left of the design domain Ω_D , so that any waves scattered off of a dielectric inclusion in Ω_D may be approximated as normally incident waves at Γ_{in} and Γ_{out} . The parameter τ is adjusted so that the relative magnitude of the phase-field term and the electromagnetic power flow term stays between $1/50$ and $1/100$. The parameter $K\Delta t$ is adjusted according to the mesh size.

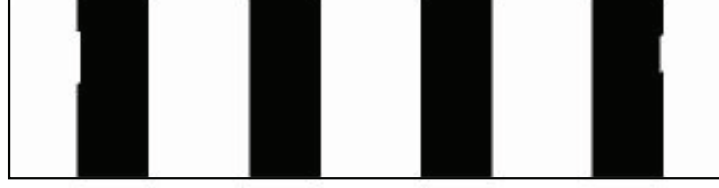
3.2.3.1 Example 1

This example uses parameters shown in Tab.3.2.3.1, where λ_0 is the wavelength of the incident electromagnetic wave in vacuum, corresponding to the prescribed incident frequency of 100GHz. A structure with uniform permittivity is used as an initial guess. Normal incidence $\theta = 0^\circ$ is used, and 40% of the area is allowed to have the inclusion material ($\epsilon_r = \epsilon_a$).

The optimal structure and the electric field distribution through it are shown in Fig.3.2. In Fig.3.2(b) the red and blue regions correspond to high and low electric field strength. The power transmitted J is computed as in Eq.3.3, and compared to the value of J through vacuum, J_0 . The ratio

$$R_J = \frac{J}{J_0} \quad (3.20)$$

is used to report the performance of the optimum structure. The structure shown in Fig.3.2 achieves $R_J = 2.24 \times 10^{-3}$.



(a) Optimum structure



(b) Electric field magnitude through the optimum structure

Figure 3.2: Optimal structure and the field distribution for example 1. For interpretation of the references to color in this and all other figures, the reader is referred to the electronic version of this thesis (or dissertation).

Table 3.2: Parameters for example 2

Parameter	d	D	ϵ_a	θ	A_0
Value	$0.3\lambda_0$	$4d$	11.56	0°	19.6%

3.2.3.2 Example 2

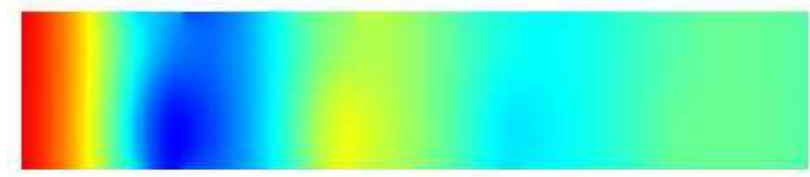
Parameters shown in Tab.3.2.3.2 are used for this example. Normal incidence is used, and this time only 19% of the area is allowed to have the inclusion material ($\epsilon_r = \epsilon_a$), but a higher dielectric constant is used. A structure with uniform permittivity is used as an initial guess again.

The optimal structure is shown in Fig.3.3, through which $R_J = 1.04 \times 10^{-4}$ is achieved.

The objective function J is plotted over a range of incident frequencies in Fig.3.4. The plot shows that the solution has the characteristics of a band-gap structure, with a gap of low transmission in a frequency range between 70-120GHz. The structure shown in Fig.3.3(a) indeed resembles a known photonic band-gap, discussed by Sigmund and Hougaard in [47]. See Fig.3.5(a) and (b) for the photonic band-gap structure and its performance, computed



(a) Optimum structure



(b) Electric field magnitude through the optimum structure

Figure 3.3: Optimal structure and the field distribution for example 2.

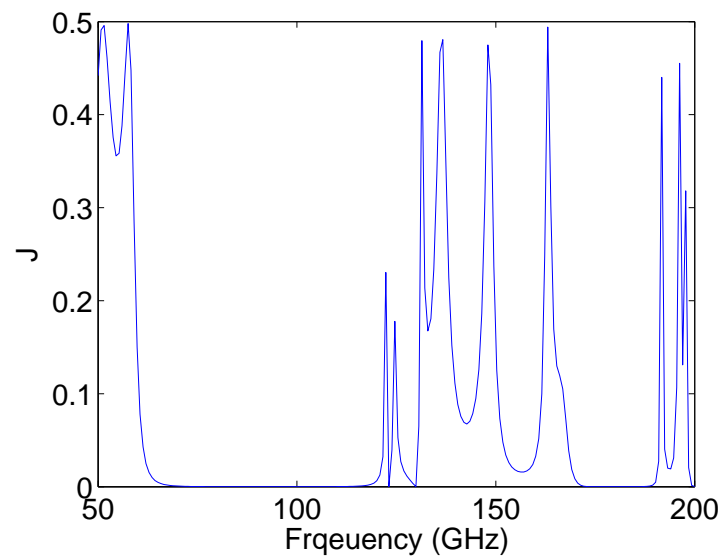
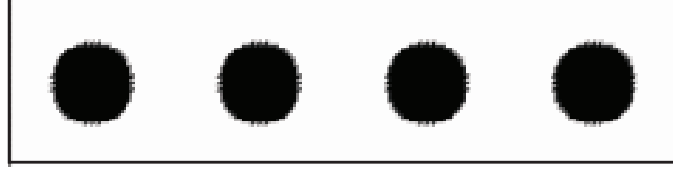
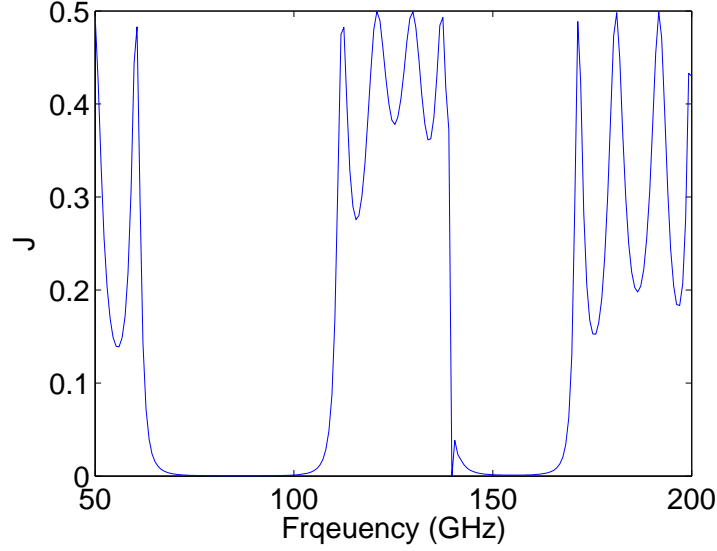


Figure 3.4: Frequency sweep for the optimum structure for example 2.



(a) Band-gap structure



(b) Frequency sweep for the band-gap structure

Figure 3.5: A known band-gap structure and the frequency sweep.

using the parameters displayed in Tab.3.2.3.2.

Comparing the performance of the two structures, we observe that the solution obtained through optimization performs better than the band-gap structure at the prescribed target frequency of 100GHz ($R_J = 2.44 \times 10^{-3}$ for the band-gap structure). In this example, the algorithm found a structure that resembles a photonic band-gap structure with high performance. Looking at the structure in Fig.3.3(a), we also observe that the structure is not symmetric across the middle of the design domain, even though the incident angle is 0° , and the domain is periodic in the vertical direction. We suspect that this lack of symmetry may be caused by small numerical discrepancies in the periodic boundary conditions applied

during the finite element analysis.

3.2.4 Conclusion

In computations, smoothing of the level set function is necessary when using a gradient-based optimization algorithm, and in the end solutions still suffer from having mixture (gray) regions at interfaces. It was also observed that several parameters affecting the analysis accuracy and optimization algorithm need to be adjusted in an ad hoc manner but with great care to avoid numerical instability.

3.3 Density Approach

Next, an interpolation scheme similar to the SIMP approach [48], [49], [50] is used to characterize the material distribution. This is a “classical” approach used in topology optimization problems. To facilitate convergence a filter is used.

3.3.1 Material distribution

The relative permittivity at location (x, y) in Ω is expressed as

$$\epsilon_r(\rho) = \epsilon_b + (\epsilon_a - \epsilon_b)\rho^p \quad (3.21)$$

where $\rho = \rho(x, y) \in [0, 1]$ is the effective density of material ϵ_a and $p \geq 1$ is a coefficient used to facilitate convergence. The effect of the parameter p is explained later. Upon discretization, ρ is piece-wise constant, taking a constant value ρ_e within each element e . The computational domain Ω may include a subdomain Ω_0 where ρ is fixed, i.e., where the

material is not designed.

3.3.2 Optimization problem

The analysis of the electric field distribution is done using the plane wave expansion at the input and output boundaries (Γ_{in} and Γ_{out} in Fig.3.1), as described in Sec.2.3.3. Details of the finite element formulation are given in Appendix A. Using this formulation, one obtains the modal transmission and reflection coefficients as a part of the solution. That is, the solution to the finite element equation (Eq.3.22)

$$\begin{bmatrix} \mathbf{K}_{EE} & \mathbf{K}_{Er} & \mathbf{K}_{Et} \\ \mathbf{K}_{rE} & d\mathbf{I} & \mathbf{0} \\ \mathbf{K}_{tE} & \mathbf{0} & d\mathbf{I} \end{bmatrix} \begin{bmatrix} \mathbf{E}_z \\ \mathbf{r} \\ \mathbf{t} \end{bmatrix} = \begin{bmatrix} \mathbf{f}_E \\ \mathbf{f}_r \\ \mathbf{0} \end{bmatrix} \quad (3.22)$$

includes not only the field distribution \mathbf{E}_z but the reflection \mathbf{r} and transmission \mathbf{t} coefficients associated with all the modes included in the analysis. The objective of the optimization problem can be defined by extracting the relevant reflection/transmission coefficients. The optimization problem is stated as follows: Find ρ that

minimizes

$$J = J(\mathbf{z}(\rho), \mathbf{z}^*(\rho)) = \mathbf{z}^* \mathbf{T} \mathbf{A} \mathbf{z} \quad (3.23)$$

subject to

$$0 \leq \rho \leq 1$$

where \mathbf{A} is a diagonal matrix with constant coefficients

$$A_{kk} = \{ \underbrace{0, \dots, 0}_{N_n \text{ terms}}, \underbrace{a_{-N_m}, \dots, a_0, \dots, a_{N_m}}_{2N_m+1 \text{ terms}}, \underbrace{b_{-N_m}, \dots, b_0, \dots, b_{N_m}}_{2N_m+1 \text{ terms}} \} \quad (3.24)$$

Matrix \mathbf{A} is used to accommodate different design goals by selecting different values for the coefficients a_k and b_k . For instance, setting $a_k = 1$ and $b_k = 0$ sets the objective function J to be the sum of absolute values of reflection coefficients r_m . If reflection coefficients of only the propagating modes are included in the sum, the value of the objective function becomes the reflection coefficient at the incident boundary. Similarly, setting $a_k = 0$ and $b_k = 1$ corresponds to minimization of transmission at the exit boundary.

3.3.3 Optimality condition

The Lagrangian L associated with (4.6) with non negative multipliers μ_1 and μ_2 is

$$L = J(\rho) + \mu_1(\rho - 1) + \mu_2(-\rho) \quad (3.25)$$

If ρ^* is a local optimum, the KKT conditions require that for each design variable ρ_e^*

$$\frac{\partial L}{\partial \rho_e^*} = \frac{\partial J}{\partial \rho_e^*} + \mu_1 - \mu_2 = 0 \quad (3.26)$$

If $\rho_e^* = 0$, $\mu_1 = 0$ and $\mu_2 > 0$, then from (3.26) $\frac{\partial J}{\partial \rho_e^*} = \mu_2 > 0$. If $\rho_e^* = 1$, $\mu_1 > 0$ and $\mu_2 = 0$, then $\frac{\partial J}{\partial \rho_e^*} = -\mu_1 < 0$. Otherwise, $\mu_1 = \mu_2 = 0$ and $\frac{\partial J}{\partial \rho_e^*} = 0$. In summary, if ρ^* is a local optimum, then for all $e = 1, \dots, N_e$

$$\begin{aligned}
\frac{dJ}{d\rho_e} &> 0 \quad \text{if} \quad \rho_e = 0 \\
\frac{dJ}{d\rho_e} &< 0 \quad \text{if} \quad \rho_e = 1 \\
\frac{dJ}{d\rho_e} &= 0 \quad \text{if} \quad 0 < \rho_e < 1
\end{aligned} \tag{3.27}$$

where N_e is the number of elements.

3.3.4 Sensitivity analysis

Gradients of the objective function J are computed using a standard adjoint variable approach, starting from

$$\frac{dJ}{d\rho_e} = \frac{\partial J}{\partial \mathbf{z}^*} \frac{\partial \mathbf{z}^*}{\partial \rho_e} + \frac{\partial \mathbf{z}}{\partial \rho_e}^T \left(\frac{\partial J}{\partial \mathbf{z}} \right)^T = \lambda_e^T P_e + \lambda_e^{*T} P_e^* \tag{3.28}$$

for all $e = 1, \dots, N_e$. The adjoint variable λ_e is obtained by solving the adjoint problem

$$\mathbf{K}^T \lambda = \left(\frac{\partial J}{\partial \mathbf{z}} \right)^T = \mathbf{A}^T \mathbf{z}^* \tag{3.29}$$

Vector P_e is computed using

$$P_e = -\frac{\partial \mathbf{K}_e}{\partial \rho_e} \mathbf{z}_e \tag{3.30}$$

Note that the portion of the stiffness matrix that corresponds to the area integral, \mathbf{K}_{EE} , is the only component of \mathbf{K} that depends on the design variable ρ and therefore

$$\frac{\partial \mathbf{K}_e}{\partial \rho_e} = \begin{bmatrix} \frac{\partial \mathbf{K}_{EEe}}{\partial \rho_e} & \mathbf{0} & \mathbf{0} \\ \mathbf{0} & \mathbf{0} & \mathbf{0} \\ \mathbf{0} & \mathbf{0} & \mathbf{0} \end{bmatrix}$$

with

$$\frac{\partial K_{EEe}^{ij}}{\partial \rho_e} = \frac{\partial K_{EEe}^{ij}}{\partial \epsilon_r} \frac{\partial \epsilon_r}{\partial \rho_e} = k_0^2 p \rho_e^{p-1} (\epsilon_a - \epsilon_b) \int_{\Omega_e} \phi_e^i \tilde{\phi}_e^j dx dy$$

3.3.5 Influence of parameter p

The factor p in Eq.4.5 does not have the same effect as in a typical topology optimization problem with a volume constraint. Here the factor is used only to speed up convergence to a binary solution. In numerical experiments, it is observed that convergence in regions of elements with high values of ρ (near $\rho = 1$) is faster than convergence of elements with low ρ values (near $\rho = 0$). What is also notable is that a strictly binary solution has better performance for a minimum transmission problem than a solution of similar topology where a thin layer of intermediate permittivity ($0 < \rho < 1$) is present at the interface between the two phases. This can be explained using an analogy to camera lens design. Often, a camera lens is coated with a matching layer of material with permittivity value between air and the lens material to improve transmission of light into the lens. Without the intermediate layer, the large mismatch between the indices of refraction would cause a strong reflection at the interface. For a minimum transmission problem the opposite is true, a high contrast is desirable and thus removing “gray” elements at the interface improves performance.

Based on those observations, the following scheme is implemented to speed up conver-

gence to a binary solution. The value $p = 1$ is used until the optimality conditions (Eq.3.27) are satisfied. If the solution is not essentially binary (less than a small percentage of elements is “gray”), p is increased e.g. up to $p = 3$. Iterations continue until a maximum number of iterations is reached or until convergence to an essentially binary solution is achieved. In most problems, setting $p = 1$ is sufficient. Occasionally faster convergence is achieved by using $p = 3$. No instance was observed where the final solution depends on the value of p .

3.3.6 Numerical examples

The use of the approach is illustrated using simple examples that focus on different features of the problem. A material with relative electric permittivity $\epsilon_a = 12$ (*Si*) is distributed in a background material with $\epsilon_b = 4.5$ (*SiO₂*). The permittivity of a vacuum is assumed for the material outside of the analysis domain Ω . Without loss of generality, the magnitude of the excitation $|E_{zin}|$ is set to unity for convenience. Other parameters such as the wavelength of the incident wave λ , angle of incidence θ , the dimension of the cell in the propagation direction D , and the highest mode order N_m used in modal expansions are chosen in each case to highlight different features of the problem or its solution. All examples are solved using the MMA (Method of Moving Asymptotes) [51]. Except as noted, the initial design has uniform permittivity with $\rho = 0.2$ throughout the design domain. A filter is used to avoid complex designs and facilitate convergence to binary solutions. A “cone” filter [52], [53] with $r_{min} = 1.5$ is used. Iterations start with $p = 1$ and may increase to $p = 3$.

Table 3.3: Parameters used in Example 1

D	λ/d	θ	N_m
$4d$	3.7	40°	9

3.3.6.1 Example 1

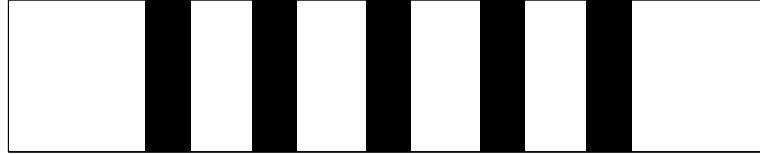
In this example we explore the solution of the problem solved in [20]. Slabs of non-designable material of width $d_0 = 0.5d$ and fixed permittivity ϵ_b are placed at the incidence and exit boundaries. The objective is to find a configuration that minimizes transmission, which corresponds to setting $a_k = 0$ in Eq.3.24. Coefficients b_k are set as follows:

$$b_k = \begin{cases} 1 & \text{if } \chi_k \text{ is real} \\ 0 & \text{if } \chi_k \text{ is imaginary} \end{cases}$$

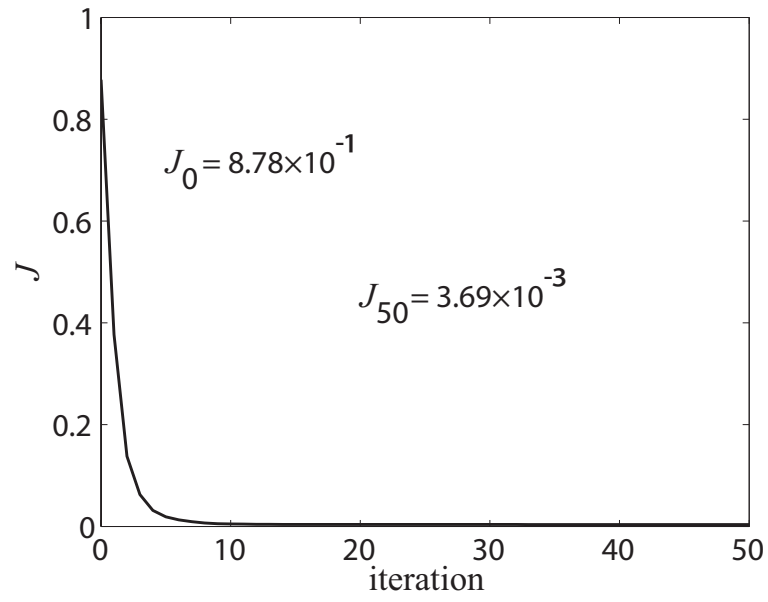
Mode numbers k take integer values in $[-N_m, N_m]$. χ_k can be computed for each mode k as in Eq.A.4, based only on design independent parameters d, k_0 , and θ . Note that a real χ_k corresponds to a propagation mode and an imaginary χ_k corresponds to an evanescent mode.

An electromagnetic wave with wavelength $\lambda = 3.7d$ ($k_0 = \frac{2\pi}{\lambda}$ in Eq.2.9) is incident at the boundary Γ_{in} at $\theta = 40^\circ$. The highest mode order included in the wave expansion N_m is set to 9. This is the maximum value allowed under the Nyquist condition so that the wavelength of mode N_m is larger than the length of two elements. Values of other parameters used in this example are shown in Table 3.3.6.1.

The optimum material layout and the iteration history are shown in Fig.3.6(a) and (b). The solution is feasible and satisfies optimality conditions (Eq.3.27) within a prescribed



(a) Optimum structure



(b) Iteration history

Figure 3.6: Example 1. Optimum solution and iteration history

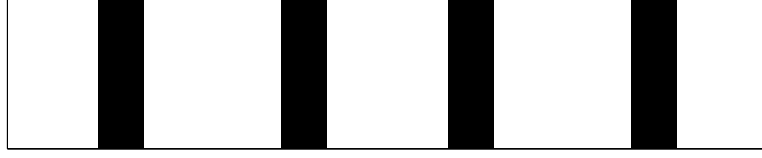


Figure 3.7: Example 1. Optimum solution with vacuum background material

tolerance, i.e., replacing Eq.3.27 by

$$\begin{aligned} \frac{dJ}{d\rho_e} &> 0 & \text{if } \rho_e &\leq \delta \\ \frac{dJ}{d\rho_e} &< 0 & \text{if } \rho_e &\geq 1 - \delta \\ \left| \frac{dJ}{d\rho_e} \right| &\leq \delta & \text{otherwise} \end{aligned}$$

with a threshold $\delta = 0.001$. In this problem the same solution is obtained if only one term is kept in the plane wave expansion, i.e., if the problem is solved with $N_m = 0$. This is not surprising since higher modes become less significant when homogeneous slabs of length $0.5d$ are placed at the incidence and exit boundaries. Moreover, in the design in Fig.3.6(a) all the material interfaces are parallel to the tiling vector. As a result, only the dominant mode is present, i.e. there is no coupling into higher modes. This confirms the validity of the single mode assumption used in [20] and [21]. However, the authors in [20] report an instability in the optimization procedure when transmission at the boundary is used as the objective function. Because of this instability the authors are forced to use a surrogate objective function based on an area integral of the field. In the present work, however, no such instability is observed, as verified by the iteration history in Fig.3.6(b). It should also be noted that the material layout found here is qualitatively different from the solution obtained in [20].

To investigate the influence of the host medium, the problem is now solved setting the background material to vacuum. Figure 3.7 shows the optimum solution. The two have

Table 3.4: Parameters used in Example 2

D	λ/d	θ	N_m
$2d$	$2.5 - 3.3$	40°	10

qualitatively similar features (straight bands parallel to the tiling vector), but a much lower objective function value of $J = 4.98 \times 10^{-5}$ (compared to $J = 3.69 \times 10^{-3}$) is achieved when vacuum is used. The improvement in performance is due to the higher contrast in indices of refraction, which causes stronger reflection.

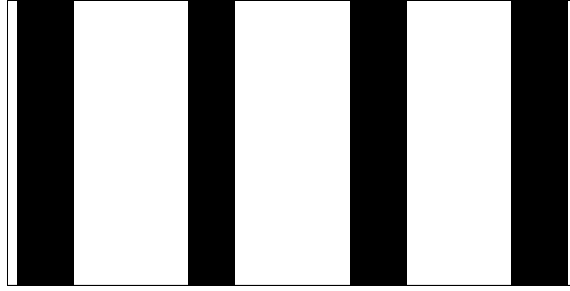
3.3.6.2 Example 2

In this example we seek a configuration that minimizes transmission for wavelengths in the range $\lambda/d = 2.5 - 3.3$. Material can be designed everywhere in Ω . The function $J^{(i)} = \mathbf{z}^* T^{(i)} \mathbf{A}^{(i)} \mathbf{z}^{(i)}$ is computed for each $(\lambda/d)^{(i)}$ in the interval $[2.5, 3.3]$ at 7 equally spaced sample points. Terms are then added up to obtain the total objective $J = \frac{1}{7}(J^{(1)} + J^{(2)} + \dots + J^{(7)})$. Coefficients a_k and b_k are set as in Example 1 for each $(\lambda/d)^{(i)}$. Values for other parameters used in this example are shown in Tab.3.3.6.2.

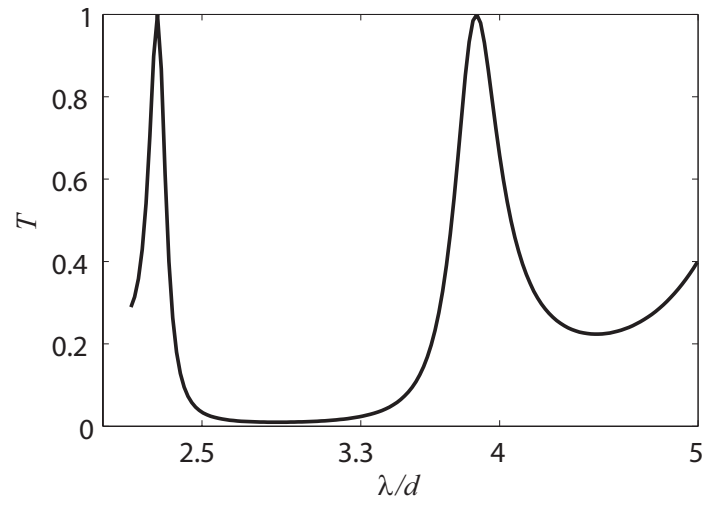
After 200 iterations, a solution that satisfies the optimality conditions with $\delta = 0.001$ is obtained. The solution has a small number of gray elements near the interfaces between the two materials, which are removed by applying a simple threshold at $\rho = 0.5$ with negligible effect on performance. Figure 3.8(a) shows the solution after postprocessing. For this solution the total transmission coefficient is calculated as

$$T = \sum_{\tilde{k}} |t_{\tilde{k}}|^2 \quad (3.31)$$

where the sum is over all modal transmission coefficients of propagating modes \tilde{k} . T is



(a) Optimum solution after postprocessing



target $\lambda/d = 2.5-3.3$

(b) Wavelength sweep

Figure 3.8: Example 2. Solution and its wavelength sweep

plotted in Fig.3.8(b) for a range of wavelengths. Note that $T = 1$ corresponds to total transmission while $T = 0$ corresponds to total reflection of the incident wave. A drop in transmission is apparent in the range $\lambda/d = 2.5 - 3.3$, verifying that the solution has the propagation characteristics set as the target of the optimization problem.

3.3.6.3 Example 3

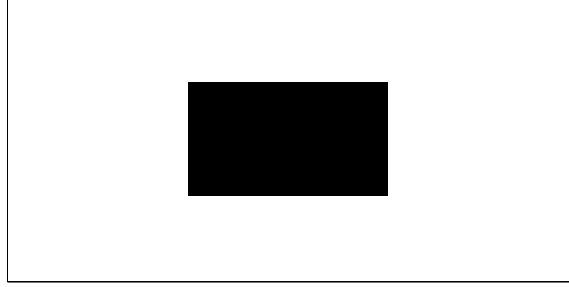
In the preceding examples solutions achieve optimum performance through the use of material arranged in straight bands of varying widths and spacing parallel to the tiling vector. One can change the number, width and spacing of the bands of material to achieve the desired transmission characteristics. The preceding examples show that the optimization algorithm essentially uses this strategy to find optimum combinations of the band parameters. Coincidentally, the configurations found have homogeneous slabs at the incidence and exit boundaries, as well as a simple overall material distribution inside the computational domain. As a result, a single mode assumption turns out to be sufficient in the analysis of these problems.

In this example, an instance where the single mode assumption is not valid, is shown. This solution is obtained by biasing the optimization algorithm with a non uniform initial guess. A number of arbitrary starting layouts were tested, and a layout that yielded a qualitatively different optimum layout was used. This starting design converges to a more complicated material layout that requires a higher number of modes be included in the analysis.

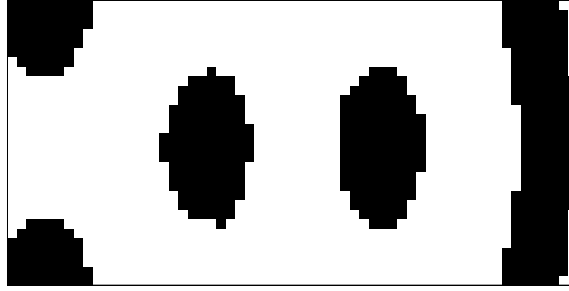
In this example, the goal is to achieve a low transmission configuration at any angle of incidence between 0° and 90° . A weighted sum of the objective function J evaluated over a finite number of angles is used in computations. The objective function $J^{(i)}$ is computed for

Table 3.5: Parameters used in Example 3

D	λ/d	θ	N_m
$2d$	3.0	$0^\circ, 20^\circ, 40^\circ, 45^\circ, 60^\circ, 80^\circ$	10



(a) Initial design

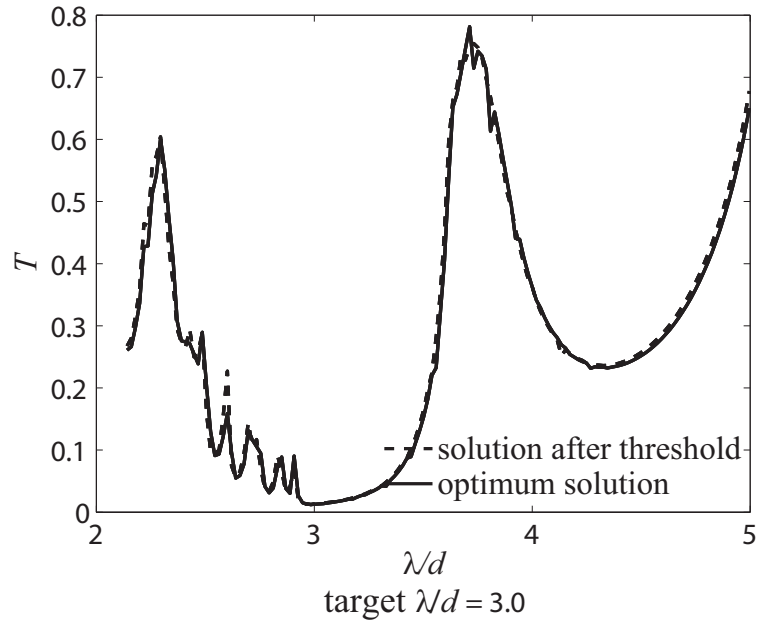


(b) Optimum solution after postprocessing

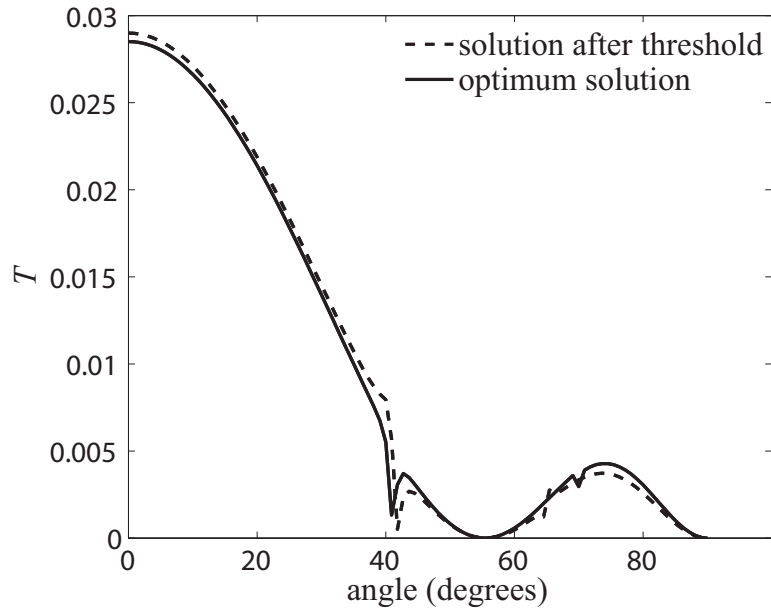
Figure 3.9: Example 3. Initial design and optimum solution after postprocessing

each angle $\theta^{(i)}$, and the total objective is calculated as $J = \frac{1}{N_a}(J^{(1)} + J^{(2)} + \dots + J^{(N_a)})$, where N_a is the number of angles included. It should be noted that the angles should be selected with some care. For instance, the set $0^\circ, 20^\circ, 40^\circ, 60^\circ$ and 80° yields an undesirable peak in transmission at 45° (the remedy is straight forward: simply add 45° to the set). The coefficients a_k and b_k are set as in Example 2 when computing each $J^{(i)}$. Values for other parameters used in this example are shown in Tab.3.3.6.3.

The initial guess and the optimum solution after postprocessing are shown in Fig.3.9(a) and (b). Again, the solution (before postprocessing) satisfies the optimality conditions with a threshold $\delta = 0.001$. Figure 3.10(a) shows the total transmission coefficient T averaged over all angles of incidence, plotted for wavelengths in a range around the target wavelength



(a) Wavelength sweep



(b) Angle sweep

Figure 3.10: Example 3. Wavelength and angle sweeps ($N_m = 10$)

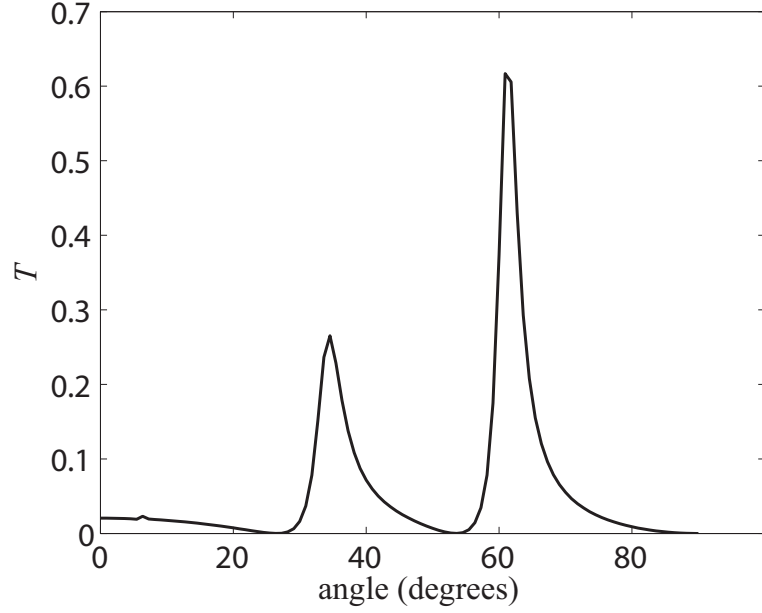


Figure 3.11: Example 3. Angle sweep computed using one mode only ($N_m = 0$)

$\lambda = 3.0d$. The solid and dashed lines show the wavelength response curves of the solution before and after postprocessing, respectively. There is no significant difference between the two curves, and in both cases transmission is suppressed at the target wavelength $\lambda = 3.0d$, as desired. Objective function values are $J = 1.32 \times 10^{-2}$ and $J = 1.28 \times 10^{-2}$, respectively (The solution after postprocessing is better. Note that a filter was used and this prevents the algorithm from reaching a binary solution). Figure 3.10(b) shows the response of the optimum configuration for various angles. T is plotted in the range 0° - 90° with $\lambda = 3.0d$ for the solution before (dashed) and after (solid) postprocessing. Again, no significant difference is observed between the two designs. In both cases, even though transmission is not uniform for all angles, it is suppressed over the entire range of interest 0° - 90° .

With the more complex material distribution in Fig.3.9(b), one must be careful to account for higher modes in the analysis. Complexity of the material distribution, especially inhomogeneity near the incident and exit boundaries, may result in significant deviations

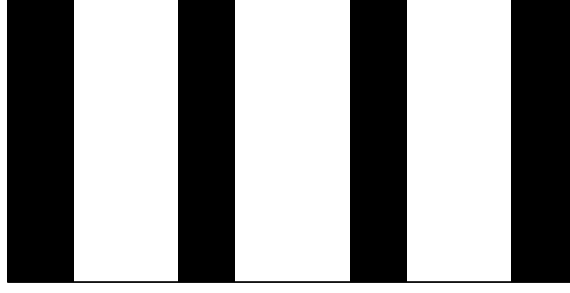


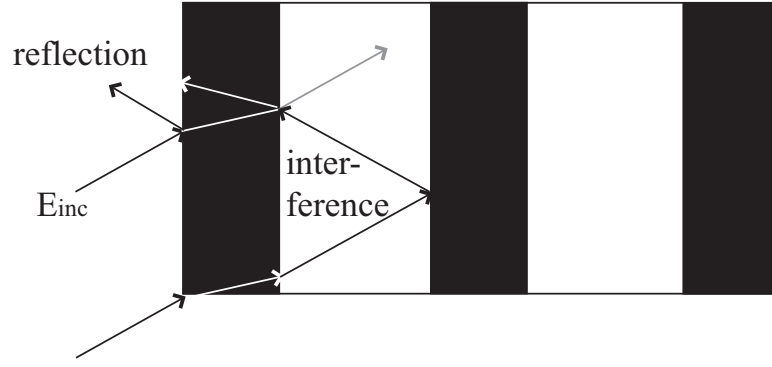
Figure 3.12: Example 3. Optimum structure starting from a homogeneous material distribution

from the single mode assumption. This is illustrated by Fig.3.11, where the response for different incidence angles is shown for the design in Fig.3.9(b), computed now using only one mode ($N_m = 0$). The figure clearly shows that using only a single mode analysis the predicted response is quite different from that obtained when $N_m = 10$ is used (Fig.3.10(b)). Using a single mode expansion in this case could lead to convergence to erroneous results.

To conclude this example the problem is solved again, starting now from a homogeneous initial design with $\rho = 0.2$. Figure 3.12 shows an optimum solution starting from such design. This solution has an objective value of $J = 1.08 \times 10^{-2}$, compared to the value $J = 1.28 \times 10^{-2}$ obtained using the non uniform initial design. The new configuration in Fig.3.12 differs from the one in Fig.3.9 in that it allows for analysis using a single mode assumption, simply because of the homogeneous material placed at the incidence and exit boundaries.

3.3.7 Designs with parallel bands

In most instances, layouts with bands parallel to the tiling vector were found as optimum solutions. As the incoming wave arrives at the first “black” band, the magnitude of the transmitted wave is reduced due to reflection (see Fig.3.13 (a)). At the next interface the



(a) Bands parallel to the tiling vector



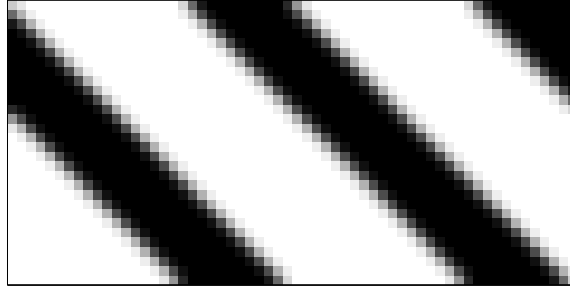
(b) Bands perpendicular to the incidence

Figure 3.13: Wave propagation through vertical and inclined bands

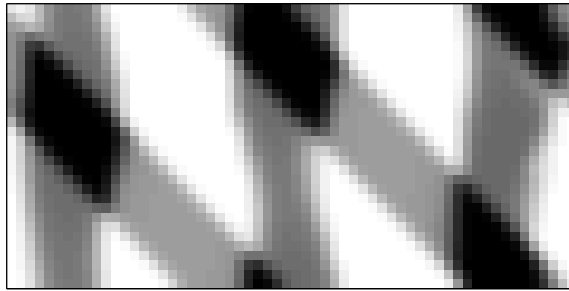
magnitude of the wave is reduced further due to reflection as well as destructive interference with a wave that is reflected off of an adjacent interface. Going through multiple bands in this manner, the transmitted wave at the exit boundary will be of reduced magnitude. This explanation applies to any angle of incidence.

In contrast, a layout with slanted bands has sharp corners at the incidence boundary (see Fig.3.13 (b)). As the incoming wave enters the domain, reflection at each band reduces the magnitude of the wave as before. However, as the incident wave scatters at a corner, the overall wave propagation behavior is significantly altered. In particular, electromagnetic power flow into the direction parallel to the bands is allowed in the form of surface wave modes, thus the wave may have high transmission at the exit boundary.

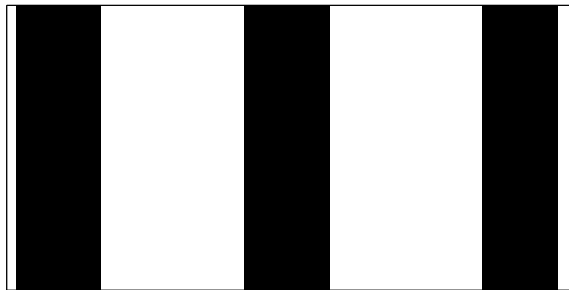
To investigate the effectiveness of a layout with bands parallel to the tiling vector, a



(a) Initial guess



(b) After 10 iterations



(c) Optimum structure

Figure 3.14: Optimization using slanted bands for the initial guess

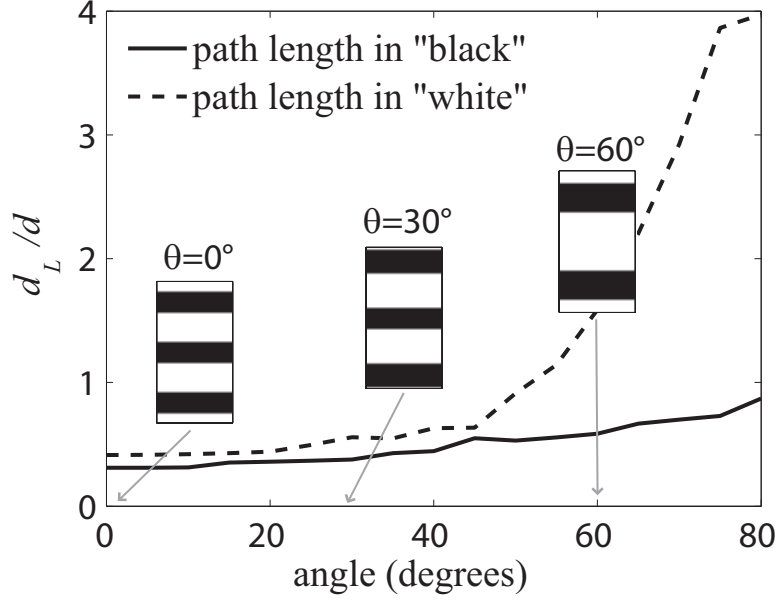


Figure 3.15: Angle dependency of the path length d_L

Table 3.6: Parameters used for the angle dependency

D	λ/d	θ	N_m
$1.9d$	1.4	variable	11

minimum transmission problem is solved using as the initial guess a slanted grating perpendicular to the incident wave at angle of incidence $\theta = 45^\circ$ (Fig. 3.14 (a)). A layout with bands parallel to the tiling vector is obtained (Fig. 3.14 (b) and (c)) as predicted from the earlier discussion.

Even though qualitatively very similar designs are effective for any angle of incidence θ , optimum solutions do depend on θ . The number of bands and the spacing between them are adjusted depending on the angle of incidence. To illustrate this point, a problem is solved with the parameters shown in Tab. 3.3.7 for angles of incidence in the interval $[0^\circ, 80^\circ]$ with a 5° increment. Lower electric permittivity values $\epsilon_b = 1$ and $\epsilon_a = 1.5$ are used to amplify the angle dependency.

The optimum structures for $\theta = 0^\circ$, $\theta = 30^\circ$, $\theta = 60^\circ$ are shown in Fig. 3.15. The length

of the path that the refracted wave travels inside each band in the optimum layout, d_L , is plotted over angles of incidence in Fig.3.15. For this simple geometry, d_L can be computed analytically from the material properties and Snell’s law. The solid and dotted lines show the path length inside “black” ($\epsilon_a = 1.5$) and “white” ($\epsilon_b = 1$) bands respectively. As the angle of incidence increases, the spacing between the bands is adjusted and the path length increases. The curves are continuous even though the number of bands in the optimum solution is not. The number of bands decreases as the spacing between bands becomes too large to fit within the domain (the number of bands depends on D).

3.3.8 Conclusion

For minimum transmission problems the solution strategy proposed is stable and robust, even when only boundary terms are included in the objective. The formulation presented can accommodate complex material distributions near boundaries by considering a variable number of modes kept in the wave expansion at the boundaries. The problem has potentially many local optima. Straight bands of material were found as optimum configurations whenever uniform initial configurations were used. In those cases a single mode approximation is sufficient for accurate analysis: the same result would be obtained whether higher modes are included or not. More complex material distributions appeared in optimum configurations when iterations started from non uniform designs. In such cases it is crucial to include higher modes in the analysis, as the single mode assumption could result in inaccurate evaluations of performance. An advantage of the method introduced here is that it does not rely on an a priori knowledge of how many modes should be kept to maintain accuracy. The optimization method works equally well and with only marginally different effort whether one or more

modes are used in the analysis.

Chapter 4

Topology Optimization of 3D Periodic Structures

In this chapter, a topology optimization method is used to design structures with periodicity in two directions. The problem is setup in a similar manner as in chapter 3, for the design of 1-D periodic structures. The goal of the design problem is to find periodic structures that exhibit desirable transmission and reflection characteristics. Dielectric materials are distributed in a 3D design domain by assigning an effective density at each location within the domain.

4.1 Problem Setup

The optimization problem is set up as follows. The objective of the problem is to find a 2-D periodic structure, described by a distribution of a dielectric material within the design domain shown Ω_D in Fig.4.1, that minimizes/maximizes the electromagnetic power flow. The electromagnetic propagation is analyzed within a 3D domain Ω , which is a representative

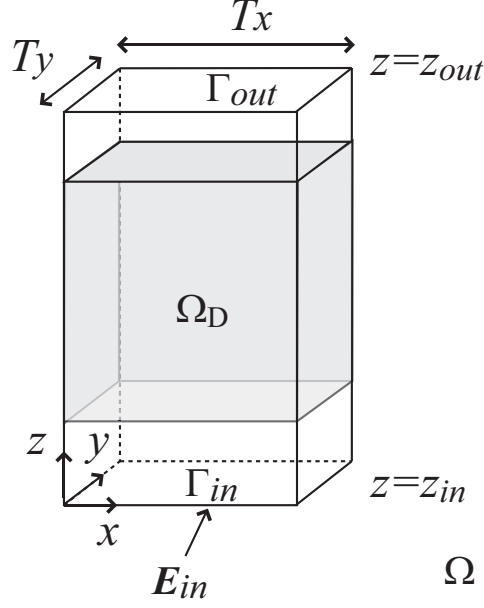


Figure 4.1: Design Domain

cell of a periodic structure with periodicity in the x - and y -directions with tiling vectors $\mathbf{e}_x = (Tx, 0, 0)$ and $\mathbf{e}_y = (0, Ty, 0)$. An incident field \mathbf{E}_{in} enters the domain from the bottom at Γ_{in} , and the power flow through the structure is measured at the top boundary Γ_{out} . The finite element method is used to carry out the analysis, with a plane wave expansion at the truncation boundaries (Γ_{in} and Γ_{out} in Fig.4.1), as described in Sec.2.3.3. Details of the finite element formulation are give in appendix B.

The electric field is assumed to take the form

$$\begin{aligned}
 \mathbf{E}(x, y, z) &= \mathbf{E}_{in} + \mathbf{E}_{ref} \\
 &= \exp \left\{ -j \left[\alpha_0 x + \beta_0 y + \gamma_0 (z - z_{in}) \right] \right\} \hat{p} \\
 &+ \sum_{m=-\infty}^{+\infty} \sum_{n=-\infty}^{+\infty} \mathbf{r}_{mn} \exp \left[j \gamma_{mn} (z - z_{in}) \right] \psi_{mn}
 \end{aligned} \tag{4.1}$$

at the input boundary Γ_{in} and

$$\begin{aligned}\mathbf{E}(x, y, z) &= \mathbf{E}_{tr} \\ &= \sum_{m=-\infty}^{+\infty} \sum_{n=-\infty}^{+\infty} \mathbf{t}_{mn} \exp[-j\gamma_{mn}(z - z_{out})] \psi_{mn}\end{aligned}\quad (4.2)$$

at the output boundary Γ_{out} . In Eqs.4.1 and 4.1 $\psi_{mn} = \exp[-j(\alpha_m x + \beta_n y)]$, α_m and β_n are x - and y -components of the propagation vector, and γ_{mn} is the propagation constant. Infinite sums in the expansion are truncated in computation, as in the 2D structure case.

The modal transmission and reflection coefficients (\mathbf{t}_{mn} and \mathbf{r}_{mn}) can be computed as

$$\mathbf{t}^{mn} = \frac{1}{T_x T_y} \int_{\Gamma_{out}} \mathbf{E} \psi_{mn}^* d\Gamma \quad (4.3)$$

and

$$\mathbf{r}^{mn} = \frac{1}{T_x T_y} \int_{\Gamma_{in}} (\mathbf{E} - \mathbf{E}_{in}) \psi_{mn}^* d\Gamma \quad (4.4)$$

where \mathbf{t}_{mn} and \mathbf{r}_{mn} are complex constant vectors.

4.2 Material distribution

The relative permittivity at location (x, y, z) in Ω_D is expressed as

$$\epsilon_r(\rho) = \epsilon_b + (\epsilon_a - \epsilon_b)\rho \quad (4.5)$$

in terms of relative permittivities of constituents, ϵ_a and ϵ_b . Here $\rho = \rho(x, y, z) \in [0, 1]$ is the effective density of the inclusion material ϵ_a . Upon discretization, ρ is piece-wise constant, taking a constant value ρ_e within each element e .

The effective density ρ may be controlled through a piece-wise constant mapping X . One choice is to consider a material distribution that only varies in the x - and y -directions and is uniform in the “thickness” (z -) direction, so that $\rho(x, y, z) = X(x, y)$. A more complex case would be a variable material distribution in all three directions. Only the former case is considered here, and the latter case is not investigated for its excess complexity in computation and fabrication.

4.3 Optimization problem

The objective function of the optimization problem can be defined in terms of reflection or transmission coefficients. The optimization problem is stated as follows: Find $X(x, y)$ that

minimizes

$$J = J(\mathbf{S}(\rho(X)), \mathbf{S}^*(\rho(X))) = \mathbf{S}^{*T} \mathbf{A} \mathbf{S} \quad (4.6)$$

subject to

$$0 \leq \rho(X) \leq 1$$

where \mathbf{S} refers to either \mathbf{t}_{mn} or \mathbf{r}_{mn} , and \mathbf{A} is a constant diagonal matrix of size $(2N_m + 1)(2N_n + 1)$ such that

$$\mathbf{A} = \begin{bmatrix} a_1 & 0 & 0 & 0 \\ 0 & a_2 & 0 & 0 \\ 0 & 0 & \ddots & 0 \\ 0 & 0 & 0 & a_{(2N_m+1)(2N_n+1)} \end{bmatrix} \quad (4.7)$$

where N_m and N_n denote the highest modes included in the sums in Eqs.4.1 and 4.2. In essence, \mathbf{A} is used to collect only the modal reflection or transmission coefficients corresponding to the propagating (energy carrying) modes by setting

$$a_k = \begin{cases} 1 & ; \text{ if } k \text{ corresponds to a propagating mode} \\ 0 & ; \text{ otherwise} \end{cases} \quad (4.8)$$

in Eq.4.7. Note that for a mode with indices m and n , a real γ_{mn} indicates a propagation mode and an imaginary γ_{mn} indicates an evanescent mode.

4.3.1 Sensitivity analysis

Gradients of the objective function J with respect to the element material effective density ρ_e are computed using an adjoint variable approach as

$$\frac{dJ}{d\rho_e} = \frac{\partial J}{\partial \mathbf{S}^*} \frac{\partial \mathbf{S}^*}{\partial \rho_e} + \frac{\partial \mathbf{S}}{\partial \rho_e}^T \left(\frac{\partial J}{\partial \mathbf{S}} \right)^T = \lambda_e^T P_e + \lambda_e^{*T} P_e^* \quad (4.9)$$

$$\frac{dJ}{d\rho_e} = \lambda_e^T P_e + (\lambda_e^T P_e)^* \quad (4.10)$$

Adjoint variable λ can be obtained by solving the adjoint problem

$$K^T \lambda = \left(\frac{\partial J}{\partial \mathbf{E}} \right)^T = \left[\frac{\partial J}{\partial \mathbf{S}^*} \frac{\partial \mathbf{S}^*}{\partial \mathbf{E}} + \left(\frac{\partial \mathbf{S}}{\partial \mathbf{E}} \right)^T \left(\frac{\partial J^T}{\partial \mathbf{S}} \right) \right]^T \quad (4.11)$$

and

$$\frac{\partial J}{\partial \mathbf{S}^*} = \mathbf{S}^{*T} \mathbf{A}, \quad \left(\frac{\partial J}{\partial \mathbf{S}} \right)^T = \mathbf{A} \mathbf{S} \quad (4.12)$$

where

$$\frac{\partial \mathbf{S}}{\partial \mathbf{E}} = \frac{1}{T_x T_y} \int_{\Gamma_{in}} \phi \psi_{mn}^* d\Gamma \quad (4.13)$$

if $\mathbf{S} = \mathbf{r}_{mn}$ and

$$\frac{\partial \mathbf{S}}{\partial \mathbf{E}} = \frac{1}{T_x T_y} \int_{\Gamma_{out}} \phi \psi_{mn}^* d\Gamma \quad (4.14)$$

if $\mathbf{S} = \mathbf{t}_{mn}$.

Vector P_e is computed using

$$P_e = -\frac{\partial \mathbf{K}_e}{\partial \rho_e} \mathbf{E}_e = k_0^2 p \rho_e^{p-1} (\epsilon_a - \epsilon_b) \int_{\Omega_e} \tilde{\phi}^e \phi^e d\Omega \mathbf{E}_e \quad (4.15)$$

Gradients with respect to the design variable X are computed using the chain rule as

$$\frac{dJ}{dX} = \frac{dJ}{d\rho} \frac{\partial \rho}{\partial X} \quad (4.16)$$

where

$$\frac{\partial \rho_e}{\partial X_i} = \begin{cases} 1 & ; \text{ if } \rho_e \text{ is controlled by } X_i \\ 0 & ; \text{ otherwise} \end{cases} \quad (4.17)$$

4.3.2 Projection of the effective density

To facilitate convergence to a binary solution, a projection technique is used [54], [55]. The effective density ρ is projected to $\bar{\rho}$ using a smooth Heaviside function H_β :

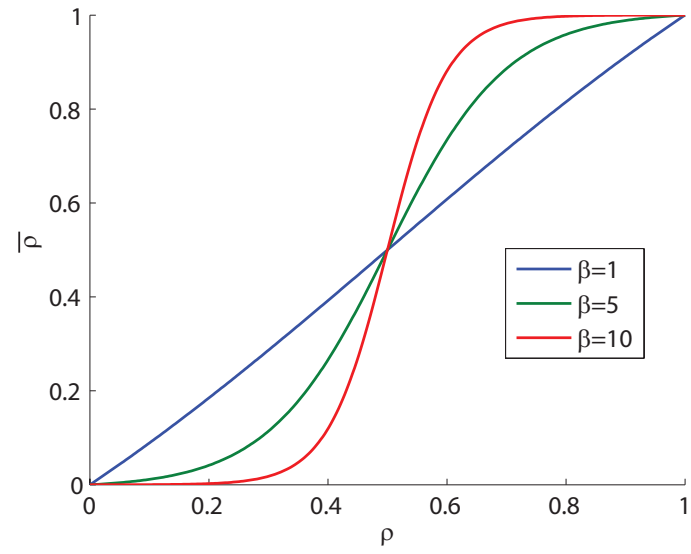
$$\bar{\rho} = H_\beta(\rho) = \frac{\tanh(\beta\eta) + \tanh(\beta(\rho - \eta))}{\tanh(\beta\eta) + \tanh(\beta(1 - \eta))} \quad (4.18)$$

which approaches a step function as $\beta \rightarrow \infty$. Parameter β is used to control smoothness and, and η is used to control the threshold value. The projection function is plotted for various values of β and η in Fig.4.2(a) and (b), respectively, to illustrate the effect of β and η .

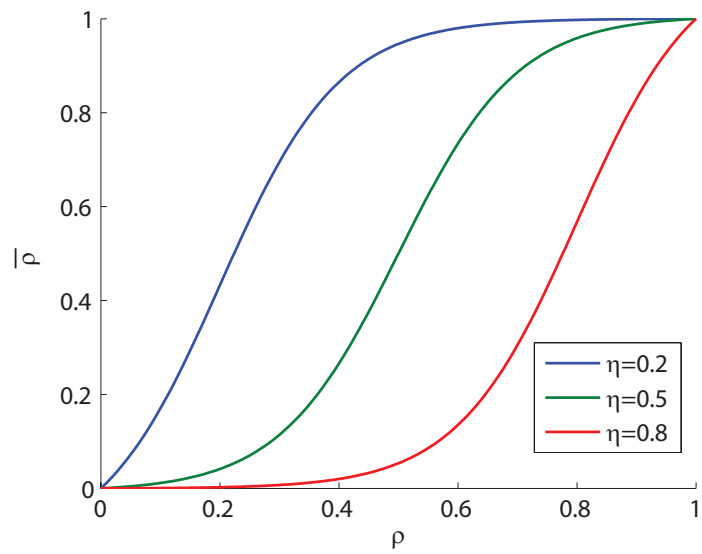
The projected density $\bar{\rho}$ is used to describe the material distribution in the analysis.

4.3.3 Numerical example

The use of the approach is illustrated using a simple example. A material with relative electric permittivity $\epsilon_a = 2.25$ is distributed in a vacuum background ($\epsilon_b = 1$), within a design domain Ω_D that occupies the entire computational domain Ω . Domain Ω is described by tiling vectors $\mathbf{e}_x = (Tx, 0, 0) = (1.5\mu m, 0, 0)$ and $\mathbf{e}_y = (0, Ty, 0) = (1.5\mu m, 0, 0)$ and thickness $1.0\mu m$, in the z -direction, and discretized by 20x20x20 brick elements. The material below the input boundary Γ_{in} in Fig.4.1 is vacuum, and the space above the output boundary Γ_{out} is assumed to be filled with the inclusion material with ϵ_a . Normal incidence with the vacuum wavelength $\lambda = 0.6\mu m = 0.4Tx$ and the magnitude $|\mathbf{E}_{in}| = 1$ is applied. Values



(a) $\eta=0.5$



(b) $\beta=5$

Figure 4.2: Projection function

Table 4.1: Parameters used in the example

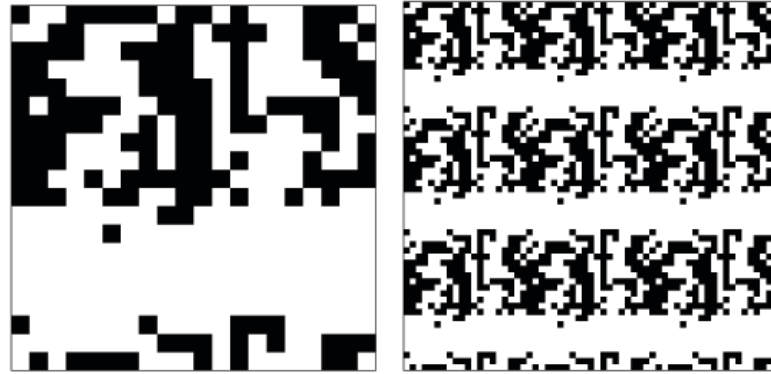
Parameter	Tx	Ty	λ	ϵ_a	ϵ_b
Value	$1.5\mu\text{m}$	$1.5\mu\text{m}$	$0.6\mu\text{m}$	2.25	1

of the parameters used in the example are summarized in Table 4.1. The highest mode order included in the wave expansion N_m is set to 2.

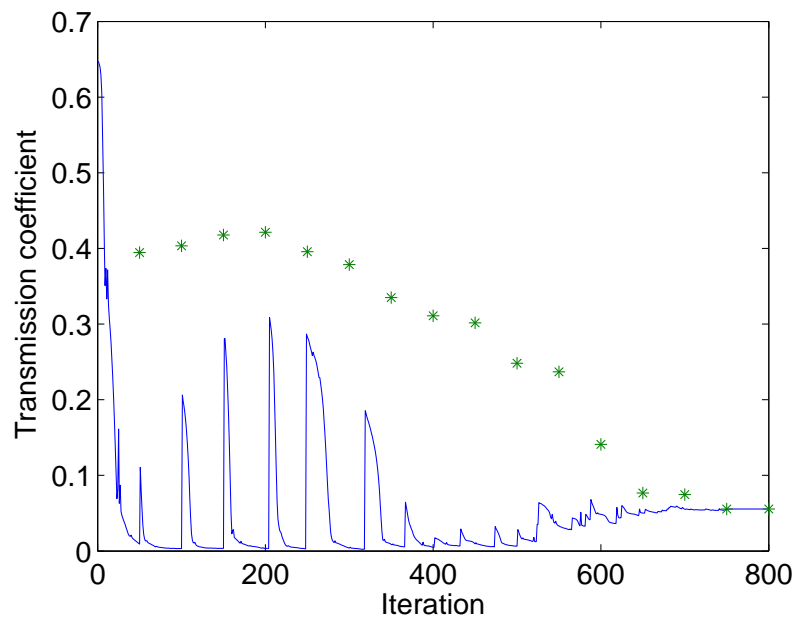
The initial design has uniform permittivity with $\rho = 0.5 \forall (x, y) \in \Omega_D$. The projection function in Eq.4.18 is used to facilitate convergence to a binary solution. Parameter η is set to 0.5, and β is set to 1 and is increased gradually during the optimization iterations.

The objective is to find a configuration that minimizes transmission, which corresponds to setting $\mathbf{S} = \mathbf{t}_{mn}$, and an optimal solution is found using the MMA [51].

The optimal solution, the 3x3 tile associated with the optimal solution and the iteration history are shown in Fig.4.3(a), (b) and (c), respectively, where black color corresponds to material with ϵ_a and white is vacuum in Fig.4.3(a) and (b). The peaks at 51, 101, 151, etc. iterations seen in the iteration history in Fig.4.3(b) are due to the increased value of parameter β used in the projection function in Eq.4.18. As β increases, the projection function becomes closer to a step function, allowing a smaller number of effective densities to take intermediate values. The rate at which β changes should be adjusted carefully; increasing β too slowly will require many iterations until convergence is achieved, and increasing β too quickly will push intermediate effective densities (ρ) towards 0 or 1 too aggressively, leading to poor convergence. Since H_β for a large β has small gradients near $\rho = 0$ and $\rho = 1$, once ρ is pushed to a value close to either 0 or 1, it will get “stuck” at that value. Parameter β is increased by multiplying the previously set value by 1.355 whenever the maximum change in design variables is smaller than 0.01 and the change in the objective function is smaller than 10×10^{-4} . The transmission coefficient of the binary solution obtained by



(a) Optimal solution (b) 3x3 tile of the solution



(c) Iteration history

Figure 4.3: Optimal solution and iteration history

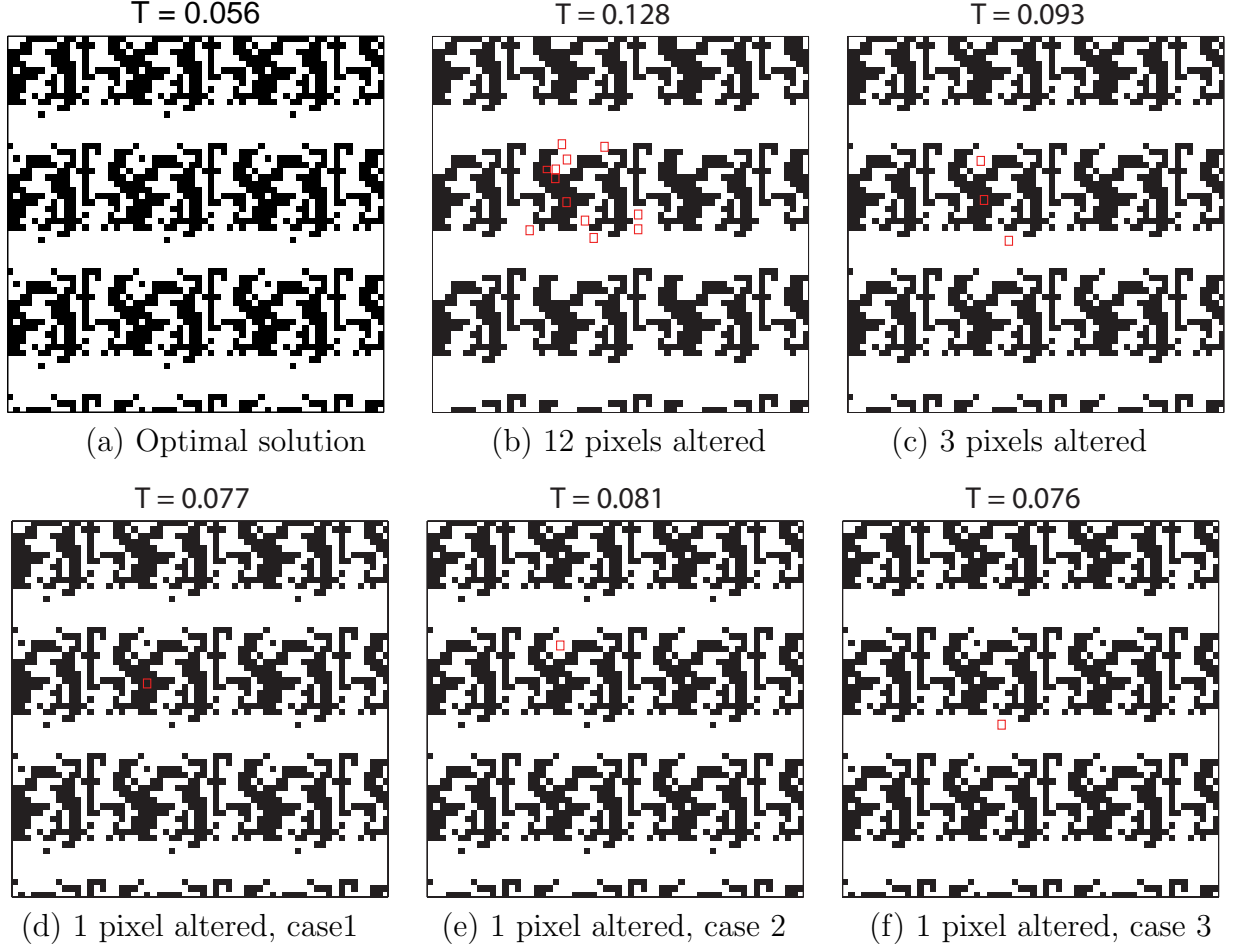


Figure 4.4: Processed solutions

applying a threshold at $\rho = 0.5$ is shown for every 50 iterations, using an asterisk (*) in Fig.4.3(c). It can be observed that the objective value of the thresholded design approaches that of the unprocessed design towards the end of the optimization process. After 800 iterations, $\beta = 4.08 \times 10^{11}$, and we obtain an optimal solution with no “gray” regions, with the transmission coefficient $T = 0.056$.

In Fig.4.3(a), we observe that several pixels are surrounded by pixels of a different color. To evaluate the performance of simpler designs in the neighborhood of the optimal solution, some designs are obtained by altering some of the pixels that are surrounded by a different color, indicated by red squares, and the transmission coefficient is measured. The optimal

solution with its transmission coefficient is shown in Fig.4.4(a) again. The alternate designs and their transmission coefficients are shown in Fig.4.4(b)-(d). It can be seen that as a larger number of pixels is altered, performance becomes worse. To obtain simpler designs, one needs to use a filtering technique during the optimization process instead of relying on image processing after obtaining an optimal solution.

4.3.4 Conclusions

A topology optimization method was used to design a 3D structure with periodicity in the x - and y -directions. The material distribution is controlled by a mapping that varies in the xy -plane and uniform in the z -direction. A structure that minimizes transmission for an incidence of a prescribed frequency was found. The effective density ρ was projected, using a smooth Heaviside function, to $\bar{\rho}$ to be used in the analysis. Use of the parameter β to adjust the sharpness of the projection function needs great care, in order to achieve a fast and stable convergence.

Chapter 5

Origami Tunable Surfaces for Electromagnetic Applications

The use of the concept of origami for engineering applications is gaining interest as an integral part of innovative design processes. Origami is a Japanese word for “art of paper folding”, a tradition that appears in many cultures [56]. In origami design, the construction of a 2D or 3D geometry from a flat, usually square sheet is achieved through a combination of simple folding steps.

Today, use of origami in engineering includes collapsible structures, structures that can be folded to take up only a small fraction of the space taken by the final, unfolded configuration of the structure. Examples from the aerospace industry include foldable satellite structures such as solar panels [57][58].

In this chapter, the use of the concept of origami in design of electromagnetic devices in [59] and [60] is discussed. In particular, shifting of resonance frequencies of frequency selective surfaces and tunable metamaterials is discussed.

5.1 Origami Tunable Frequency Selective Surfaces

Frequency selective surfaces (FSSs) are used as band-pass or band-stop surfaces to filter electromagnetic signals to enhance the operation of various electromagnetic systems such as radar, communication and sensing systems. The capability of adjusting the working frequency of FSSs while in operation expands the utility of devices in advanced applications. Tuning is commonly achieved using lumped components such as varactors [61], [62]. Another method is to use special types of substrates such as liquid crystals [63]-[65] or ferrites [66], wherein a 15-20% shift of a resonance frequency can be achieved by altering the properties of the substrate through the application of an external excitation. Concepts based on changing the geometric configuration of metallic inclusions by means of switches have also been proposed [67]. A drawback of such designs of tunable FSSs is that they require continuous excitation from an external source, which increases the energy consumption of the system.

A new approach to designing tunable FSSs based on the concept of origami is introduced in [59]. A layer of a conventional FSS, composed of a periodic array of conducting or dielectric elements printed on a flat substrate, is folded into a periodic pattern in an origami-like fashion. The transformation of the surface geometry of the layer through a process of folding and unfolding is applied to invoke tuning of the working frequency of FSSs. Such an FSS requires an external energy input only at instances when the working frequency is to be adjusted.

5.1.1 Miura-ori

An example of a folding pattern that can be used to design a tunable FSS is the well known Miura-ori, shown in Fig.5.1(a). This pattern has one control parameter that determines a

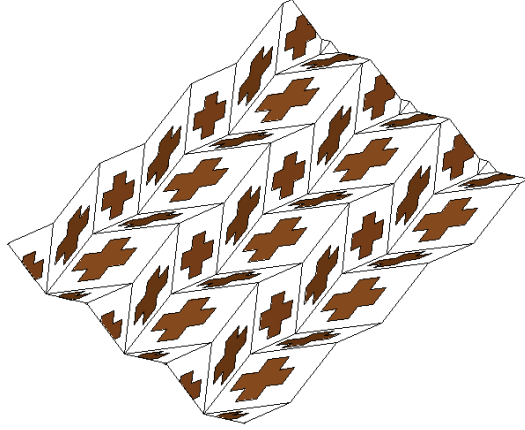


Figure 5.1: Miura-ori

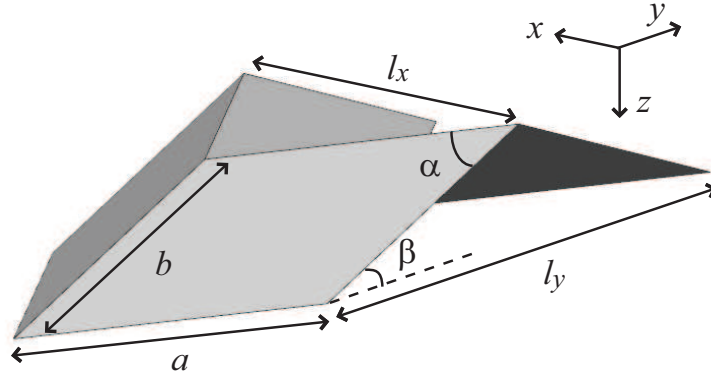


Figure 5.2: Unit cell of Miura-ori

folding state that ranges from flat to highly folded and remains periodic throughout the motion. Varying this parameter changes the relative location of the prints of conducting material, and thus the frequency of resonance. Computer simulations and experiments are conducted to test the performance of the origami tunable FSS.

The unit cell of the chevron origami structure of Fig.5.1(a) consists of four parallelogram-shaped facets, as shown in Fig.5.1(b). The cell is repeated periodically along two tiling directions \hat{x} and \hat{y} with lengths l_x and l_y . The angle β determines the folding state. The other geometric parameters, a , b and α , describe the parallelogram that forms the unit cell.

When $\beta = 0^\circ$ the sheet is flat. As β is increased, lengths l_x and l_y change, as do the orientations of elements printed on the sheet. The length parameters are expressed in terms of β as:

$$\begin{aligned} l_x &= 2a \cos \gamma \\ l_y &= 2b(\sin \gamma \cos \alpha + \cos \gamma \cos \beta \sin \alpha) \end{aligned} \tag{5.1}$$

where $\gamma = \tan^{-1} [1/(\tan \alpha \cos \beta)]$ is an intermediate value defined for convenience. Each facet (a parallelogram plane in case of Miura-ori) within the unit cell may be decorated, for example, with an element made of a thin conducting print to make the folded surface into a working FSS in the radio frequency (RF) range.

5.1.2 Performance evaluation

Performance of the designed FSSs is done by analyzing the electromagnetic wave propagation within the representative cell of a periodic structure and computing the reflection and transmission coefficients ($|S_{11}|$ and $|S_{21}|$) using a full-wave solver HFSS [68], based on finite element analysis. An example of a setup is shown in Fig.5.3.

For Miura-ori, the projection of the representative cell follows a chevron shape. The periodic boundary conditions are used at all six sides. At the input (top) and output (bottom) boundaries, PMLs described in 2.3.2 are used. A thin dielectric sheet as well as the conducting prints are modeled using the impedance boundary condition.

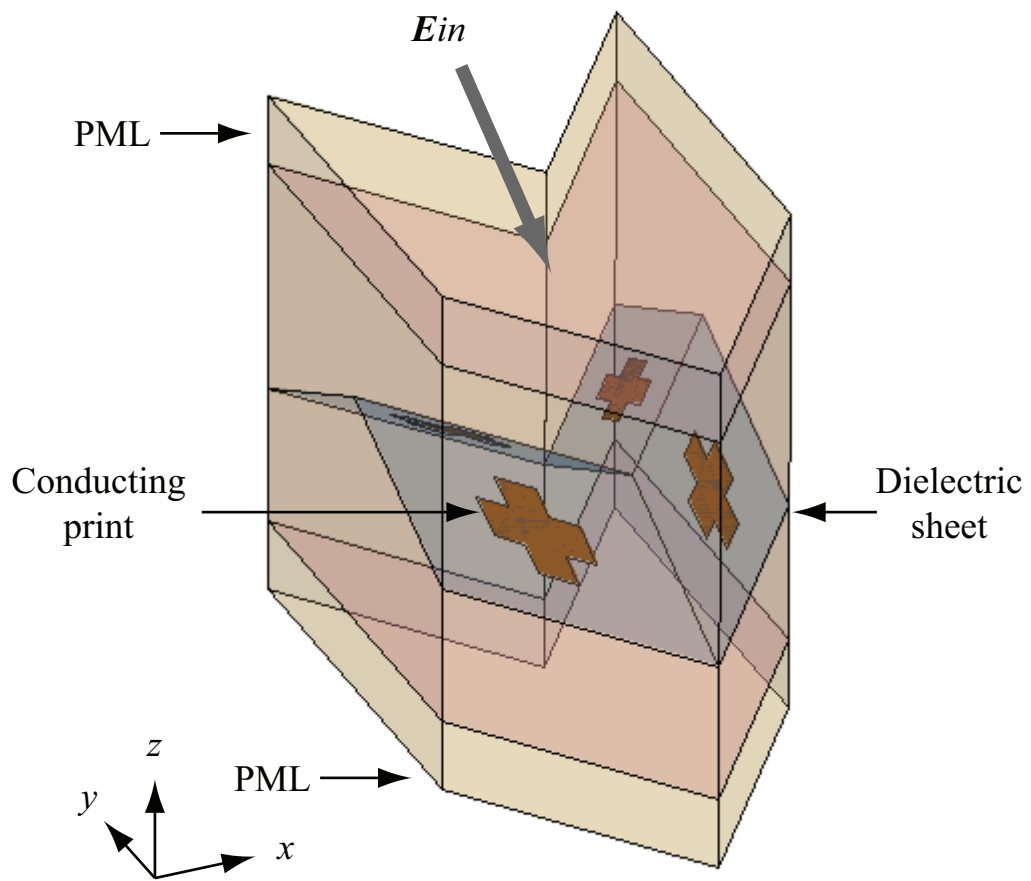


Figure 5.3: Analysis setup

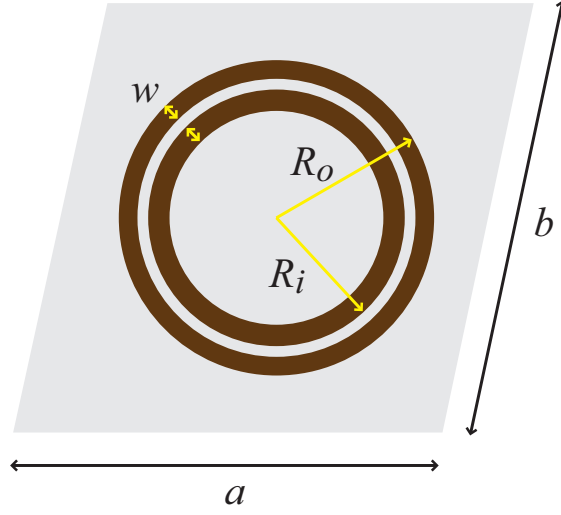


Figure 5.4: Concentric ring conducting element

5.1.3 Choice of conducting element types

Variations of commonly used conducting prints are evaluated for their performance in terms of the amount of shift in the resonance frequency and the strength of resonance.

5.1.3.1 Concentric double ring copper prints

First, concentric rings, shown in Fig.5.4 are considered.

Consider a design with a unit cell described by $a = 25\text{mm}$, $b = 20\text{mm}$ and $\alpha = 60^\circ$. Copper elements with $R_o=5.45\text{mm}$, $R_i=4.8\text{mm}$ and $w=0.4\text{mm}$ are placed on facets of the folded sheet. The sheet is assumed to be very thin, and the dielectric constant of unity is used in simulations. The FSS is illuminated by a normally-incident plane wave with the electric field polarized along the x -axis and the propagation vector along the z -axis. The transmission responses of an FSS in folded states described by $\beta = 0^\circ, 20^\circ, 40^\circ$ and 60° are plotted in Fig.5.5. Computation of the transmission coefficient S_{21} was undertaken using HFSS.

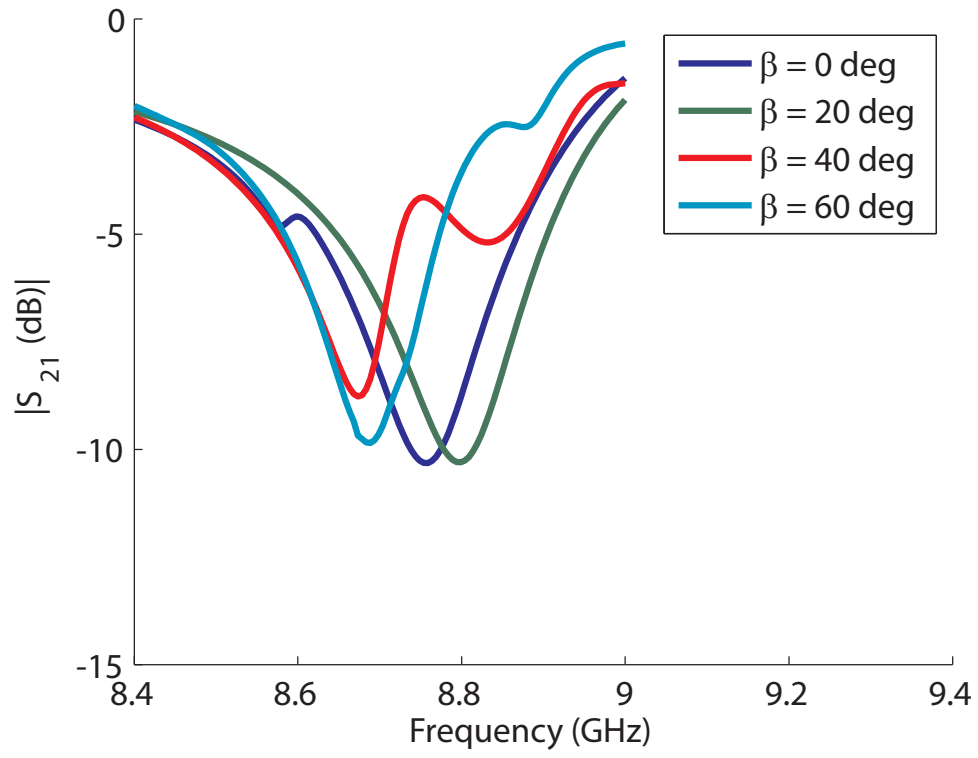


Figure 5.5: Simulated transmission coefficient $|S_{21}|$ for concentric rings at normal incidence

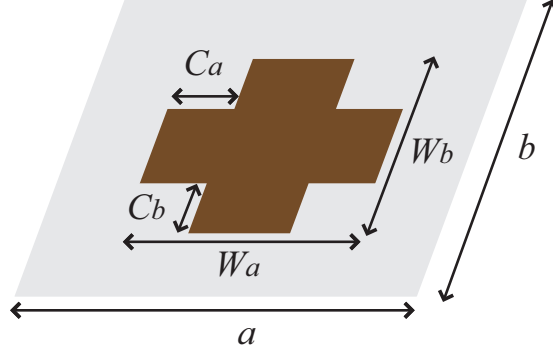


Figure 5.6: Skewed cross-shaped conducting element

The amount of frequency shift that occurs as β is changed between angles β_1 and β_2 is computed as

$$\frac{\Delta f}{f_{mid}} = \frac{|f_{\beta 1} - f_{\beta 2}|}{0.5 (f_{\beta 1} + f_{\beta 2})} \quad (5.2)$$

where f_{mid} is the midpoint between frequencies $f_{\beta 1}$ and $f_{\beta 2}$. Using this formula, the shift in resonance observed in Fig.5.5 is 1.4%, as β is changed from 0° to 60° . The value of transmission coefficient is kept under -10dB, except at $\beta = 40^\circ$.

5.1.3.2 Cross-shaped copper prints

Skewed cross prints, shown in Fig.5.6 are considered next, where the arms of the crosses are aligned with the sides of the parallelogram.

Consider a design with a unit cell described by $a = 19.6\text{mm}$, $b = 14.7\text{mm}$ and $\alpha = 45^\circ$. Copper elements with $W_a = W_b = 7.3\text{mm}$ and $C_a = C_b = 2.2\text{mm}$ are placed onto the facets of the cells. A sheet of paper is chosen as the substrate, and a dielectric constant of 3 and thickness 0.1mm are used in simulations. The FSS is illuminated again by a normally-incident plane wave with the electric field polarized along the x -axis and the propagation vector along the z -axis. The transmission responses of an FSS in folded states described by

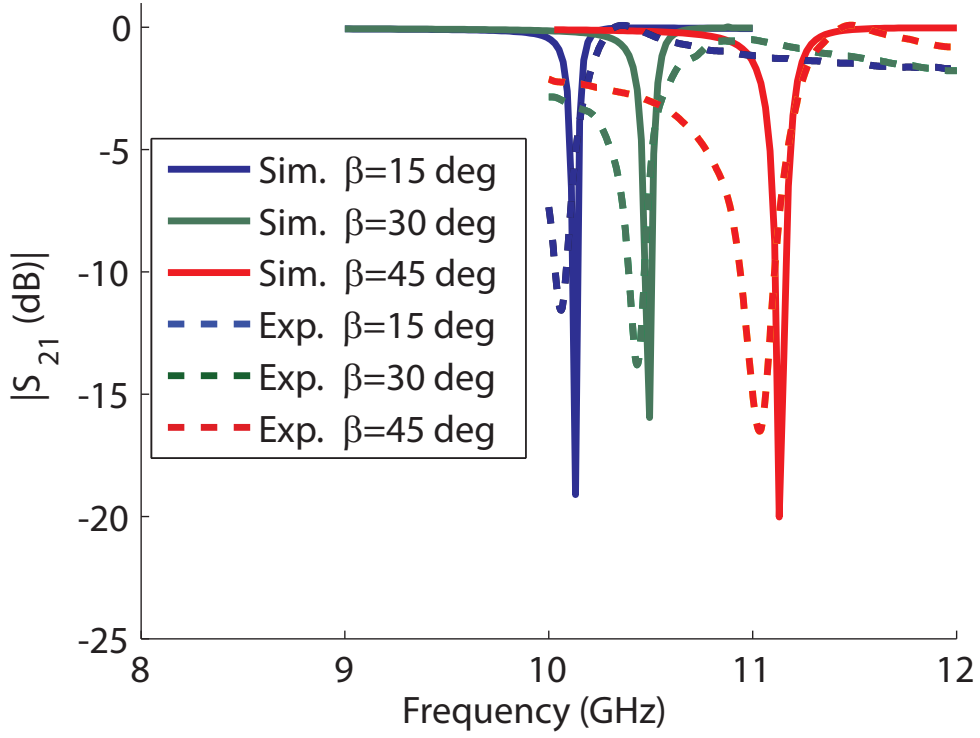


Figure 5.7: Simulated (Sim.) and measured (Exp.) transmission coefficient $|S_{21}|$ at normal incidence

$\beta = 15^\circ$, 30° and 45° are plotted in Fig.5.7. As β increases, the resonance shifts continuously to a higher frequency, with a shift of 19% occurring as β changes from 0° to 60° . The value of transmission coefficient is kept well under -10dB at all values of β examined. Both in terms of the amount of shift in resonance frequency and the strength of resonance, skewed cross-shaped elements are more desirable, compared to concentric rings.

5.1.3.3 Summary

The frequency shift observed is due both to the changes in interactions between the incident field and the metallic structures caused by the change in unit cell size, and to mutual interactions between the structures. The interactions and thus the resonance behavior are

highly dependent on the type of folding pattern, the shape of the conducting elements, and the properties of the substrate. It has been shown that a sheet folded into Miura-ori and decorated with concentric rings does not show much tunability. This is because with circular rings, the location of the resonance depends primarily on the circumference of the rings, but the spacing between the printed elements is not as important as with cross-shaped prints.

5.1.4 Angle dependency

To investigate the resonance frequency dependency on angle of incidence, the performance of the folded FSS is evaluated for oblique incidence. The transmission responses of an oblique incidence case are plotted in Fig.5.8. Here the original z-directed propagation vector is rotated to lie in the y-z plane at an angle $\theta = 30^\circ$ to the z-axis, with the electric field still polarized along the x-axis. A similar trend as in the normal incidence case is observed; the resonance frequency increases as the folding angle β increases. The three curves shown in Fig. 5.9 summarize the dependency of resonance frequency on β for three different angles of incidence $\theta = 0^\circ, 30^\circ$ and 60° . One can observe the same trend of increasing resonance frequency with β in all three curves. It is worth mentioning that there is a band of frequencies shared by all three curves. Within this frequency band, there is a β that brings the resonance frequency to a desired location for any (of the three) angles of incidence. This range of frequencies is indicated as a gray band in Fig.5.9.

5.1.5 Polarization dependency

Next, polarization dependency of a folded FSS is investigated. An incidence with the electric field polarized along the y-axis is used in simulation. In this case, much weaker resonances

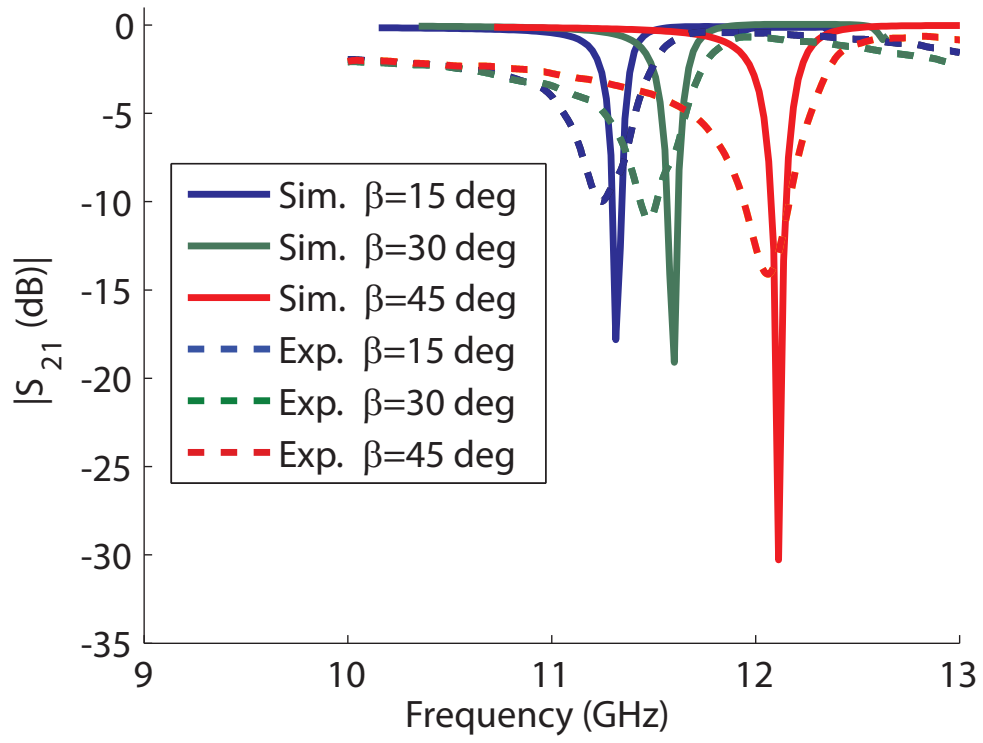


Figure 5.8: Simulated and measured transmission coefficient $|S_{21}|$ at oblique incidence at $\theta=30^\circ$

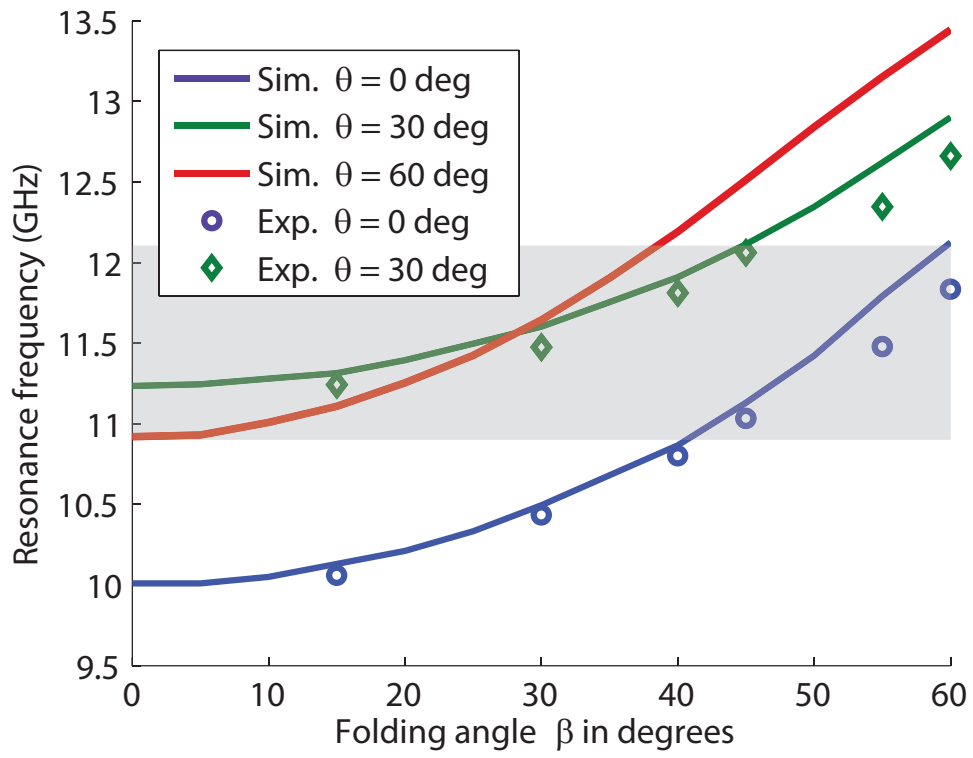


Figure 5.9: Simulated and measured resonance frequencies, f_{res} in GHz

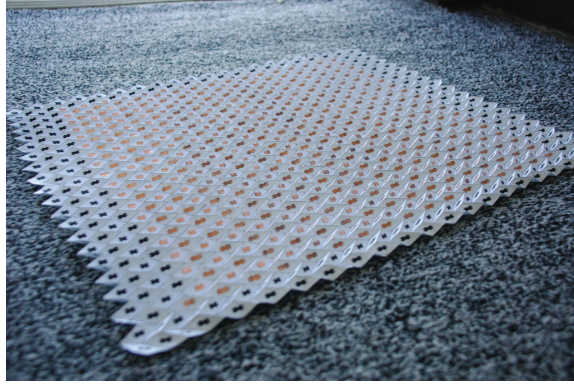


Figure 5.10: Fabricated origami tunable FSS

are observed, and therefore the usability of the folded FSS is significantly degraded for the orthogonal polarization. A different design strategy using symmetric designs may resolve this problem.

5.1.6 Experiment

A prototype FSS with an origami geometry identical to that used in simulations was constructed and its performance was measured to validate the origami tuning concept. The folding crease pattern of a 40 by 40 element array was printed on a sheet of paper, and the sheet was folded by hand, producing the chevron structure of Fig.5.1. When flat ($\beta=0^\circ$), the array measures 55.3 cm by 58.7 cm. Cross-shaped elements were chemically etched on strips of copper tape, and one element was attached to each facet of the folded pattern. The fabricated foldable FSS is shown in Fig.5.10. A more sophisticated fabrication method relying on automated procedures is envisioned for eventual manufacture of foldable FSSs.

Measurement of the transmission properties of the prototype FSS was undertaken as follows. The surface was folded to a desired angle β and attached to a foam sheet using removable pins. For small values of β , clamps were used to hold the sheet in place, as

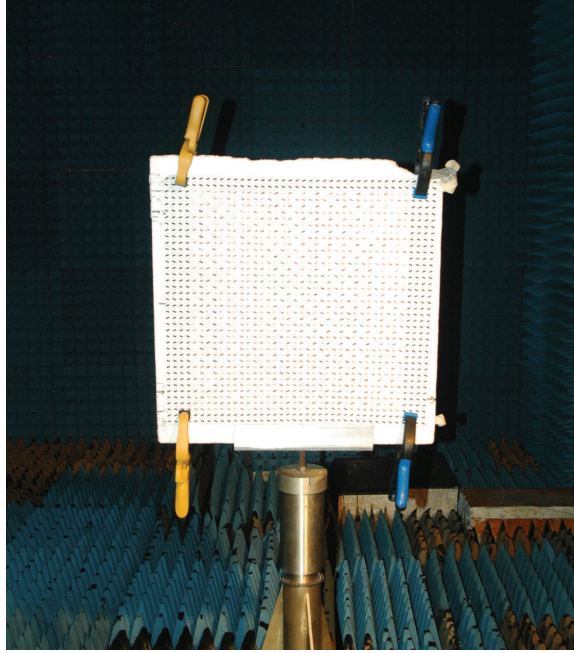


Figure 5.11: Experiment setup for normal incidence

shown in Figs.5.11 and 5.12. The sheet was placed on an adjustable stand in the center of an anechoic chamber of size 12 by 12 by 24 feet (3.66 by 3.66 by 7.32 m). American Electronics Laboratory model H-1498TEM-horn antennas were placed against opposite walls and attached through rigid coaxial cable to an HP 8510C vector network analyzer, which was used to measure the transmission coefficient S_{21} through the surface. Nylon dielectric lenses were placed in front of the antennas to create a focused beam with a roughly Gaussian profile at the position of the FSS; at 10 GHz the spot diameter of the beam is about 20 cm, and the phase across the spot is approximately uniform. Focusing of the beam is important to eliminate termination effects, such as edge diffraction, and interaction of the beam with the supporting structures. Calibration was accomplished using a through-measurement with the surface absent, first subtracting the background response measured with a metal plate blocking the beam.

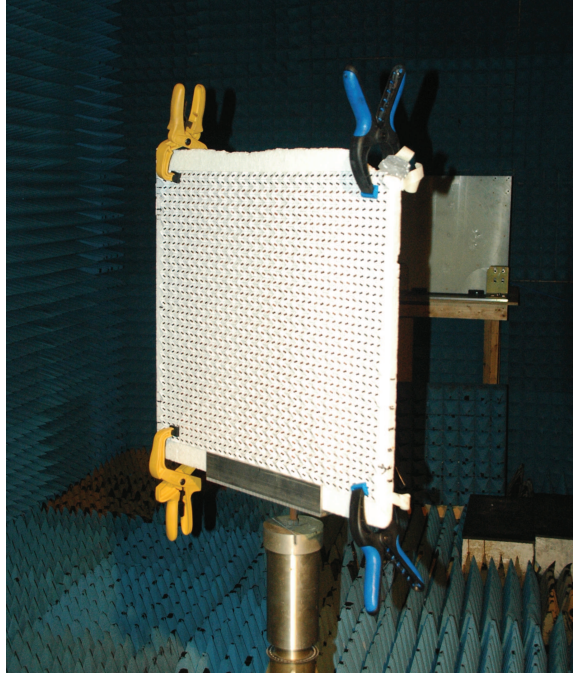


Figure 5.12: Experiment setup for oblique incidence at $\theta = 30^\circ$

Transmission responses measured using normal incidence (experimental setup shown in Fig.5.11) and an oblique incidence angle of $\theta=30^\circ$ (experimental setup shown in Fig.5.12) are plotted in Fig.5.7 and Fig.5.8, respectively. The measured resonance frequencies for various folding angles β are very nearly those predicted by simulation, as summarized in Fig.5.9. Note that the measured resonance curves are not as sharp and pronounced as predicted by simulations. This could be because the focused incident field used in the experiment illuminates only a portion of the FSS array, and simulations assume the array is infinite and plane-wave illuminated. Also, the loss in the paper used to construct the surface and in the glue used to hold the crosses in place may lead to resonances with a lower quality factor than predicted in simulation. Measurement at an incidence angle of $\theta=60^\circ$ was not undertaken because the FSS profile presented to the incident beam is too narrow at this angle to ignore edge effects. Also, the orthogonal polarization state was not measured since it was shown in

simulation that in this case resonances are not strongly excited.

5.1.7 Conclusions

The feasibility of tuning an FSS by simple mechanical means is demonstrated using a Miura-ori structure with cross-shaped metallic prints in simulations and experiments. By changing the folding angle from 0° to 60° , the resonance frequency may be shifted by 19%. Tunability performance was observed to be dependent on the type of conducting prints.

5.2 Origami Tunable Metamaterials

A well-known realization of metamaterials is achieved using SRRs, proposed by Pendry [27]. For instance, edge-coupled SRRs are formed by two concentric, coplanar split rings made of a thin layer of conducting material printed on a dielectric substrate. It is possible to arrange SRRs in a three-dimensional array to make a metamaterial that exhibits resonance behavior when excited by an electromagnetic wave with a magnetic field oriented normally to the plane of the rings. This resonance is enabled by a capacitance dominated by the proximity of the inner and outer edges of the rings, and by a loop inductance. The frequency at which the resonance occurs can be determined based on the geometry of the rings, the material properties of the conducting prints and the substrate, and on the thickness of the substrate.

One disadvantage of metamaterials based on SRRs is a narrow bandwidth. To expand the utility of these types of metamaterials, researchers have investigated various ways to tune the resonance frequency of metamaterials in response to changes in environment or operating mission. Similar to the design of tunable FSSs, incorporation of lumped components such as varactors, diodes and potentiometers, in an array of resonating structures is a common

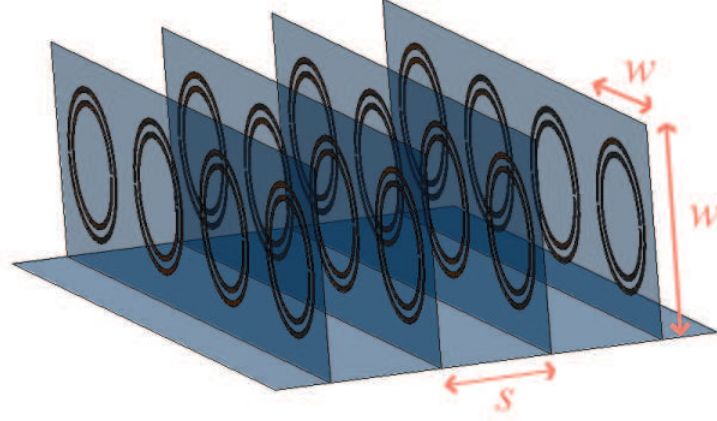


Figure 5.13: Corrugated sheet with SRRs, $\alpha = 0^\circ$

approach to achieve tunability [69]-[74]. For example, a varactor loaded split ring resonator has been used to achieve a 30% shift in resonance in an RF range [70]. A wider range of tuning (65%) has been achieved by using a combination of multiple switches and a varactor placed in a spiral resonator [75]. Another approach is to use a host medium whose dielectric properties can be altered [76]-[79], again, in a similar manner as in the design of FSSs.

A new approach to designing tunable metamaterials based on the concept of origami ([60]) is introduced here, where SRRs are printed on a surface folded into a periodic pattern that can be un-folded by controlling one free folding parameter. The inner and outer rings are printed on different surfaces so that when the folding parameter is varied, the gap between the rings, and thus the capacitance of the resonators, is altered.

5.2.1 Design of an origami tunable metamaterial

A simple example of an arrangement that can be used for the design of tunable metamaterials is illustrated in Fig.5.13. The folding pattern is that of a sheet folded in a corrugated arrangement, which may be unfolded to form the surface shown in Fig.5.14.

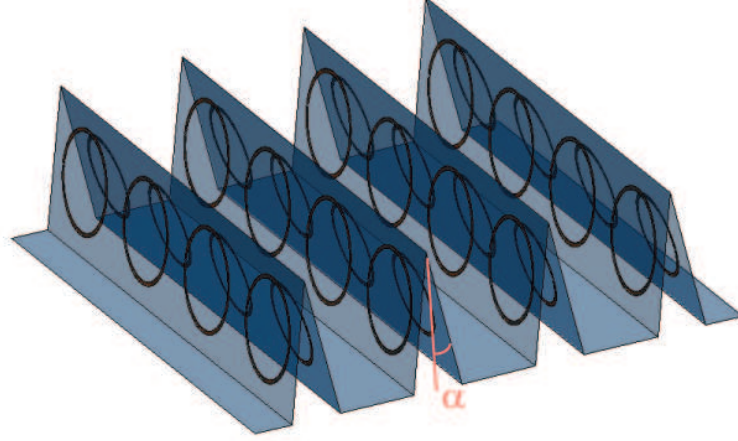


Figure 5.14: Corrugated sheet with SRRs, $\alpha = 10^\circ$

A thin dielectric sheet is decorated with SRRs, with each ring in an SRR pair placed on opposite faces of the corrugation. When the structure is completely folded, the rings lie on the same plane and form an SRR centrally embedded within a dielectric sheet of thickness $2d$. As the sheet unfolds, an air gap opens between the adjacent dielectric surfaces and the rings separate. A unit cell containing a single ring pair is shown in Fig.5.15, and this cell is repeated in the direction perpendicular to the corrugation. Thus the folding pattern is periodic in one direction and uniform in the other, perpendicular direction. The pattern has one free parameter, represented here by the angle α , that can be varied to change the capacitance of the rings. When $\alpha = 0^\circ$, the array of SRRs is oriented vertically to the plane of the corrugation. When the edges of the folded sheet are pulled apart along the corrugation direction, the angle α increases (Fig.5.14) and the separation between the two split rings increases. Excitation is by a plane wave incident from above such that the magnetic field is aligned along the axis of the fully folded rings ($\alpha = 0^\circ$).

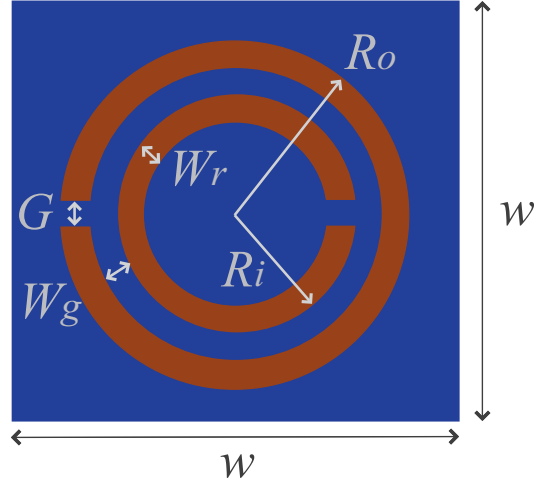


Figure 5.15: Origami metamaterial unit cell design

5.2.2 Demonstration of tuning of a metamaterial

The full-wave solver HFSS was used to analyze the electromagnetic behavior of the origami metamaterial, using periodic boundary conditions and PMLs as in Sec.5.1.2. An incident plane wave with propagation direction perpendicular to the sheet was used to excite the rings, with its magnetic field oriented normal to the plane of the rings in the $\alpha = 0^\circ$ configuration. The transmission coefficients (S_{21}) were computed using the field solution found in simulations.

A sample design was analyzed where the resonance frequency of the fully folded ($\alpha = 0^\circ$) structure is placed in the lower portion of the F-band, at 5.29 GHz. The unit cell parameters from Fig.5.15 are given in Tab.5.1, while the spacing in Fig.5.13 is set to $s = 4\text{mm}$. Note that W_g is the separation of the ring edges when $\alpha = 0^\circ$. Both rings were assigned the conductivity of copper, and the substrate was chosen to be 0.5 mm thick with the properties of Rogers Duroid 5870 (dielectric constant $\epsilon_r = 2.33$ and loss tangent $\tan \delta = 0.0012$.)

Transmission and reflection coefficients are plotted in Figs.5.16 and 5.17, respectively, for $\alpha=0^\circ$ - 10° in 2° increments. The transmission and reflection curves show that the resonance

Table 5.1: Parameters used in sample F-band design

Parameter	Value (mm)
w	7
R_o	2.2
R_i	1.82
W_r	0.2
W_g	0.18
G	0.25

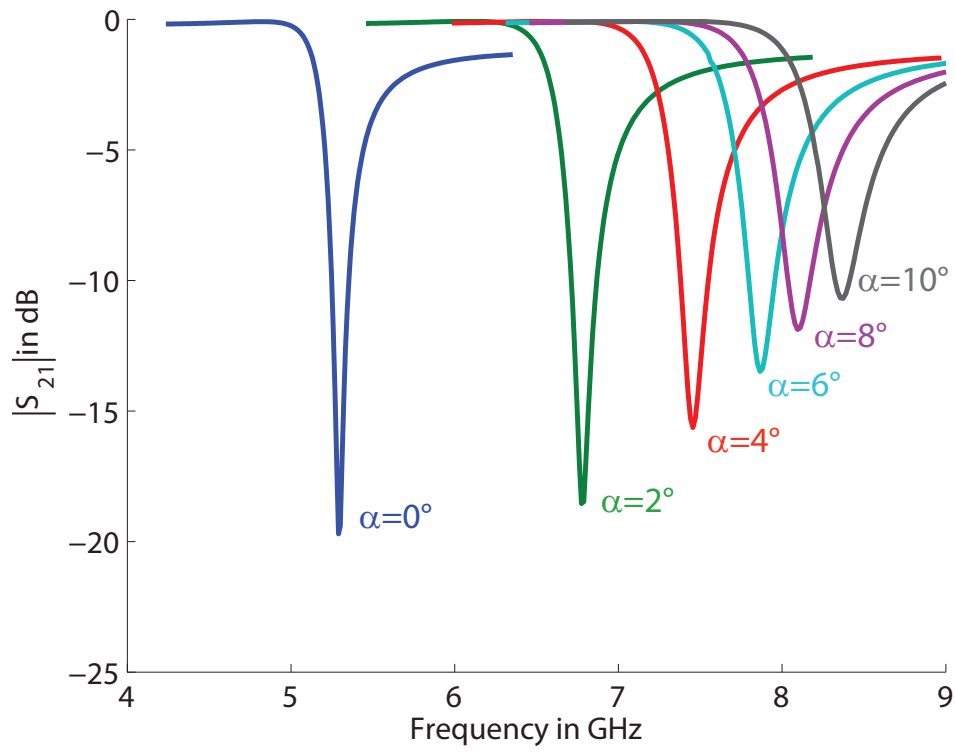


Figure 5.16: Transmission coefficient, $|S_{21}|$

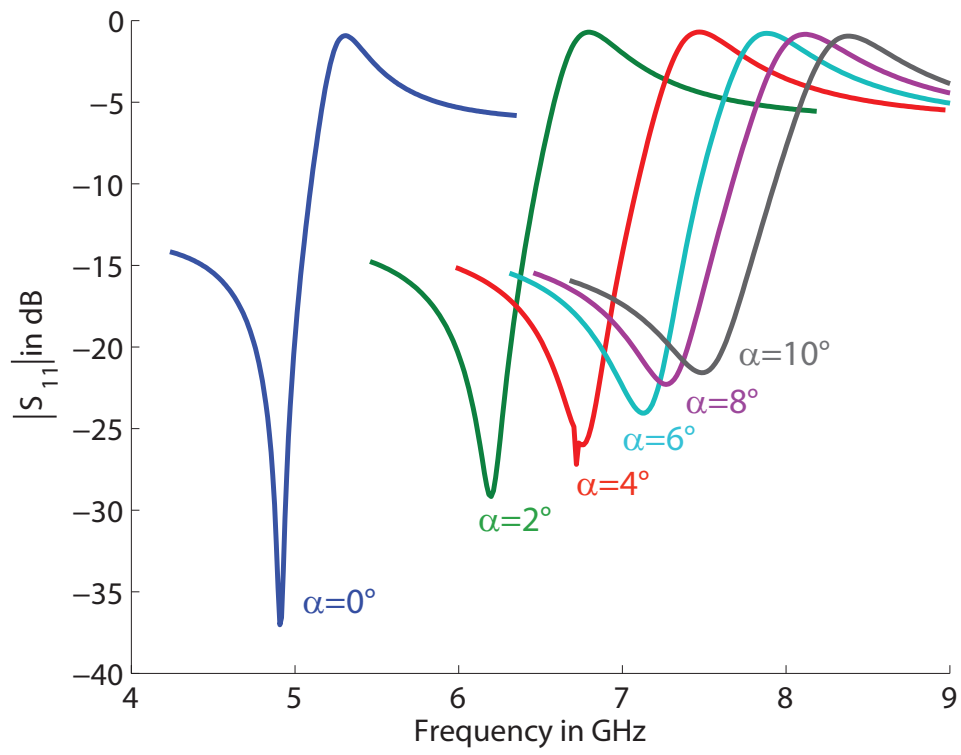


Figure 5.17: Reflection coefficient, $|S_{11}|$

Table 5.2: Resonance frequencies found using HFSS

α (deg)	f_r (GHz) $\epsilon_r = 10.2$	f_r (GHz) $\epsilon_r = 2.33$	f_r (GHz) $\epsilon_r = 1$
0	2.56	5.29	7.97
1	3.79	6.32	8.22
2	4.12	6.78	8.53
3	4.33	7.13	8.82
4	4.50	7.46	9.11
5	4.62	7.68	9.38
6	4.73	7.87	9.64
7	4.82	8.07	9.87
8	4.90	8.09	10.03
9	4.97	8.26	10.19
10	5.02	8.37	10.18
11	5.07	8.45	10.29
12	5.12	8.51	10.44
13	5.16	8.59	10.47
14	5.21	8.67	10.59
15	5.24	8.69	10.62

frequencies shift upwards as α is increased. Resonance frequencies for α between 0° and 10° are tabulated in Tab.5.2.

The shift in resonance frequency resulting from unfolding the sheet from its fully folded state ($\alpha = 0^\circ$) to an angle α can be quantified using the formula

$$\delta(\alpha) = \frac{f_r(\alpha) - f_r(\alpha = 0)}{f_r(\alpha = 0)} = \frac{f_r(\alpha)}{f_r(0)} - 1 \quad (5.3)$$

A 2° change in α produces a resonance shift of 28%, a 5° change produces a shift of 45%, and a 10° change produces a shift of 58%. Thus, the upward shift in resonance frequency is quite rapid as the sheet begins to unfold, with the magnitude of the shift tapering off as α increases. The result is a metamaterial that can be tuned mechanically over a wide band of frequencies with only slight physical movement. The principle behind this effect is explored

in the next section.

5.2.3 Principle of operation

The proposed origami-based tunable metamaterial can be broadly tuned with small movements because the resonance frequency of the split-rings is highly sensitive to folding angle when the angle is small. To understand the origin of this effect, recall that the resonance frequency of a set of concentric split rings may be described using a simple series RLC circuit model [80]. Using the circuit shown in Fig.5.18, the resonance frequency is computed using

$$f_r = \frac{1}{2\pi\sqrt{L_{eq}C}} \quad (5.4)$$

For a coplanar SRR, the inductance, L_{eq} , is the inductance of a loop with a radius that is the average of the two rings, $r_0 = R_i + W_g/2$, while the capacitance, C , is due in part to the capacitance between the ring edges and in part to the capacitance of the gaps. Usually, the capacitance of the gaps is neglected, but the presence of the gaps causes the ring edges to act like two capacitors in series, each with the capacitance of a half ring:

$$C = \frac{C_{eq}C_{eq}}{C_{eq} + C_{eq}} = \frac{C_{eq}}{2} \quad (5.5)$$

where

$$C_{eq} = \pi r_0 C_{PUL} \quad (5.6)$$

Here C_{PUL} is the per-unit-length capacitance of the ring pair, which depends on the properties of the dielectric substrate as well as the geometry of the rings. When the rings are used

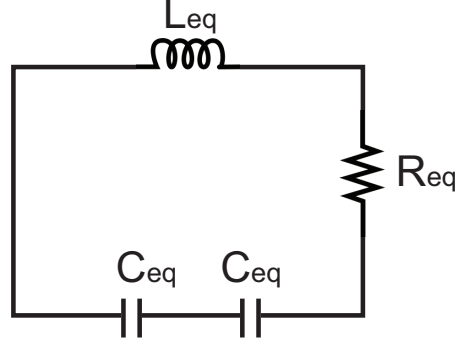


Figure 5.18: Equivalent circuit of an SRR

in the construction of an array of unit cells, Eq.5.4 can be used to compute the resonance frequency of the resulting structure, if the effects of the mutual interaction between the array elements are included.

When the sheet is completely folded ($\alpha = 0^\circ$), each unit cell consists of a set of coplanar rings centrally embedded in a dielectric sheet. Because the capacitance is dominated by the field lines extending between the adjacent edges of the rings, the majority of the electric flux is within the dielectric, and the capacitance of a single set of rings may be approximated by assuming that the rings are embedded in an unbounded dielectric. As the surface is unfolded and the adjacent dielectric sheets move apart, the capacitance changes for two distinct reasons. First, as the coplanar rings separate the capacitance decreases due to both the change in alignment of the adjacent ring surfaces and to the increase in distance between the edges. Second, as the dielectric surfaces unfold, an air gap appears between the surfaces, and the electric flux begins to concentrate in this air gap region. This effect can be seen in Figs.5.19-5.22, which are three-dimensional plots of the electric field strength computed using HFSS for the parameters of Tab.5.1 and a folding angles of $\alpha = 0^\circ$ - 8° . Strong field is shown in red color. The field is clearly strongest in the air region immediately adjacent to rings, at a point 90° from the gaps in the rings. Because the dielectric constant of

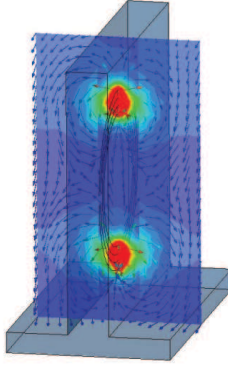


Figure 5.19: Electric field magnitude in one unit cell for $\alpha = 0^\circ$

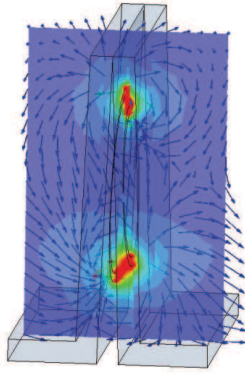


Figure 5.20: Electric field magnitude in one unit cell for $\alpha = 2^\circ$

air is significantly smaller than that of the substrate on which the rings are mounted, the capacitance decreases rapidly as the extent of this region increases. An accurate computation of how this effect compares with the reduction in capacitance due to caused by the increase in distance between the rings requires a full wave simulation of the type already described in Sec.5.2.2. However, it is possible to assess the significance of the contribution of the air gap effect to the tunability of the structure using some simple analysis.

Of predominant importance is the change in resonance frequency with folding angle, described by equation Eq.5.3. Assuming that the inductance is not seriously affected by small changes in α , the change in f_r may be described entirely in terms of the change in capacitance by employing Eq.5.4:

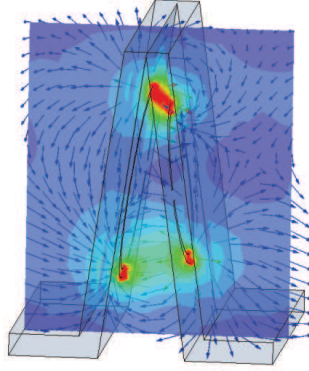


Figure 5.21: Electric field magnitude in one unit cell for $\alpha = 8^\circ$

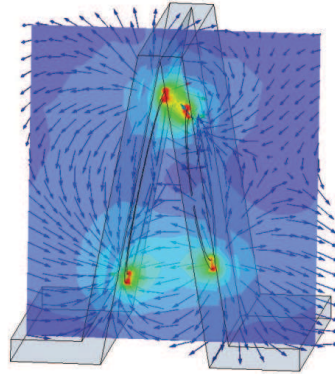


Figure 5.22: Electric field magnitude in one unit cell for $\alpha = 10^\circ$

$$\delta(\alpha) = \sqrt{\frac{C_{eq}(\alpha = 0)}{C_{eq}(\alpha)}} - 1 \quad (5.7)$$

For small folding angles the array effect shouldn't change significantly as α changes, so the change in capacitance can be studied by observing a unit cell. To determine the effect of the ring separation on capacitance, consider a set of concentric rings immersed in an unbounded dielectric. As the rings unfold, an estimate of the capacitance of the inclined rings can be made using the per-unit-length capacitance, C_{PUL} , of the simple canonical structure shown in Fig.5.23. Here two infinite parallel conducting strips of width W_r are offset in both the x and y directions, and C_{PUL} can be computed as a function of Δ and h using simple numerical techniques [81]. Ignoring the slight angle between the strips, the capacitance of each half of the inclined rings shown in Fig.5.24 can be found by assuming that $\Delta = W_r + W_g$ and that C_{PUL} only depends on h :

$$C_{eq}(\alpha) = \int_0^\pi C_{PUL}(h) r_0 d\phi \quad (5.8)$$

where

$$h(\phi, \alpha) = \left[\frac{w}{2} + (2R_o - 2W_r - W_g) \cos \phi \right] \cos \alpha. \quad (5.9)$$

Fig.5.25 shows plots of $\delta(\alpha)$ found using Eq.5.8 in Eq.5.7 for the geometrical parameters in Tab. 5.1. It is seen that as α is increased from zero, $\delta(\alpha)$ increases at a fairly constant rate due to decreasing capacitance. In comparison, when $\delta(\alpha)$ is plotted from Eq.5.3 by using the resonance frequencies from the HFSS simulations described in Section 5.2.2, a much more rapid increase is seen for small α . This suggests that at small folding angles, the decrease in capacitance is dominated by the appearance of the air gap rather than the separation of the

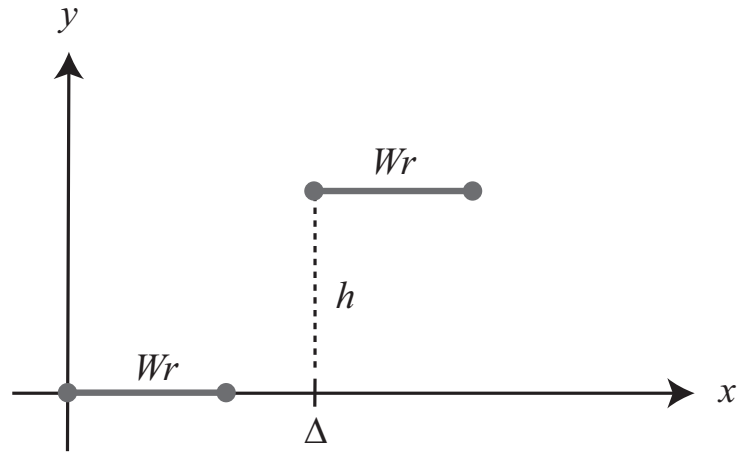


Figure 5.23: Geometry of offset parallel conducting strips

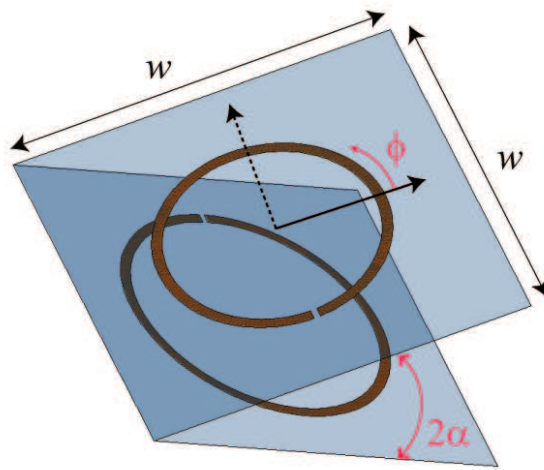


Figure 5.24: Geometry of unfolded origami metamaterial unit cell

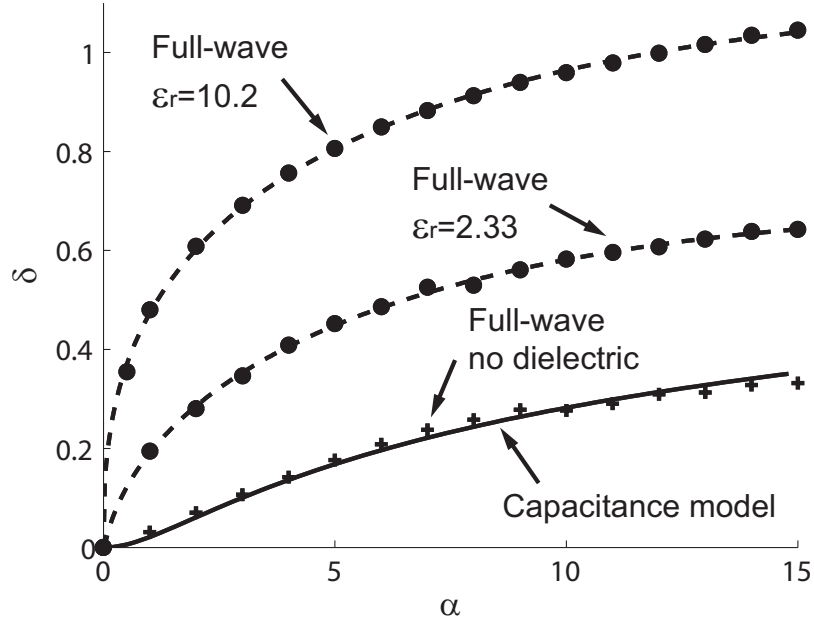


Figure 5.25: Relative change in resonance frequency (dashed curves are best-fit lines)

rings. However, for larger α most of the electric flux resides in the air gap, and thus as α is increased from larger values, the rate of increase in resonance frequency should approach that of two rings separating in free space. Observing the two curves it is seen that the slopes begin to resemble each other as α approaches about 8 degrees. To verify this, the derivative of $\delta(\alpha)$ with respect to α was computed for both the capacitance model and the full-wave analysis by finding the slope of the $\delta(\alpha)$ curves. Because slight variations in the HFSS results preclude using a simple finite-differences derivative, the data was first fit using the empirical model

$$\delta(\alpha) = \sum_{n=1}^4 A_n \alpha^{1/n} \quad (5.10)$$

and then this expression was analytically differentiated. The resulting derivatives are plotted in Fig.5.26. Clearly the relative changes in resonance frequency begin to coalesce above

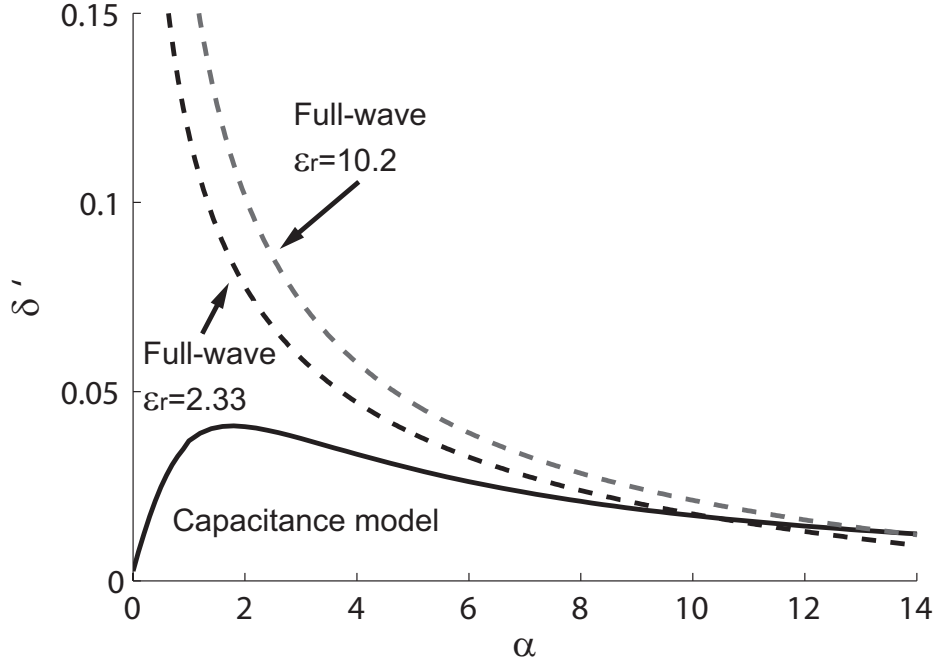


Figure 5.26: Derivative of relative change in resonance frequency

$\alpha = 8^\circ$, and thus above this angle the change in resonance frequency is due primarily to the separation of the rings and not to the increasing air gap.

To study the capacitance effect further, the HFSS simulations were repeated for the same geometrical configuration as shown in Tab.5.1 but with the dielectric parameters of the substrate set first to those of free space ($\epsilon_r = 1$, $\tan \delta = 0$) and then to those of Rogers Duroid 6010 ($\epsilon_r = 10.2$, $\tan \delta = 0.0023$.) The resulting resonance frequencies are shown in Tab.5.2, and $\delta(\alpha)$ found using Eq.5.3 is plotted in Fig.5.25. When the dielectric constant is set to that of free space, the effect of the opening air gap is not present, and the increase in resonance frequency is due entirely to the decrease in capacitance caused by the separation of the rings. The resulting change in resonance frequency, shown as the crosses in Fig.5.25, follows closely that predicted by the capacitance model for rings opening in free space, even though the resonance frequencies found from HFSS with $\epsilon_r = 1$ are significantly

higher than those found by HFSS with $\epsilon_r = 2.33$. This result also validates the assumption that the resonance behavior of the unfolding origami metamaterial array can be deduced by observing a single unit cell, making it easier to devise the experiment described in Sec.5.2.4. Finally, when the dielectric constant is increased to $\epsilon_r = 10.2$ from $\epsilon_r = 2.33$, the contrast between the permittivity of the substrate and that of the air gap that opens as the rings are unfolded increases, and the impact of the opening air gap on the capacitance of the system is magnified. This results in a more rapidly rising value of δ with increasing α at low values of angle, as is clearly seen in Fig.5.25, and a greater overall fractional change in resonance frequency at any value of α . Even so, as with the $\epsilon_r = 2.33$ substrate, the rate of change levels out and becomes the same as two rings opening in free space, as shown in Fig.5.26.

5.2.4 Experiment

An experiment was conducted to test the validity of the design concept. Two copper rings were etched on separate 0.38 mm-thick sheets of Rogers Duroid 5870 (dielectric constant $\epsilon_r = 2.33$ and loss tangent $\tan \delta = 0.0012$) as in Fig.5.27 to form an origami metamaterial unit cell when placed together. The unit cell has dimensions $w = 6.85$, and the etched rings have the geometry values shown in Tab.5.1. The dielectric sheets were glued along an edge to form a hinge, and the sheets were opened to a set angle α by placing a small spacer between the sheets at the open edge. The origami metamaterial unit cell was then placed onto a piece of Styrofoam and inserted into a section of WR-159 F-band (4.90-7.05 GHz) waveguide (Fig.5.28.) The hinge was oriented vertically in the guide so that the horizontal magnetic field of the dominant TE_{10} mode is along the axes of the rings, thus exciting the ring resonance. Finally, the transmission parameters $|S_{21}|$ of the waveguide section

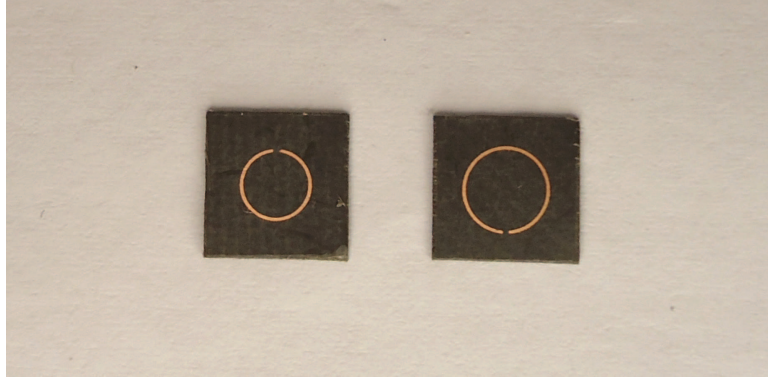


Figure 5.27: Two halves of fabricated origami metamaterial unit cell with the unit cell width $w = 6.85$ mm

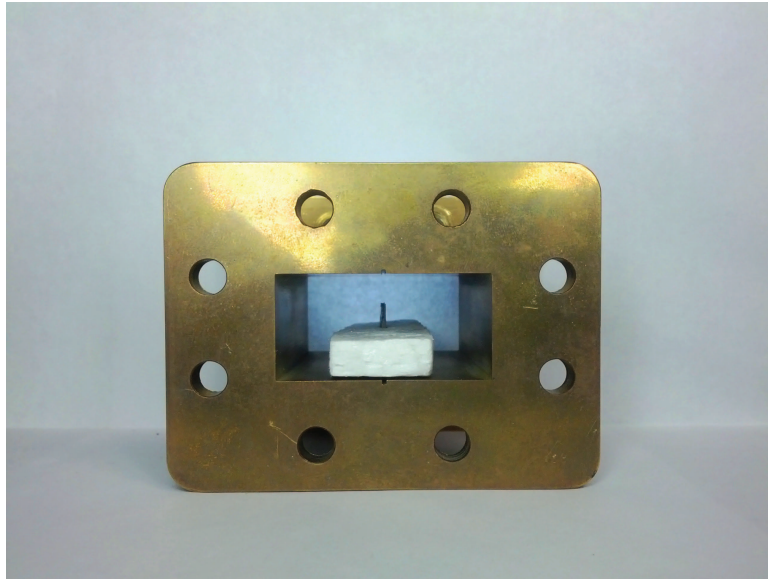


Figure 5.28: Origami metamaterial unit cell placed into an F-band waveguide sample holder

were measured to determine the frequency of resonance. Because the unit cell behaves as a negative permeability metamaterial near resonance, the propagation constant of the dominant mode becomes imaginary and the wave becomes evanescent. Resonance is thus indicated by a stop band with a dip in $|S_{21}|$.

Fig.5.29 shows the measured values of $|S_{21}|$ for several values of folding angle α . It is clearly seen that as the unit cell is unfolded, the resonance frequency quickly increases. A plot of resonance frequency versus α is shown in Fig.5.30, indicating that the resonance

frequency may be shifted across nearly all of F-band with a slight increase in α from 0° to 2° . As a comparison, the unit cell placed into a waveguide with perfectly conducting walls was simulated using HFSS, and values of $|S_{21}|$ are shown for several values of α in Fig.5.31. A similar trend upward in resonance frequency with increasing α may be seen in this figure. The resonance frequencies from the simulations are plotted in Fig.5.30 and compared to the measured resonance frequencies. Interestingly, it appears that the measured resonance frequencies increase with α at a rate even greater than predicted by simulation. This is probably due to a slight unintended gap near the hinge which exists even for very small α . As the sheets are unfolded, this small gap becomes less important compared to the gap opening between the sheets, and the curves agree more closely. The case of $\alpha = 0^\circ$ was measured last, with the two sheets glued together to ensure no gap. At this angle the resonance frequencies from experiment and simulation are nearly identical.

5.2.5 Conclusions

The reflection and transmission characteristics of a corrugated sheet decorated with SRRs were investigated using full-wave simulations. When the folding angle α is increased, resonance is shown to shift rapidly to higher frequencies. A simple analysis reveals that the dominant effect on resonance at small values of α is the decrease in capacitance due to the air gap that opens between the rings as α is increased from zero. Experimental results using a unit cell placed into a waveguide section verify this effect. These results suggest the possibility of tuning folded metamaterial structures using slight mechanical manipulations.

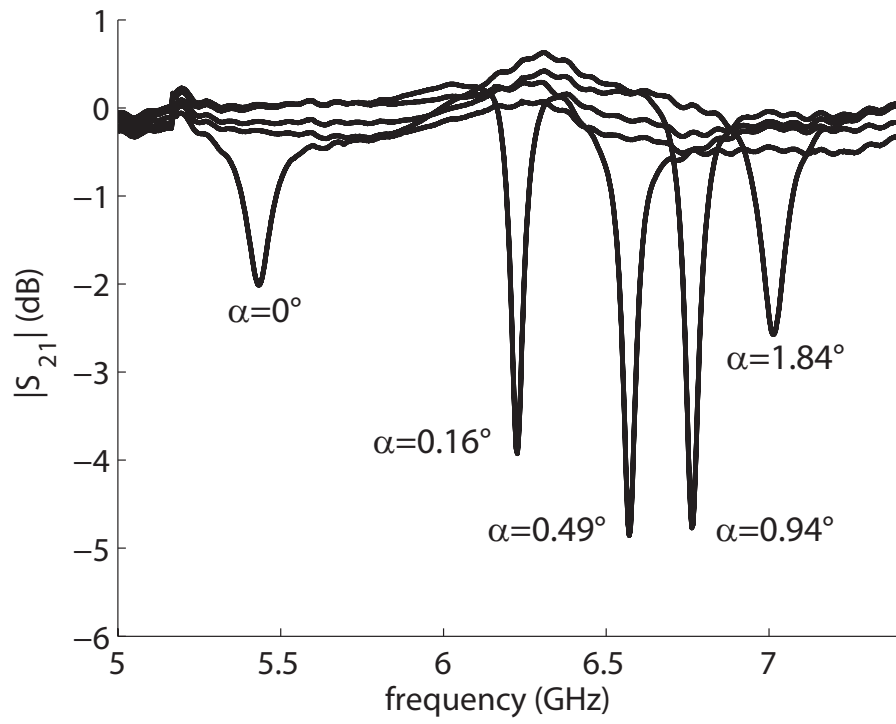


Figure 5.29: Measured transmission coefficients for an origami metamaterial unit cell placed into an F-band waveguide

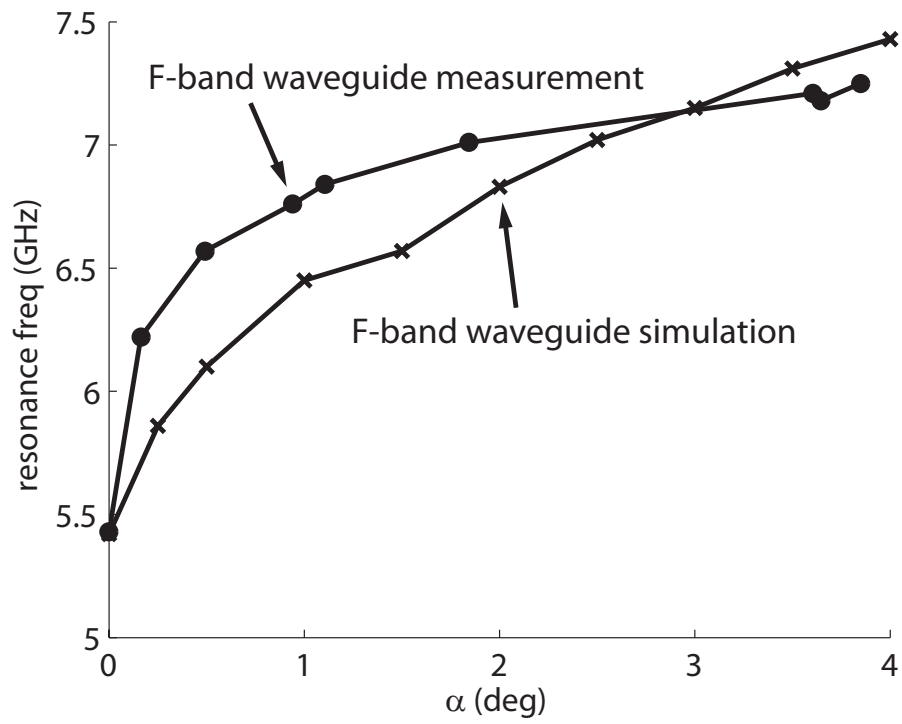


Figure 5.30: Resonance frequency of an origami metamaterial unit cell placed into an F-band waveguide

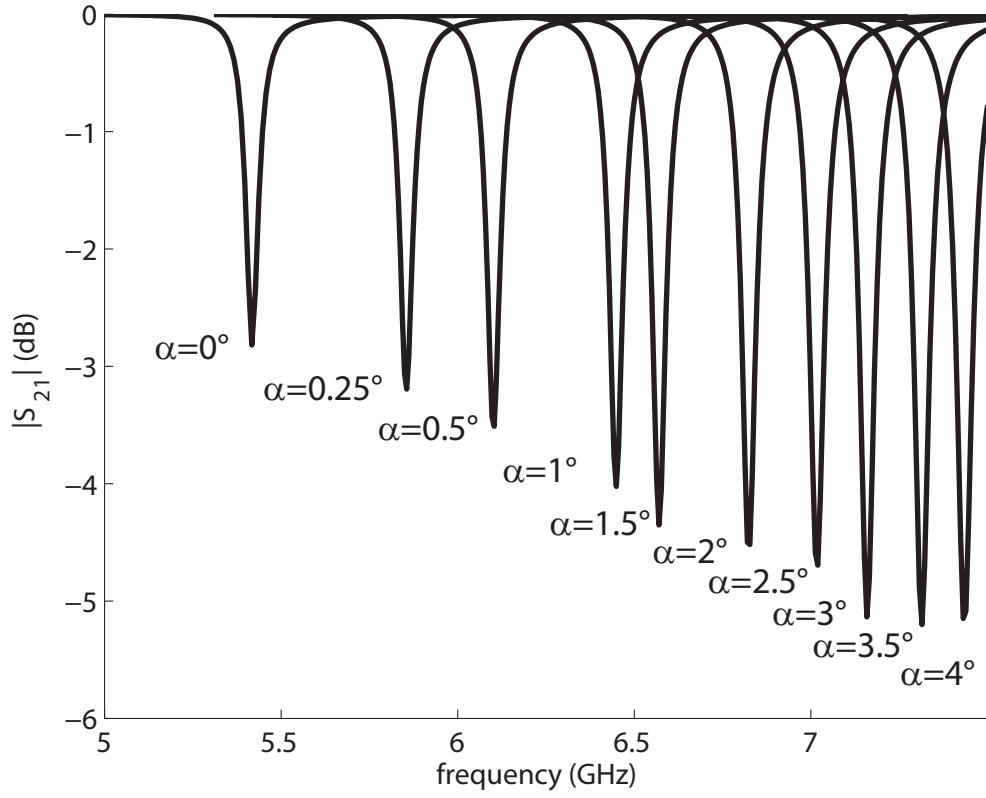


Figure 5.31: Transmission coefficients for an origami metamaterial unit cell placed into an F-band waveguide from HFSS simulations

Chapter 6

Topology Optimization for Origami Design

The use of the folding and unfolding motion of origami for resonance frequency tuning in electromagnetic applications was introduced in chapter 5. In the designs used in chapter 5 and most of other applications of origami in engineering design, such as self-assembly of microdevices such as biomedical devices [82], electronics [83], and microfluidics [84], simple folding patterns with well-known geometric properties are used.

The development of design algorithms and the mathematics of origami in the last two decades allows for systematic design of quite intricate folding patterns [56], [85]-[91]. For example, Lang ([86] [87]) developed a computer program where the origami design is decomposed into two processes: design of a base and design of the complete model. An origami designer draws a stick figure in the program indicating, e.g., the number and lengths of legs. The algorithm then finds a crease pattern that provides the desired base, and the designer completes the design using artistic skills. This is called the tree method. Such methods

are commonly used for art work that may involve very complex geometry. Using a different approach, Tachi [89] [90] developed an origami design method aimed at industrial applications based on tuck-folding. The method systematically finds a folding pattern that follows a prescribed polyhedral surface by tucking some part of the sheet under another to adjust the surface geometry.

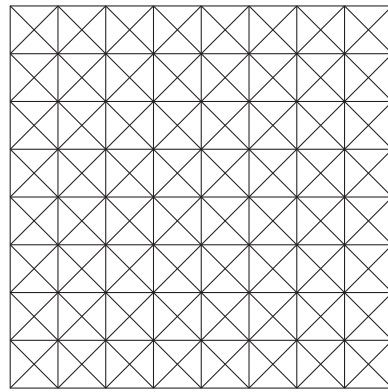
The work presented in this chapter introduces an optimization-based method for origami design. The method used here is similar to an origami design technique that involves the use of a sheet of paper with lines drawn on it. The lines act as a guideline for origami designers to decide where to create folds; some of the lines become folds and some remain flat. The idea is that, if one starts with a sheet with many lines, many different origami designs can be constructed by creating folds along some of those lines. This is analogous to the ground-structure approach to topology optimization of truss structures [92] [93] . The idea there is to start from a ground structure, a potential structure that includes a sufficiently rich set of truss elements, and eliminate unnecessary elements based on an optimization algorithm. In this work we present an origami design counterpart of a ground structure for truss design, constructed by drawing a set of lines on a 2D domain, and an optimization strategy to find patterns with folds along these lines that result in a folded geometry with desirable, target geometric properties. Examples of target properties include a prescribed distance between two points on the sheet and a prescribed angle between two planes, in the folded configuration. Origami designs considered here are restricted to those that may be constructed using only simple folds, namely, those made by folding a sheet along a line to make a mountain or a valley shape. More advanced folding techniques, such as sliding a flap into a pocket, are not considered.

The proposed origami design method can be incorporated into the existing folding design problems such as the design of deployable structures, packaging materials, self-assembled microdevices and dynamically alterable electromagnetic devices to improve their performance. Using sheet materials with customized properties, which may be achieved through the inclusion of nano-particles, the use of the origami design method can be extended to material design, e.g., for the design of thermoelectric materials, membranes, peristaltic porous media, battery or fuel-cell microarchitectures.

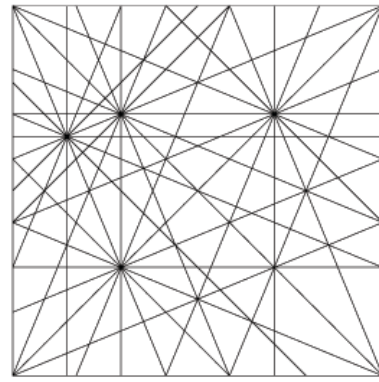
6.1 Construction of the Ground Structure

There are several types of grids traditionally used as a guideline for origami design. One simple example is a square or triangular grid system, used in [94] for design of origami tessellations, formed by a repetition of folded patterns that make up a flat or curved surface. For instance, an origami waterbomb, an example of origami tessellation that follows a curved surface, can be constructed using the triangular grid system shown in Fig.6.1(a). A grid system that results in a more intricate design is the angular grid system studied in [91]. This grid is constructed by drawing lines through reference points, defined as either the corners of the sheet or intersections of lines already drawn. At each reference point, $2n$ lines with a separation angle $90^\circ/n$ are drawn, creating new intersection points. Fig.6.1(b) shows an example of angular grid systems for $n = 4$, where lines at each reference point are drawn 22.5° apart from each other. Maekawa constructed very complex and popular origami designs such as a peacock, a dinosaur and a devil (shown in [95] with instructions), using this type of grid system.

In this work, ground structures similar to those used in structural design are used. A

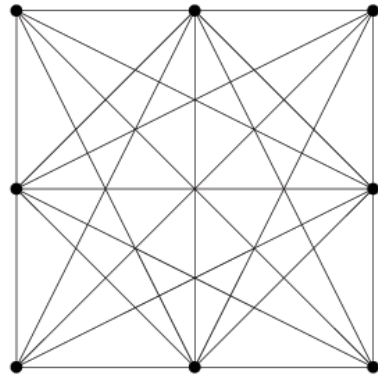


(a) Triangular grid system

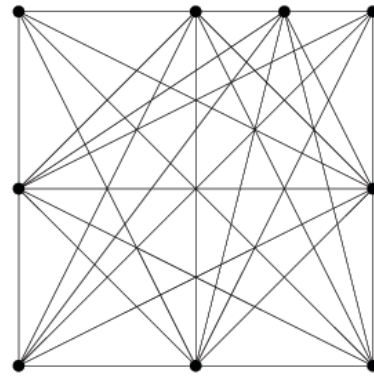


(b) 22.5° grid system

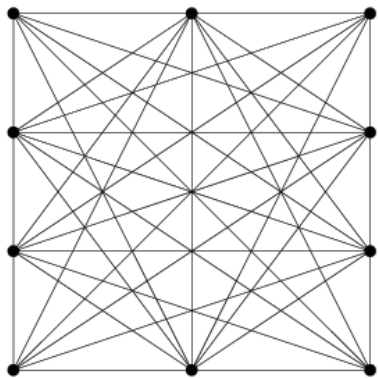
Figure 6.1: Origami grid systems



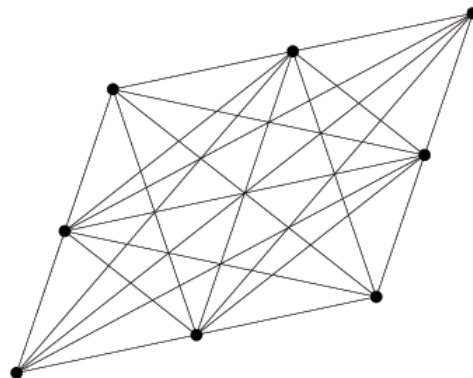
(a)



(b)



(c)



(d)

Figure 6.2: Variations of ground structures

ground structure is constructed by placing points along the boundary of the design domain and drawing connections between all point pairs, creating new vertices at intersections. This is a simple method that provides full control of where vertices appear at the boundary. It is advantageous to have such control for origami design problems where constraints (e.g., periodic boundary conditions for tessellations) are applied at the boundary. Using this technique, one can construct symmetric ground structures such as the one shown in Fig.6.2(a). This structure is appropriate for design of origami tessellations, since it can be tiled in the horizontal and vertical directions with vertices and lines consistent with the periodicity assumption at the boundary. Asymmetric ground structures can be constructed as well, for example, by adding a point to the grid shown in Fig.6.2(a), to construct a structure shown in Fig.6.2(b). The ground structure can be refined to accommodate more complex designs by adding points as in Fig.6.2(c). Ground structures on a non square domain can also be created, as in Fig.6.2(d). Miura-ori, an origami tessellation used for engineering applications in [57][59][96] and several other engineering designs found in literature, can be constructed from the ground structure shown in Fig.6.2(a).

6.2 Crease Type Assignment and a Folded State

Here we consider a rigid origami. A rigid origami is a developable surface made of origami facets and foldlines that can be replaced by rigid panels and hinges, respectively, and can be flattened without distorting the sheet. The model in [88] is used to analyze the geometry of folding patterns in rigid origami. The process of creating a fold in this model can be considered as a rotation of a facet by an angle with respect to its adjacent facet. This angle of rotation is called a folding angle. Fig.6.3(a) shows a circular section of a ground

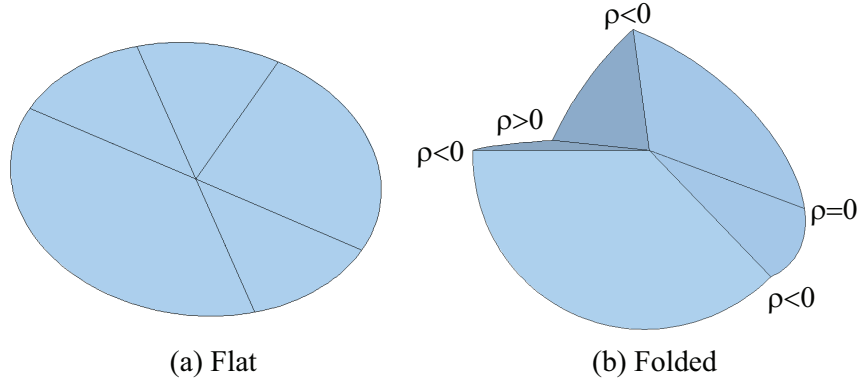


Figure 6.3: Flat and folded states of a single-vertex crease

structure around a vertex, called a single-vertex crease, with $n = 5$ lines extending from it. An example of a folded geometry is shown in Fig.6.3(b) for a given set of $n = 5$ folding angles, denoted ρ . The type of fold at each segment is determined by the value of folding angle: zero, negative and positive folding angles correspond to flat, mountain and valley fold, respectively, as shown in Fig.6.3. Assignment of fold type on the entire domain is done by assigning folding angles to all segments in the ground structure.

The folding angles will be used as design variables to find a folding pattern that meets the target geometric properties. A ground structure with folding angles assigned to all segments represents a folded state: the configuration of the folded geometry of a sheet. One can process information encoded in the folding angles and connectivity of the ground structure to find the geometry of the folded surface. Geometric features relevant to the specific design problem can then be extracted and used within an optimization framework to search for folding patterns with the target properties. The use of continuous variables as design variables allows the use of gradient based optimization algorithms.

6.3 Foldability Conditions

An important constraint in origami design is that the designed pattern is in fact foldable. Necessary conditions for foldable origami design were investigated by belcastro and Hull in [85] and require that the sheet does not stretch or rip during the folding process, and that each face remain flat. The condition to avoid a sheet intersecting itself and penetrating to the other side (self-intersection) is not addressed in [85] (this is still an open problem in origami design). The necessary conditions for foldability in [85] were used to simulate a motion of rigid origami in [88]. A similar approach is used in this work. The foldability condition of a crease around the k^{th} vertex, having n crease lines, is expressed as

$$\mathbf{F}^k(\rho^k, \theta^k) = R\rho_1^k R\theta_1^k R\rho_2^k R\theta_2^k \cdots R\rho_n^k R\theta_n^k = \mathbf{I} \quad (6.1)$$

Matrices $R\theta^k$'s and $R\rho^k$'s are rotation matrices

$$R\theta_i^k = \begin{bmatrix} \cos \theta_i^k & -\sin \theta_i^k & 0 \\ \sin \theta_i^k & \cos \theta_i^k & 0 \\ 0 & 0 & 1 \end{bmatrix} \quad (6.2)$$

$$R\rho_{i;k} = \begin{bmatrix} 1 & 0 & 0 \\ 0 & \cos \rho_i^k & -\sin \rho_i^k \\ 0 & \sin \rho_i^k & \cos \rho_i^k \end{bmatrix} \quad (6.3)$$

and $\{\theta_1^k, \theta_2^k, \dots, \theta_n^k\}$ are angles of rotation about the axis perpendicular to the (flat) sheet, measured between adjacent crease lines, while $\{\rho_1^k, \rho_2^k, \dots, \rho_n^k\}$ are folding angles, as shown

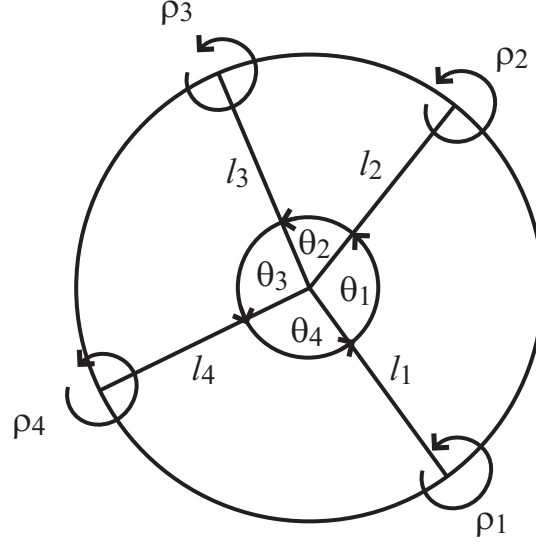


Figure 6.4: Single-vertex crease

in Fig.6.4. For a multi-vertex crease Eq.6.1 has to be satisfied at all vertices $k = 1, 2, \dots, M$, where M is the number of vertices. Note that the notation ρ_i^k refers to the i^{th} crease around vertex k i.e. indexing used in Eq.6.1 is local. It has to be mapped to the global indexing going from 1 to N , where N is the total number of design variables. For design of origami tessellations, foldability conditions for vertices along the edge need to account for crease lines connected to their periodic pairs in neighboring tiles.

6.4 Optimization of Origami Design

The goal of the optimization problem is to find a combination of folding angles that results in a folded state with target geometric properties. Examples of target properties include a prescribed distance between two points on the sheet and a prescribed angle between two planes, in the folded configuration.

6.4.1 Geometric properties

Each geometric property to be controlled is expressed in terms of the coordinates \mathbf{X} of vertices in a folded state as

$$J = J(\mathbf{X}) \quad (6.4)$$

The coordinates \mathbf{X} in a folded state are computed for a given combination of folding angles. For instance, the orientation of the crease line l_2 in a single-vertex crease shown in Fig.6.4 can be found through a rotation of l_1 about the axis of the circle by θ_1 , followed by a rotation about the axis along l_1 by ρ_1 . One can work around one vertex at a time, computing the coordinates of crease ends relative to the vertex. This process can be repeated for all vertices to find \mathbf{X} .

6.4.2 Objective function

A simpler design has fewer foldlines and a larger number of “off” foldlines that remain flat ($\rho = 0$) throughout the folding process. It is our interest to design a folding pattern that achieves the target geometric properties using only a small number of “on” foldlines. This way, any device that is designed based on the folding pattern requires a small number of components and less effort during the fabrication process.

To find folding patterns with a small number of “on” foldlines, one may use in the optimization problem an objective function that favors designs with larger number of “off” foldlines. One such function is f , defined as

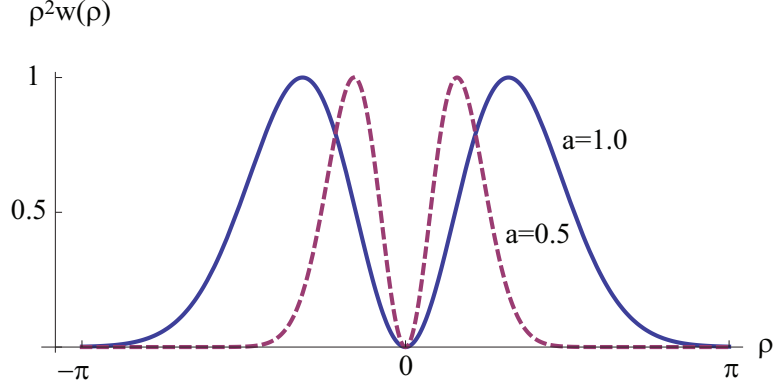


Figure 6.5: Objective function f

$$f = \sum_i \rho_i^2 w(\rho_i) \quad (6.5)$$

Here $w(\rho_i)$ is a weight function that takes the form

$$w(\rho_i) = C e^{-(\rho_i/a)^2} \quad (6.6)$$

with a constant $C = e/a^2$ and a parameter $a \in (0, \infty)$. Curves in Fig.6.5 show $\rho^2 w(\rho)$ for $a = 0.5$ and $a = 1$. As maxima occur at $\rho = \pm a$, their location can be adjusted by choosing a . The objective function penalizes folding angles near $\rho = \pm a$, forcing ρ away from $\pm a$, towards zero or towards larger values.

6.4.3 Optimization problem

If a folding process is considered as a time evolution of geometry of a sheet, an optimal solution should describe the geometry of a folded sheet at one instant during the folding process. To specify the instant at which the geometric properties of a folded sheet are examined, one of the folding angles ρ_r is prescribed to take a fixed value ρ_r^0 , $r \in \{1, 2, \dots, N\}$.

After ρ_r is fixed, the optimization problem is

Optimization Problem P_0^r :

$$\begin{aligned}
& \text{Find} && \rho_i \text{ for } i \in U_0^r \text{ that} \\
& \text{Minimizes} && f(\rho) \\
& \text{Subject to} && \mathbf{g}^k = 0 \quad \text{for } k = 1, 2, \dots, M \\
& && h_i = 0 \quad \text{for } i = 1, 2, \dots, M_{eq} \\
& && -\pi \leq \rho_i \leq \pi \quad \text{for } \forall i \in U_0^r
\end{aligned} \tag{6.7}$$

where $U_0^r = \{1, 2, \dots, N\} \setminus r$ is the set of indices of the free folding angles in P_0^r . In Problem P_0^r ,

- Constraints \mathbf{g}^k express the foldability condition. \mathbf{g}^k is a measure of the deviation of a given design from a foldable design, computed by collecting the three independent components of a 3x3 matrix \mathbf{G}^k as

$$\mathbf{g}^k = \left(\mathbf{G}_{23}^k, \mathbf{G}_{31}^k, \mathbf{G}_{12}^k \right)^T \tag{6.8}$$

where

$$\mathbf{G}_{ij}^k = \frac{1}{2} \left(\mathbf{F}_{ij}^k \left(\rho^{\mathbf{k}}, \theta^{\mathbf{k}} \right) - \mathbf{I}_{ij} \right)^2, \quad i, j = 1, 2, 3 \tag{6.9}$$

- Constraints h_i are used to express how well the design meets a target property J_i .

They are defined by setting

$$h_i = \frac{1}{2} |J_i - J_i^*|^2 \quad (6.10)$$

for each geometric specification J_i and corresponding target value J_i^* .

Clearly, there is no guarantee that a feasible solution to P_0^r exists for a given target property and fixed ground structure. If no feasible solution to P_0^r is found for any fixed angle (r and ρ_r^0), the problem setting must be reconsidered, possibly by modifying the ground structure.

If there is a feasible solution to P_0^r , let ρ^* be the solution. Note that ρ^* may still have many small but nonzero folding angles. A sequence of optimization problems is used to set these angles to zero while retaining foldability.

To find a feasible solution with a reduced number of “on” foldlines near ρ^* , the foldline with the smallest folding angle

$$|\rho_q| = \min_{i \in U_0^r} |\rho_i^*| \quad (6.11)$$

is eliminated. A new set of free folding angles $U_1^r = U_0^r \setminus q$ is defined and ρ_q is set to zero. A new optimization problem is solved, using now the reduced set of design variables. The process is repeated until no feasible solution is found. The p^{th} step in this process solves

Optimization Problem P_p^r :

$$\begin{aligned}
& \text{Find} && \rho_i \text{ for } i \in U_p^r \text{ that} \\
& \text{Minimizes} && f(\rho) \\
& \text{Subject to} && \mathbf{g}^k = 0 \quad \text{for } k = 1, 2, \dots, M \\
& && h_i = 0 \quad \text{for } i = 1, 2, \dots, M_{eq} \\
& && -\pi \leq \rho_i \leq \pi \quad \text{for } \forall i \in U_p^r \\
& && \left| \rho_i - \rho_i^{*p-1} \right| \leq \delta \quad \forall i \in U_p^r
\end{aligned} \tag{6.12}$$

where $U_p^r = U_{p-1}^r \setminus q_{p-1}$ is the set of indices of the free folding angles in P_p^r . Note that an additional constraint $\left| \rho_i - \rho_i^{*p-1} \right| \leq \delta$ has been added to restrict the search within a box of width δ centered at the previous solution ρ^{*p-1} .

If there is no feasible solution to Problem P_p^r , ρ^{*p-1} is a solution to the problem *for the given choice of fixed fold angle ρ_r* . The algorithm is summarized in the flowchart in Fig.6.6.

6.4.4 Sensitivity analysis

To facilitate numerical implementation, gradients based on analytical expressions may be computed and provided to the optimizer. The foldability constraint depends explicitly on folding angle ρ , and the gradients of \mathbf{G}_{ij}^k can be computed as

$$\frac{d\mathbf{G}^k}{d\rho_i^k} = (\mathbf{F}^k - \mathbf{I}) \frac{d\mathbf{F}^k}{d\rho_i^k} = (\mathbf{F}^k - \mathbf{I}) R\rho_1^k R\theta_1^k R\rho_2^k R\theta_2^k \dots \frac{dR\rho_i^k}{d\rho_i^k} R\theta_i^k \dots R\rho_n^k R\theta_n^k \tag{6.13}$$

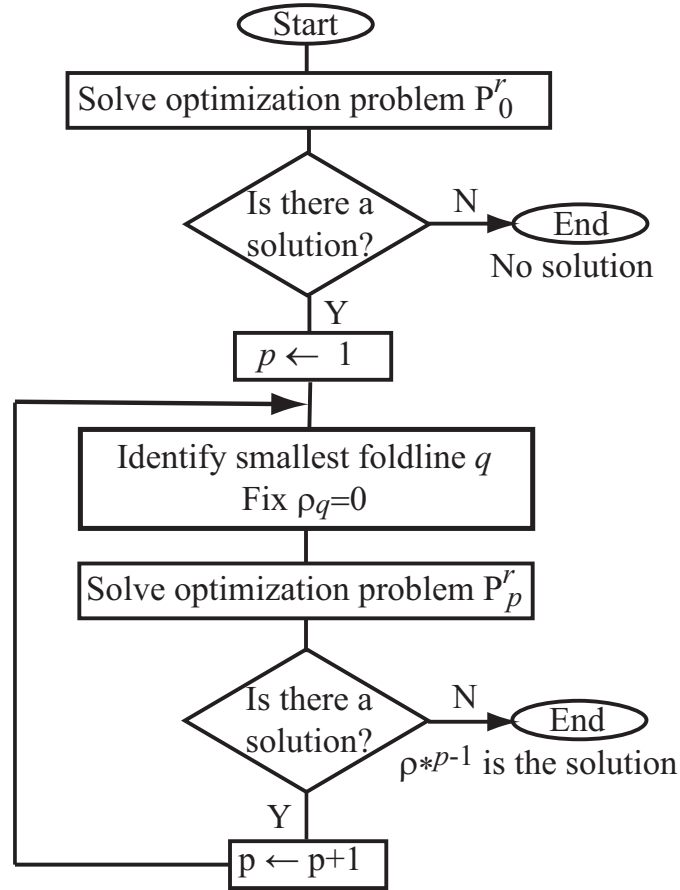


Figure 6.6: Flowchart of foldline elimination algorithm

if the i^{th} crease is connected to the k^{th} vertex and set to 0 otherwise. The constraints h associated with the geometric properties are implicit functions of \mathbf{X} , which depends on ρ . First gradients of vertex coordinates with respect to ρ are computed, then the chain rule is applied to find the gradients of the constraints as

$$\frac{dh}{d\rho_i} = \frac{\partial h}{\partial \mathbf{X}} \frac{d\mathbf{X}}{d\rho_i} \quad (6.14)$$

The gradients of f are

$$\frac{df}{d\rho_i} = \begin{cases} 0 & ; \quad i \notin U_p^r \\ 2Ca^{-2}x \left(a^2 - \rho_i^2 \right) e^{-(\rho_i/a)^2} & ; \quad i \in U_p^r \end{cases} \quad (6.15)$$

6.5 Numerical examples

Two origami tessellations are designed to test the method. The ground structure shown in Fig.6.2(a) with $N = 88$ design variables is used. Note that the periodicity condition requires that folding angles corresponding to foldlines on the right boundary are the same as those on the left boundary, and those on the top boundary are the same as those on the bottom boundary. The number of design variables in this particular ground structure equals the total number of segments minus four. The optimization problem is solved using the interior-point approach described in [97]-[99], implemented in the optimization tool *fmincon* in MATLAB [100].

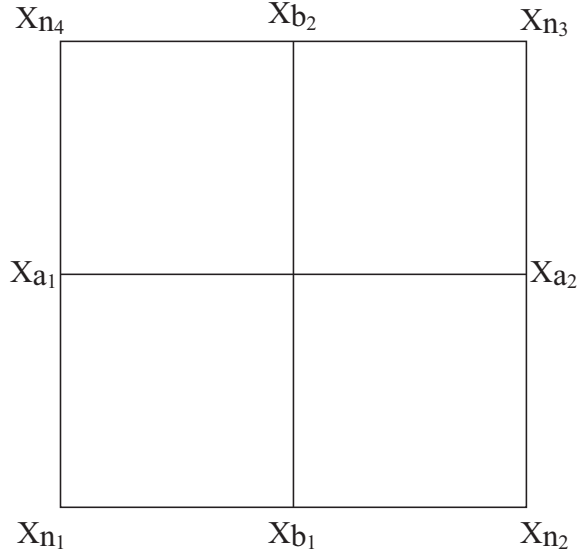


Figure 6.7: Labeled vertices

6.5.1 Example 1

The first example seeks a folding pattern that changes the size of the tessellation tile as it folds, while maintaining the aspect ratio. This property is expressed using

$$J = \frac{1}{2} \left(X_{a_1} - X_{a_2} \right)^T \left(X_{a_1} - X_{a_2} \right) - \frac{1}{2} \left(X_{b_1} - X_{b_2} \right)^T \left(X_{b_1} - X_{b_2} \right) \quad (6.16)$$

with target value $J^* = 0$. The locations of midpoints X_{a_1} , X_{a_2} , X_{b_1} and X_{b_2} in the flat configuration are shown in Fig. 6.7.

A random initial guess ρ_0 with a small magnitude ($< \pi/3000$) is used. The problem is solved multiple times, each time using a different fixed folding angle $\rho_r = \rho_r^0$, choosing r from the segments in Fig.6.8. Due to symmetry, only the 13 segments highlighted in Fig.6.8 need to be investigated.

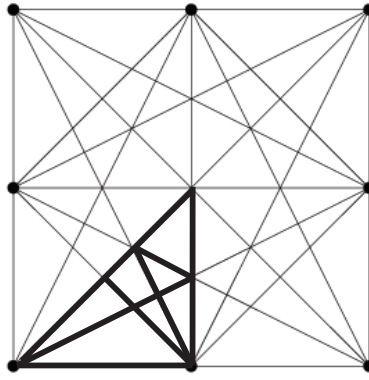
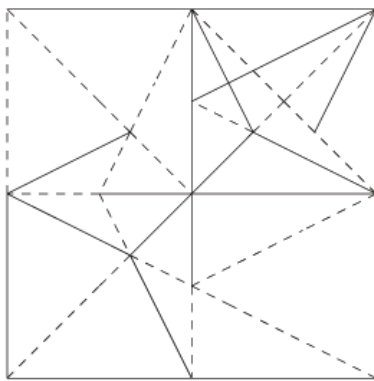
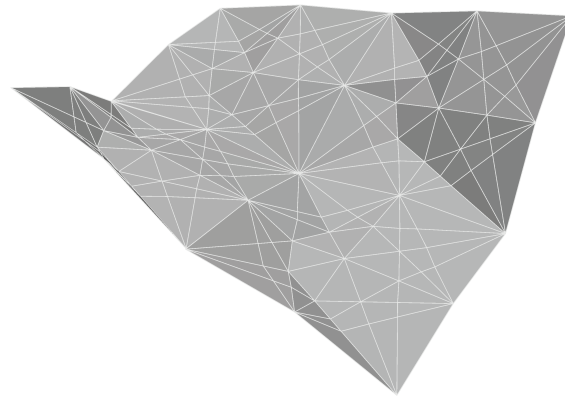


Figure 6.8: Candidates of fixed folding angles

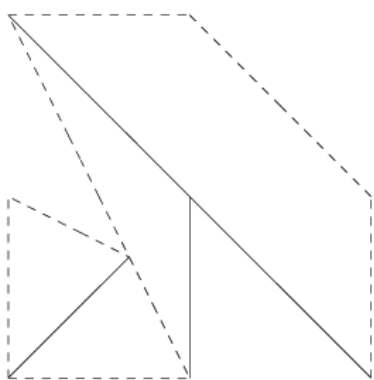


(a) Crease Pattern

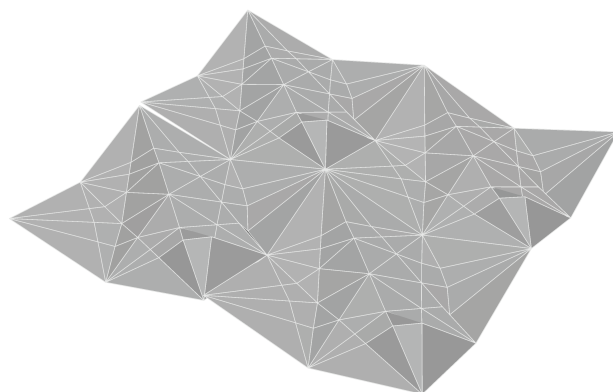


(b) Tessellation

Figure 6.9: Design 1, Example 1



(a) Crease Pattern



(b) Tessellation

Figure 6.10: Design 2, Example 1

Figures 6.9 and 6.10 show crease patterns and folded tessellations corresponding to two of the 13 solutions found, which satisfy constraints \mathbf{g} and h within the specified tolerance $\epsilon = 0.05$. Parameters $a = \pi/4$, $\delta = \pi/12$ and $\rho_r^0 = \pi/4$ are used. The dotted and solid lines in the crease patterns represent mountain and valley folds, respectively.

6.5.2 Example 2

For the second example, additional constraints are used to ensure that the projected shape of the folded sheet follows a flat, square surface. The first geometric property J_1 is the same as before (as in Eq.6.16). To keep the tile shape square,

$$J_2 = \frac{1}{2} \left| \left(X_{a1} - X_{a2} \right)^T \left(X_{b1} - X_{b2} \right) \right|^2 \quad (6.17)$$

should be maintained at $J_2^* = 0$. To design a tessellation that follows a flat surface (non conforming) as it is folded and unfolded, it is also necessary that

$$J_3 = \frac{1}{2} \left\| \frac{(X_{b1} - X_{a1}) \times (X_{b2} - X_{a1})}{|(X_{b1} - X_{a1}) \times (X_{b2} - X_{a1})|} - \frac{(X_{a2} - X_{a1}) \times (X_{b2} - X_{a1})}{|(X_{a2} - X_{a1}) \times (X_{b2} - X_{a1})|} \right\|^2 \quad (6.18)$$

$$J_4 = \frac{1}{2} \left\| X_{a2} - X_{a1} - X_{n2} + X_{n1} \right\|^2 \quad (6.19)$$

$$J_5 = \frac{1}{2} \left\| X_{a2} - X_{a1} - X_{n3} + X_{n4} \right\|^2 \quad (6.20)$$

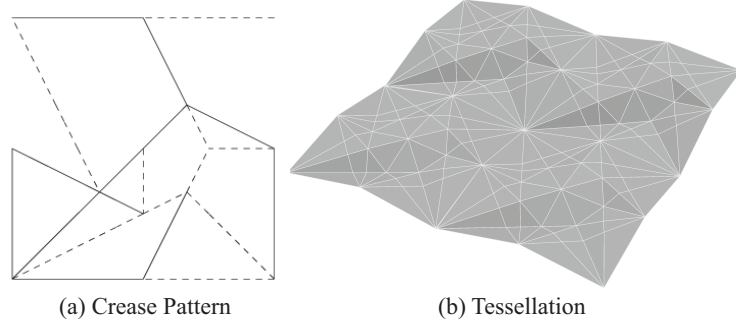


Figure 6.11: Design 1, Example 2

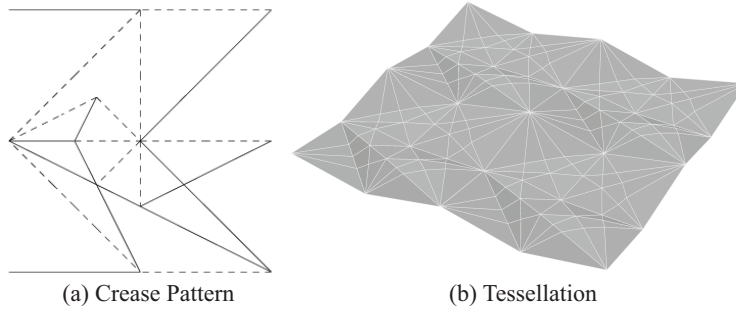


Figure 6.12: Design 2, example 2

$$J_6 = \frac{1}{2} \left\| X_{b2} - X_{b1} - X_{n4} + X_{n1} \right\|^2 \quad (6.21)$$

$$J_7 = \frac{1}{2} \left\| X_{b2} - X_{b1} - X_{n3} + X_{n2} \right\|^2 \quad (6.22)$$

be maintained at $J_3^* = J_4^* = \dots J_7^* = 0$.

Figures 6.11 and 6.12 show crease patterns and folded tessellations corresponding to two of the solutions found, which satisfy the constraints within the specified tolerance $\epsilon = 0.05$ as before.

6.6 Application: design of polarization insensitive tunable FSS

In this section, the usability of the origami design method is demonstrated in an electromagnetic problem. Frequency selective surfaces (FSSs) that can be tuned in frequency based on the folding and unfolding motion are designed. The origami design method is used to design folding patterns that can be used to construct polarization insensitive tunable FSSs. Designs considered are thin substrates decorated with conducting elements and folded into tessellations. The representative unit of periodicity is designed, using appropriate boundary conditions.

The goal of the optimization problem is to find a folding pattern that changes the size of the tessellation tile as it folds, while maintaining the aspect ratio, which correspond to the geometric constraints used in Sec.6.5.2. Two sets of rectangular strips are placed orthogonal to each other on a square sheet of substrate to make a unit cell of an FSS that is symmetric to two orthogonal polarizations as shown in Fig.6.13(a). The mechanism of resonance tuning of the design here is similar to the one used in [59], in which cross-shaped conducting elements are printed on each facet of a substrate folded into Miura-ori, and the change in the length of periodicity as a result of folding shifts the resonance frequency. The main difference is that the design used here is perfectly symmetric for the x - and y -directions in its flat configuration, while in [59] the layout of decoration is asymmetric even in its flat configuration, and thus the FSS's performance dramatically changes for different polarizations. By requiring that the substrate folds in a way that changes the lengths of periodicity in the x - and y -directions by the same amount, the resonance behavior is expected to be nearly symmetric for incidence

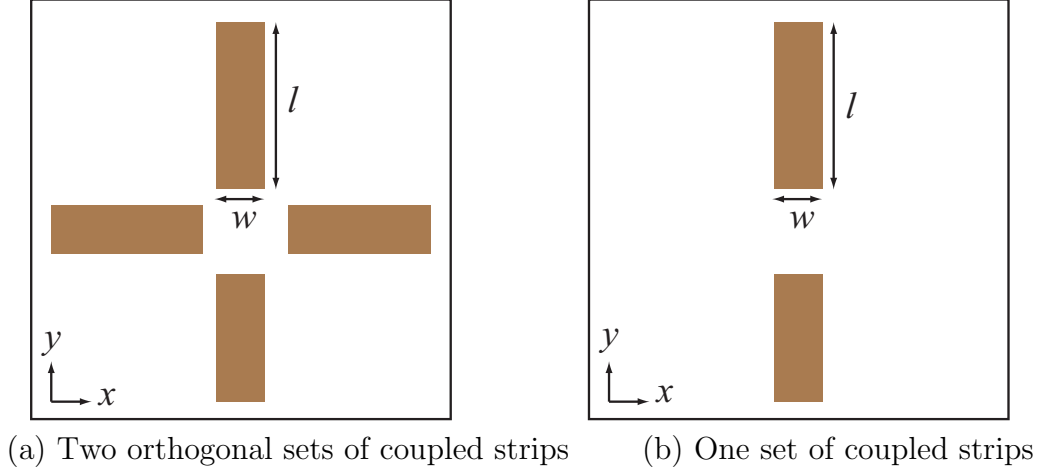


Figure 6.13: Conducting decoration for FSS

with the electric field polarized along both x - and y -directions.

The full evaluation is done by computing the transmission and reflection coefficients using HFSS. In simulations, the tile size in the flat configuration is set to 200mm, and the conducting elements illustrated in Fig.6.13 with $w = 20\text{mm}$ and $l = 120\text{mm}$ and the conductivity of copper are used. Since the strips are larger than the areas of the triangles and quadrilaterals enclosed by lines in the ground structure, the strips will have crease lines through them in the FSS's folded states. The substrate is assumed to be very thin, and the properties of air are used in simulations. A plane wave incidence with the propagation directed normally to the plane of the sheet is used.

Figure 6.14 shows the transmission coefficients $|S_{21}|$ for the polarization-insensitive FSS that satisfies the geometric constraints. The solid and dotted curves show $|S_{21}|$ for the incidence with the electric field polarized along the x -direction in their flat and folded configurations, and circles and squares show the data for the orthogonal polarization where the electric field is in the y -direction. One can observe that the performance is nearly the same for the two orthogonal polarizations. In both polarizations, the resonance shift of 8% - 9%

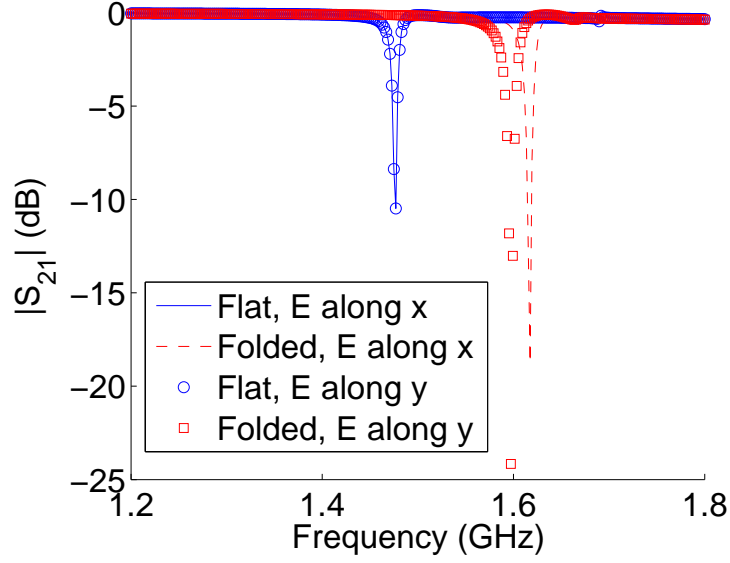


Figure 6.14: Transmission coefficient

is observed, covering nearly the same range of frequencies.

The decoration is designed such that current is induced on the coupled strips along the direction of the electric field with the first resonance occurring near $\lambda/2 = l$, where λ is the vacuum wavelength of the incidence. Strip width w , separation of the elements and the folding pattern will determine the exact location of the resonance. As the sheet is folded, size of the periodic cell decreases by 9%, changing the coupling of elements, resulting in a shift in resonance frequency. A large shift in resonance can be achieved when strips are small compared to the size of the cell, because the change in the cell size is more significant relative to the size of the strips. However, use of very small strips will degrade the strength of the resonance. The decoration was designed in an ad hoc manner based on those considerations, such that a strong resonance with a large shift is achieved.

An alternative design is to use two layers of sheets decorated with one set of strips shown in Fig.6.13(b), rotated 90° from each other. The transmission coefficients are computed for such a design and shown in Fig.6.15. It is seen that the performance is again nearly the

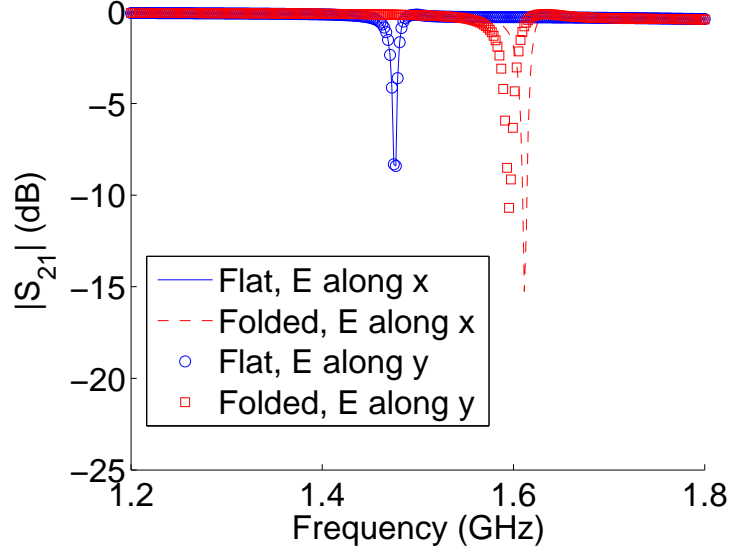


Figure 6.15: Transmission coefficient for the two-layer design

same for the two orthogonal polarizations.

6.7 Conclusions

A method to design origami patterns based on topology optimization is introduced. Folding patterns with desired geometric properties are found by assigning presence and fold types to crease lines in a “ground structure”, using a topology optimization method with folding angles as design variables. Usability of the proposed origami design method is demonstrated in design of tunable FSSs that are insensitive to polarization of the incident electromagnetic wave, which can be tuned in frequency by 8%.

One of the challenges in implementing the origami design method was to eliminate small folds. The technique used in the proposed method involves an objective function designed to aid the selection of a small fold to eliminate. It is required that the optimization problem is solved many times, once after one fold is eliminated. The selection of a proper combination

of unnecessary folds may be made more efficiently through a formulation involving integer programming.

Another potential issue is that for a given set of geometric constraints, an inappropriate choice of the ground structure or the value of the fixed fold may lead to a problem with no feasible solution. In the future work, an investigation of the relation between the existence of a solution for a certain set of geometric constraints and the ground structure, as well as the value of the fixed folding angle is needed.

The usability of the origami design method is demonstrated in an electromagnetic problem, where tunable FSSs based on the folding and unfolding motion are designed. The origami design method is used to design folding patterns that can be used to construct polarization insensitive tunable FSSs.

Chapter 7

Conclusions

In the first part of this dissertation, methods of topology optimization were used to design periodic structures, composed of dielectric materials, with prescribed transmission/reflection characteristics. Two dimensional and three dimensional design problems were solved.

A formulation using the level set function to describe the material distribution was developed for design of 2D structures, in an attempt to develop a formulation that results in solutions with no mixture (gray) regions. In computation, smoothing of the level set function was necessary for a gradient-based optimization algorithm, and in the end solutions still suffered from having mixture regions at interfaces. It was also observed that several parameters affecting the analysis accuracy and optimization algorithm need to be adjusted in an ad hoc manner but with great care to avoid numerical instability. Another formulation based on the density approach was investigated. A rigorous mesh truncation method using a plane wave expansion was applied at the input and output boundaries in this formulation. The solution strategy proposed was stable and robust, and the formulation presented could accommodate complex material distributions near boundaries by including higher modes

into consideration.

A similar formulation based on the density approach was used to design a 3D structure with periodicity in the x - and y -directions. A periodic structure with the material varying in the xy -plane and uniform in the z -direction was considered. A structure that minimizes transmission for an incidence of a prescribed frequency was found. The effective density was projected, using a smooth Heaviside function, to a near binary density in the analysis. It was found that use of the parameter, that adjusts the sharpness of the projection function, needs great care, in order to achieve a fast and stable convergence.

In the second part of this dissertation, a new design method based on topology optimization and the concept of origami was introduced for design of electromagnetic devices involving transformations of complex 3D geometries for tuning of their working frequencies.

First the feasibility of tuning the working frequency of electromagnetic devices via a folding and unfolding motion was demonstrated using two sample designs. An FSS based on a Miura-ori structure with cross-shaped metallic prints was shown to shift its resonance frequency as the folding configuration was altered, mainly due to the change in the periodic cell size. A metamaterial based on a corrugated dielectric sheet decorated with SRRs was also shown to achieve tunability in resonance frequency as an unfolding motion was applied. The two split-rings are arranged vertically on the same plane in the initial configuration, and as an unfolding motion is applied, the planes hosting the rings become separated, shifting the resonance frequency rapidly. A simple analysis revealed that the main cause of the rapid shift was the decrease in capacitance due to the air gap that opened between the split-rings.

A method to design origami patterns based on topology optimization was then introduced. Folding patterns with desired geometric properties were found by assigning presence

and fold types to crease lines in a “ground structure”, using a topology optimization method with folding angles as design variables. Usability of the proposed origami design method was demonstrated in design of tunable FSSs that are insensitive to polarization of the incident electromagnetic wave. An appropriate folding pattern was designed by finding a pattern that changes the size of the tessellation tile as the sheet is folded, while maintaining the aspect ratio. Copper strips were placed symmetrically on the sheet to construct a polarization insensitive tunable FSSs. In the optimization formulation, finding desirable folding patterns without having many small folds was found to be challenging. The proposed method requires that the optimization problem is solved many times in order to avoid many small folds. Development of a more efficient approach for removing unnecessary small folds is needed. Another potential issue with the proposed formulation is that for a given set of geometric constraints, an inappropriate choice of the ground structure or the value of the fixed fold may lead to a problem with no feasible solution. In the future work, investigation of the relation between the existence of a solution for a certain set of geometric constraints and the ground structure, as well as the value of the fixed folding angle is needed.

APPENDICES

Appendix A

Finite Element Equations for 2D

Periodic Structures

The governing equation is the scalar Helmholtz equation in Eq.2.9:

$$\nabla^2 E_z + k_0^2 \epsilon_r E_z = 0 \quad (\text{A.1})$$

The field is assumed to take the form

$$E_z(x, y) = \exp[j\chi_0(y - y_{in})] \exp(-j\alpha_0 x) + \sum_{m=-\infty}^{+\infty} r_m \exp[-j\chi_m(y - y_{in})] \psi_m \quad (\text{A.2})$$

at the input boundary Γ_{in} and

$$E_z(x, y) = \sum_{m=-\infty}^{+\infty} t_m \exp[-j\chi_m(y - y_{in})] \psi_m \quad (\text{A.3})$$

at the output boundary Γ_{out} , where r_m and t_m are modal reflection and transmission

coefficients, respectively, and $\psi_m = \exp(-j\alpha_m x)$. The propagation vector components α_m and χ_m are computed as

$$\alpha_m = \alpha_0 + \frac{2\pi m}{d}$$

and

$$\chi_m = \begin{cases} \sqrt{k_0^2 - \alpha_m^2} & ; \quad k_0^2 - \alpha_m^2 \geq 0 \\ -j\sqrt{\alpha_m^2 - k_0^2} & ; \quad k_0^2 - \alpha_m^2 < 0, \quad m \in \mathbb{Z} \end{cases} \quad (\text{A.4})$$

Consider fields E_z and w that satisfy Bloch-Floquet boundary conditions such that

$$\begin{aligned} E_z &\in S_1 := \{E_z \in H^1(\Omega) : E_z(x + nd, y) = E_z(x, y)e^{-jn\alpha_0 d}\}, \quad n \in \mathbb{Z} \\ w &\in S_2 := \{w \in H^1(\Omega) : w(x + nd, y) = w(x, y)e^{+jn\alpha_0 d}\}, \quad n \in \mathbb{Z} \end{aligned} \quad (\text{A.5})$$

The weak form can be obtained by multiplying both sides by a test function w and integrating as

$$\begin{aligned} &\int_{\Omega} \left(w \nabla^2 E_z + k_0^2 \epsilon_r w E_z \right) d\Omega = 0 \\ \implies &\int_{\Omega} \left(-\nabla w \nabla E_z + k_0^2 \epsilon_r w E_z \right) d\Omega + \int_{\Gamma} \nabla E_z \bullet \hat{n} w d\Gamma = 0 \quad \forall w \in S_2 \end{aligned} \quad (\text{A.6})$$

The boundary terms are

$$\begin{aligned}
\int_{\Gamma} \nabla E_z \bullet \hat{n} w d\Gamma &= \int_{\Gamma_{in}} \nabla E_z \bullet (-\hat{y}) w d\Gamma + \int_{\Gamma_{out}} \nabla E_z \bullet \hat{y} w d\Gamma \\
&+ \int_{\Gamma_a} \nabla E_z \bullet (-\hat{x}) w d\Gamma + \int_{\Gamma_b} \nabla E_z \bullet \hat{x} w d\Gamma
\end{aligned} \tag{A.7}$$

and the terms from the periodic boundaries (Γ_a and Γ_b) vanish as

$$\begin{aligned}
& - \int_{\Gamma_a} \nabla E_z \bullet \hat{x} w d\Gamma + \int_{\Gamma_b} \nabla E_z \bullet \hat{x} w d\Gamma \\
&= - \int_{\Gamma_a} \nabla E_z \bullet \hat{x} w d\Gamma + \int_{\Gamma_a} \exp(+j\alpha_0 d) \exp(-j\alpha_0 d) \nabla E_z \bullet \hat{x} w d\Gamma = 0
\end{aligned} \tag{A.8}$$

since $w|_{\Gamma_b} = \exp(+j\alpha_0 d) w|_{\Gamma_a}$ and $\nabla E_z|_{\Gamma_b} = \exp(-j\alpha_0 d) \nabla E_z|_{\Gamma_a}$.

The term from the input boundary (Γ_{in}) is

$$\int_{\Gamma_{in}} \nabla E_z \bullet (-\hat{y}) w d\Gamma = - \int_{\Gamma_{in}} \frac{\partial E_z}{\partial dy} w d\Gamma = \int_{\Gamma_{in}} \left[j\chi_0 \psi_0 - j \sum_{m=-\infty}^{+\infty} \chi_m r_m \psi_m \right] w d\Gamma \tag{A.9}$$

using Eq.A.2. The term from the output boundary (Γ_{out}) is

$$\int_{\Gamma_{out}} \nabla E_z \bullet \hat{y} w d\Gamma = \int_{\Gamma_{out}} \frac{\partial E_z}{\partial dy} w d\Gamma = \int_{\Gamma_{out}} \left[-j \sum_{m=-\infty}^{+\infty} \chi_m t_m \psi_m \right] w d\Gamma \tag{A.10}$$

using Eq.A.3. Substituting Eq.A.8-A.10 into Eq.A.6, we obtain

$$\begin{aligned}
& \int_{\Omega} (-\nabla E_z(x, y) \bullet \nabla w(x, y) + k_0^2 \epsilon_r E_z(x, y) w(x, y)) d\Omega \\
& - j \sum_{m=-\infty}^{+\infty} \chi_m r_m \int_{\Gamma_{in}} \psi_m(x) w(x, y_{in}) d\Gamma - j \sum_{m=-\infty}^{+\infty} \chi_m t_m \int_{\Gamma_{out}} \psi_m(x) w(x, y_{out}) d\Gamma \\
& = -j \chi_0 \int_{\Gamma_{in}} \psi_0(x) w(x, y_{in}) d\Gamma
\end{aligned} \tag{A.11}$$

Equations for the reflection and transmission coefficients r_m and t_m are obtained by multiplying both sides of Eq.A.2 and A.3 by $\psi_{\tilde{m}}^*$ and integrating as

$$\begin{aligned}
\int_{\Gamma_{in}} E_z \psi_{\tilde{m}}^* d\Gamma &= \int_{\Gamma_{in}} \psi_0 \psi_{\tilde{m}}^* d\Gamma + \sum_{m=-\infty}^{+\infty} r_m \int_{\Gamma_{in}} \psi_m \psi_{\tilde{m}}^* d\Gamma \quad \text{and} \\
\int_{\Gamma_{out}} E_z \psi_{\tilde{m}}^* d\Gamma &= \sum_{m=-\infty}^{+\infty} t_m \int_{\Gamma_{out}} \psi_m \psi_{\tilde{m}}^* d\Gamma
\end{aligned} \tag{A.12}$$

Using the orthogonality relationship

$$\int_{\Gamma} \psi_m \psi_{\tilde{m}}^* d\Gamma = \begin{cases} 0 & ; \quad m \neq \tilde{m} \\ d & ; \quad m = \tilde{m} \end{cases} \tag{A.13}$$

we obtain

$$\begin{aligned}
r_m d - \int_{\Gamma_{in}} E_z(x, y_{in}) \psi_m^*(x) d\Gamma &= -\delta_{0m} d \quad \text{and} \\
t_m d - \int_{\Gamma_{out}} E_z(x, y_{out}) \psi_m^*(x) d\Gamma &= 0
\end{aligned} \tag{A.14}$$

Equations A.11 and A.14 will be discretized, following a finite element formulation with linear rectangular elements, to find an approximate electric field component E_z and reflection and transmission coefficients (r_m and t_m). Using linear shape functions $\{\phi_m\}_{m=1}^{N_n}$, where N_n is the number of degrees of freedom, Eqs.A.11 and A.14 are approximated by finite element equations

$$\mathbf{K}\mathbf{z} = \mathbf{F} \quad (\text{A.15})$$

where $\mathbf{z} = [\mathbf{E}_z, \mathbf{r}, \mathbf{t}]^T$, and $\mathbf{F} = [\mathbf{f}_E, \mathbf{f}_r, \mathbf{0}]^T$ and

$$\mathbf{K} = \begin{bmatrix} \mathbf{K}_{EE} & \mathbf{K}_{Er} & \mathbf{K}_{Et} \\ \mathbf{K}_{rE} & d\mathbf{I} & \mathbf{0} \\ \mathbf{K}_{tE} & \mathbf{0} & d\mathbf{I} \end{bmatrix}$$

$$(\mathbf{K}_{EE})_{sn} = \int_{\Omega} (-(\nabla \phi_n) \cdot (\nabla \tilde{\phi}_s) + k_0^2 \epsilon_r \phi_n \tilde{\phi}_s) d\Omega$$

$$(\mathbf{K}_{Er})_{nm} = -j\chi_m \int_{\Gamma_{in}} \psi_m(x) \tilde{\phi}_n(x, y_{in}) d\Gamma$$

$$(\mathbf{K}_{Et})_{nm} = -j\chi_m \int_{\Gamma_{out}} \psi_m(x) \tilde{\phi}_n(x, y_{out}) d\Gamma$$

$$(\mathbf{K}_{rE})_{mn} = - \int_{\Gamma_{in}} \phi_n(x, y_{in}) \psi_m^*(x) d\Gamma$$

$$(\mathbf{K}_{tE})_{mn} = - \int_{\Gamma_{out}} \phi_n(x, y_{out}) \psi_m^*(x) d\Gamma$$

$$(\mathbf{f}_E)_n = -j\chi_0 \int_{\Gamma_{in}} \psi_0(x) \tilde{\phi}_n(x, y_{in}) d\Gamma$$

$$(\mathbf{f}_r)_m = -\delta_{0m} d$$

where $s, n \in \{-N_n, -N_n+1, \dots, 0, \dots, N_n-1, N_n\}$ and $m \in \{-N_m, -N_m+1, \dots, 0, \dots, N_m-1, N_m\}$. Here ϕ and $\tilde{\phi}$ are bilinear shape functions associated with E_z and w , and the corresponding DOFs on the periodic boundaries at $x = 0$ and $x = d$ are enforced to satisfy conditions $E_z \in S_1$ and $w \in S_2$.

Appendix B

Finite Element Equations for 3D

Periodic Structures

The governing equation is the vector wave equation in Eq.2.7:

$$\nabla \times \left(\frac{1}{\mu_r} \nabla \times \mathbf{E} \right) - k_0^2 \left(\epsilon_r - \frac{j\sigma}{\omega\epsilon_0} \right) \mathbf{E} = 0 \quad (\text{B.1})$$

The electric field is assumed to take the form

$$\begin{aligned} \mathbf{E}(x, y, z) &= \mathbf{E}_{in} + \mathbf{E}_{ref} \\ &= \exp \left\{ -j \left[\alpha_0 x + \beta_0 y + \gamma_0 (z - z_{in}) \right] \right\} \hat{p} \\ &+ \sum_{m=-\infty}^{+\infty} \sum_{n=-\infty}^{+\infty} \mathbf{r}_{mn} \exp \left[j \gamma_{mn} (z - z_{in}) \right] \psi_{mn} \end{aligned} \quad (\text{B.2})$$

at the input boundary Γ_{in} and

$$\begin{aligned}
\mathbf{E}(x, y, z) &= \mathbf{E}_{tr} \\
&= \sum_{m=-\infty}^{+\infty} \sum_{n=-\infty}^{+\infty} \mathbf{t}_{mn} \exp[-j\gamma_{mn}(z - z_{out})] \psi_{mn}
\end{aligned} \tag{B.3}$$

at the output boundary Γ_{out} , where $\psi_{mn} = \exp[-j(\alpha_m x + \beta_n y)]$ and \mathbf{r}_{mn} and \mathbf{t}_{mn} are modal reflection and transmission coefficients that can be computed as:

$$\mathbf{r}_{mn} = \frac{1}{T_x T_y} \int_{\Gamma_{in}} (\mathbf{E}(x, y, z) \psi_{mn}^* - \hat{p} \psi_{00} \psi_{mn}^*) d\Gamma \tag{B.4}$$

and

$$\mathbf{t}_{mn} = \frac{1}{T_x T_y} \int_{\Gamma_{out}} \mathbf{E}(x, y, z) \psi_{mn}^* d\Gamma \tag{B.5}$$

The propagation constant for each mode γ_{mn} can be found by

$$\gamma_{mn} = \begin{cases} \sqrt{k_0^2 - \alpha_m^2 - \beta_n^2} & ; \quad \alpha_m^2 + \beta_n^2 \leq k_0^2 \\ -j\sqrt{\alpha_m^2 + \beta_n^2 - k_0^2} & ; \quad \alpha_m^2 + \beta_n^2 > k_0^2 \end{cases} \tag{B.6}$$

where

$$\begin{aligned}
\alpha_m &= \alpha_0 - \frac{2\pi m}{T_x} \\
\beta_n &= \beta_0 - \frac{2\pi n}{T_y}
\end{aligned} \tag{B.7}$$

Consider fields \mathbf{E} and \mathbf{V} that satisfy Bloch-Floquet boundary conditions such that

$$\begin{aligned}
\mathbf{E} &\in S_1 := \{\mathbf{E} \in H^1(\Omega) : \mathbf{E}(x + mT_x, y + nT_y) \\
&= \mathbf{E}(x, y, z) \exp(-jm\alpha_0 T_x - jn\beta_0 T_y)\}, \quad n, m \in \mathbb{Z} \\
\mathbf{V} &\in S_2 := \{\mathbf{V} \in H^1(\Omega) : \mathbf{V}(x + mT_x, y + nT_y) \\
&= \mathbf{V}(x, y, z) \exp(+jm\alpha_0 T_x + jn\beta_0 T_y)\}, \quad n, m \in \mathbb{Z}
\end{aligned} \tag{B.8}$$

The weak form is obtained through multiplying both sides by a test function \mathbf{V} and integrating as

$$\int_{\Omega} \mathbf{V} \bullet (\nabla \times \frac{1}{\mu_r} \nabla \times \mathbf{E}) d\Omega - \int_{\Omega} k_0^2 \left(\epsilon_r - \frac{j\sigma}{\omega\epsilon_0} \right) \mathbf{V} \bullet \mathbf{E} d\Omega = 0 \quad \forall \mathbf{V} \in S_2 \tag{B.9}$$

This can be organized as

$$\begin{aligned}
&\int_{\Omega} \left[\frac{1}{\mu_r} (\nabla \times \mathbf{V}) \bullet (\nabla \times \mathbf{E}) - k_0^2 \left(\epsilon_r - \frac{j\sigma}{\omega\epsilon_0} \right) \mathbf{V} \bullet \mathbf{E} \right] d\Omega \\
&+ \int_{\Gamma} \frac{1}{\mu_r} \mathbf{V} \bullet (\hat{n} \times \nabla \times \mathbf{E}) d\Gamma = 0 \quad \forall \mathbf{V} \in S_2
\end{aligned} \tag{B.10}$$

using the first vector Green's theorem (see pp. 711 [39]):

$$\int_{\Omega} \mathbf{a} \bullet (\nabla \times u \nabla \times \mathbf{b}) d\Omega = \int_{\Omega} u (\nabla \times \mathbf{a}) \bullet (\nabla \times \mathbf{b}) d\Omega - \int_{\Gamma} u \hat{n} \bullet (\mathbf{a} \times \nabla \times \mathbf{b}) d\Gamma \tag{B.11}$$

and the vector identity

$$\mathbf{a} \bullet (\mathbf{b} \times \mathbf{c}) = -\mathbf{c} \bullet (\mathbf{b} \times \mathbf{a}) \quad (\text{B.12})$$

The boundary terms in Eq.B.10 are

$$\begin{aligned} & \int_{\Gamma} \frac{1}{\mu_r} \hat{n} \bullet (\mathbf{V} \times \nabla \times \mathbf{E}) d\Gamma \\ &= \int_{\Gamma_{left}} \frac{1}{\mu_r} (-\hat{x}) \bullet (\mathbf{V} \times \nabla \times \mathbf{E}) d\Gamma + \int_{\Gamma_{right}} \frac{1}{\mu_r} \hat{x} \bullet (\mathbf{V} \times \nabla \times \mathbf{E}) d\Gamma \\ &+ \int_{\Gamma_{front}} \frac{1}{\mu_r} (-\hat{y}) \bullet (\mathbf{V} \times \nabla \times \mathbf{E}) d\Gamma + \int_{\Gamma_{back}} \frac{1}{\mu_r} \hat{y} \bullet (\mathbf{V} \times \nabla \times \mathbf{E}) d\Gamma \\ &+ \int_{\Gamma_{in}} \frac{1}{\mu_r} (-\hat{z}) \bullet (\mathbf{V} \times \nabla \times \mathbf{E}) d\Gamma + \int_{\Gamma_{out}} \frac{1}{\mu_r} \hat{z} \bullet (\mathbf{V} \times \nabla \times \mathbf{E}) d\Gamma \end{aligned} \quad (\text{B.13})$$

and the terms from the periodic boundaries (Γ_a and Γ_b) vanish, similarly to the 1-D periodicity case. The weak form will then become

$$\begin{aligned} & \int_{\Omega} \left[\frac{1}{\mu_r} (\nabla \times \mathbf{V}) \bullet (\nabla \times \mathbf{E}) - k_0^2 \left(\epsilon_r - \frac{j\sigma}{\omega\epsilon_0} \right) \mathbf{V} \bullet \mathbf{E} \right] d\Omega \\ &+ \int_{\Gamma_{out}} \frac{1}{\mu_r} \mathbf{V} \bullet (\hat{z} \times \nabla \times \mathbf{E}) d\Gamma - \int_{\Gamma_{in}} \frac{1}{\mu_r} \mathbf{V} \bullet (\hat{z} \times \nabla \times \mathbf{E}) d\Gamma = 0 \quad \forall \mathbf{V} \in S_2 \end{aligned} \quad (\text{B.14})$$

The term from the input boundary (Γ_{in}) is

$$\begin{aligned}
& \int_{\Gamma_{in}} \frac{1}{\mu_r} \mathbf{V} \bullet (-\hat{z} \times \nabla \times \mathbf{E}) d\Gamma \\
&= - \int_{\Gamma_{in}} \frac{1}{\mu_r} \mathbf{V} \bullet \hat{z} \times \nabla \times \left(\exp[-j(\alpha_0 x + \beta_0 y + \gamma_0)] \hat{p} + \sum_{m=-\infty}^{+\infty} \sum_{n=-\infty}^{+\infty} \mathbf{r}_{mn} \psi_{mn} \right) d\Gamma \\
&= \sum_{m=-\infty}^{+\infty} \sum_{n=-\infty}^{+\infty} \int_{\Gamma_{in}} \frac{1}{\mu_r} \mathbf{V} \psi_{mn} d\Gamma \bullet \frac{1}{T_x T_y} \hat{z} \times \nabla \times \int_{\Gamma_{in}} \mathbf{E} \psi_{mn}^* d\Gamma \exp[+j\gamma_{mn}(z - z_{in})] \\
&+ \int_{\Gamma_{in}} \frac{1}{\mu_r} \mathbf{V} \bullet \hat{z} \times \nabla \times \{ \exp[-j\gamma_{00}(z - z_{in})] \psi_{00} \hat{p} \} d\Gamma \\
&- \int_{\Gamma_{in}} \frac{1}{\mu_r} \mathbf{V} \bullet \hat{z} \times \nabla \times \{ \exp[+j\gamma_{00}(z - z_{in})] \psi_{00} \hat{p} \} d\Gamma
\end{aligned} \tag{B.15}$$

using Eq.B.2 and B.4.

The term from the output boundary (Γ_{out}) is

$$\begin{aligned}
& \int_{\Gamma_{out}} \frac{1}{\mu_r} \mathbf{V} \bullet (\hat{z} \times \nabla \times \mathbf{E}) d\Gamma \\
&= \int_{\Gamma_{out}} \frac{1}{\mu_r} \mathbf{V} \bullet \left(\hat{z} \times \nabla \times \sum_{m=-\infty}^{+\infty} \sum_{n=-\infty}^{+\infty} \mathbf{t}_{mn} \psi_{mn} \right) d\Gamma \\
&= \sum_{m=-\infty}^{+\infty} \sum_{n=-\infty}^{+\infty} \int_{\Gamma_{out}} \frac{1}{\mu_r} \mathbf{V} \psi_{mn} d\Gamma \bullet \frac{1}{T_x T_y} \hat{z} \times \nabla \times \int_{\Gamma_{out}} \mathbf{E} \psi_{mn}^* d\Gamma \exp[-j\gamma_{mn}(z - z_{out})]
\end{aligned} \tag{B.16}$$

using Eq.B.3 and B.5.

Equation B.14 will be discretized, following a finite element formulation using brick edge elements as in [39], where the electric field components within each element e can be expressed as

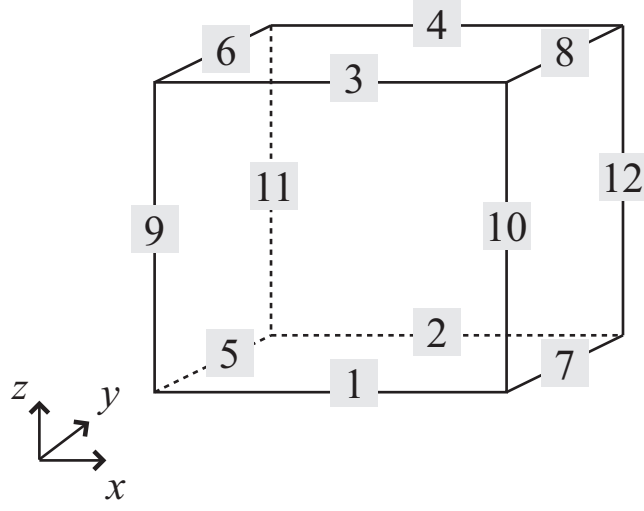


Figure B.1: Brick element

$$E_x^e = \sum_{i=1}^4 \phi_i^e E_i^e, \quad E_y^e = \sum_{i=5}^8 \phi_i^e E_i^e, \quad E_z^e = \sum_{i=9}^{12} \phi_i^e E_i^e \quad (\text{B.17})$$

and ϕ_i is a shape functions that corresponds to the tangential field component along edge i , as numbered in Fig.B.1.

$$\begin{aligned}
\phi_1^e &= \frac{1}{l_y^e l_z^e} \left(y_c^e + \frac{l_y^e}{2} - y \right) \left(z_c^e + \frac{l_z^e}{2} - z \right) \\
\phi_2^e &= \frac{1}{l_y^e l_z^e} \left(-y_c^e + \frac{l_y^e}{2} + y \right) \left(z_c^e + \frac{l_z^e}{2} - z \right) \\
\phi_3^e &= \frac{1}{l_y^e l_z^e} \left(y_c^e + \frac{l_y^e}{2} - y \right) \left(-z_c^e + \frac{l_z^e}{2} + z \right) \\
\phi_4^e &= \frac{1}{l_y^e l_z^e} \left(-y_c^e + \frac{l_y^e}{2} + y \right) \left(-z_c^e + \frac{l_z^e}{2} + z \right) \\
\phi_5^e &= \frac{1}{l_z^e l_x^e} \left(z_c^e + \frac{l_z^e}{2} - z \right) \left(x_c^e + \frac{l_x^e}{2} - x \right) \\
\phi_6^e &= \frac{1}{l_z^e l_x^e} \left(-z_c^e + \frac{l_z^e}{2} + z \right) \left(x_c^e + \frac{l_x^e}{2} - x \right) \\
\phi_7^e &= \frac{1}{l_z^e l_x^e} \left(z_c^e + \frac{l_z^e}{2} - z \right) \left(-x_c^e + \frac{l_x^e}{2} + x \right) \\
\phi_8^e &= \frac{1}{l_z^e l_x^e} \left(-z_c^e + \frac{l_z^e}{2} + z \right) \left(-x_c^e + \frac{l_x^e}{2} + x \right) \\
\phi_9^e &= \frac{1}{l_x^e l_y^e} \left(x_c^e + \frac{l_x^e}{2} - x \right) \left(y_c^e + \frac{l_y^e}{2} - y \right) \\
\phi_{10}^e &= \frac{1}{l_x^e l_y^e} \left(-x_c^e + \frac{l_x^e}{2} + x \right) \left(y_c^e + \frac{l_y^e}{2} - y \right) \\
\phi_{11}^e &= \frac{1}{l_x^e l_y^e} \left(x_c^e + \frac{l_x^e}{2} - x \right) \left(-y_c^e + \frac{l_y^e}{2} + y \right) \\
\phi_{12}^e &= \frac{1}{l_x^e l_y^e} \left(-x_c^e + \frac{l_x^e}{2} + x \right) \left(-y_c^e + \frac{l_y^e}{2} + y \right)
\end{aligned}$$

(B.18)

The finite element equations corresponding to Eq.B.14 are

$$\mathbf{K}\mathbf{E} = \mathbf{F} \quad (\text{B.19})$$

in which the element matrices are

$$\begin{aligned}
K_{ij}^e = & \int_{\Omega^e} \left[\frac{1}{\mu_r} (\nabla \times \tilde{\phi}_i) \bullet (\nabla \times \phi_j) - k_0^2 \left(\epsilon_r - \frac{j\sigma}{\omega\epsilon_0} \right) \tilde{\phi}_i \phi_j \right] \\
& - \sum_{m=-\infty}^{+\infty} \sum_{n=-\infty}^{+\infty} \int_{\Gamma_{in}^e} \frac{1}{\mu_r^e} \tilde{\phi}_i \psi_{mn} d\Gamma \bullet \frac{1}{T_x T_y} \hat{z} \times \nabla \times \int_{\Gamma_{in}^e} \phi_j \psi_{mn}^* d\Gamma \\
& + \sum_{m=-\infty}^{+\infty} \sum_{n=-\infty}^{+\infty} \int_{\Gamma_{out}^e} \frac{1}{\mu_r^e} \tilde{\phi}_i \psi_{mn} d\Gamma \bullet \frac{1}{T_x T_y} \hat{z} \times \nabla \times \int_{\Gamma_{out}^e} \phi_j \psi_{mn}^* d\Gamma \quad (B.20)
\end{aligned}$$

and

$$\begin{aligned}
F_i^e = & \int_{\Gamma_{in}^e} \frac{1}{\mu_r^e} \tilde{\phi}_i^e \bullet \hat{z} \times \nabla \times \left(\exp[-j\gamma_{00}(z-z_{in})] \psi_{00} \hat{p} \right) d\Gamma \\
& - \int_{\Gamma_{in}^e} \frac{1}{\mu_r^e} \tilde{\phi}_i^e \bullet \hat{z} \times \nabla \times \left(\exp[+j\gamma_{00}(z-z_{in})] \psi_{00} \hat{p} \right) d\Gamma \quad (B.21)
\end{aligned}$$

where ϕ and $\tilde{\phi}$ are shape functions associated with the electric field \mathbf{E} and the test function \mathbf{V} , respectively, and the corresponding DOFs on the periodic boundaries are enforced to satisfy the conditions $\mathbf{E} \in S_1$ and $\mathbf{V} \in S_2$.

BIBLIOGRAPHY

BIBLIOGRAPHY

- [1] Bendse M. P. and Kikuchi N. Generating optimal topologies in structural design using a homogenization method. *Computer Methods In Applied Mechanics And Engineering*, Vol. 71, pp. 197-224, 1988.
- [2] Sigmund O. Materials with prescribed constitutive parameters: an inverse homogenization problem. *International Journal of Solids and Structures*, Vol. 31 No. 17, pp. 2313-2339, 1994.
- [3] Bendse M. P. and Sigmund O. *Topology optimization : Theory, Methods, and Applications*. Springer: Berlin, Heidelberg, 2003.
- [4] Sigmund O. and Torquato S. Design of materials with extreme thermal expansion using a three-phase topology optimization method. *Journal of the Mechanics and Physics of Solids*, Vol. 45, No. 6, pp. 1037-1067, 1997.
- [5] Olesen L.H., Okkels F. and Bruus H. Topology optimization of Navier-Stokes flow in microfluidics. *European Congress on Computational Methods in Applied Sciences and Engineering (ECCOMAS 2004)*, Neittaanmaki P., Rossi T., Korotov S., Onate E., Periaux J. and Knorzer D. (eds.) Jyvaskyla, 24-28 July 2004.
- [6] Gersborg-Hansen A., Sigmund O. and Haber R.B. Topology optimization of channel flow problems. *Structural and Multidisciplinary Optimization*, Vol. 30, No. 3, pp. 181-192, 2005.
- [7] Bruns T.E. Topology optimization of convection-dominated, steady-state heat transfer problems. *International Journal of Heat and Mass Transfer*, Vol. 50, No. 15-16, pp. 2859-2873, 2007.
- [8] Wadbro E., Berggren M. Topology optimization of an acoustic horn. *Computer Methods in Applied Mechanics and Engineering*, Vol. 196, No. 1-3, pp. 420-436, 2006.
- [9] Dhring M.B., Jensen J.S., Sigmund O. Acoustic design by topology optimization. *Journal of Sound and Vibration*, Vol. 317, No.3-5, pp. 557-575, 2008.

- [10] Chung Y.S. and Cheon C. Optimal shape design of dielectric structure using FDTD and topology optimization. *Microwave Symposium Digest, 2001 IEEE MTT-S International*, Vol. 3, pp. 2063 - 2066, 2001.
- [11] Kiziltas G., Psychoudakis D., Volakis J. L. and Kikuchi N. Topology design optimization of dielectric substrates for bandwidth improvement of a patch antenna. *IEEE Transactions On Antennas And Propagation*, Vol. 51, No. 10, pp. 2732-2743, 2003.
- [12] Jensen J.S. and Sigmund O. Systematic design of photonic crystal structures using topology optimization: Low-loss waveguide bends. *Applied Physics Letters*, Vol. 84, No. 12, pp. 2022-2024, 2004.
- [13] Borel P.I., Harpoth A., Frandsen L.H., Kristensen M., Shi P., Jensen J.S. and Sigmund O. Topology optimization and fabrication of photonic crystal structures. *Optics Express*, Vol. 12, No. 9, pp. 1996-2001, 2004.
- [14] Jensen J.S. and Sigmund O. Topology optimization of photonic crystal structures: a high-bandwidth low-loss T-junction waveguide. *Journal of the Optical Society of America B*, Vol. 22, No. 6, pp. 1191-1198, 2005.
- [15] Tsuji Y., Hirayama K., Nomura T., Sato K. and Nishiwaki S. Design of optical circuit devices based on topology optimization. *IEEE Photonics Technology Letters*, Vol. 18, No. 5-8, pp. 850-852, 2006.
- [16] Nomura T., Sato K., Taguchi K., Kashiwa T. and Nishiwaki S. Structural topology optimization for the design of broadband dielectric resonator antennas using the finite difference time domain technique. *International Journal for Numerical Methods in Engineering*, Vol. 71, pp. 1261-1296, 2007.
- [17] Sigmund O. and Hougaard K. Geometric properties of optimal photonic crystals. *Physical Review Letters*, Vol. 100, No. 15, pp. 153904, 2008.
- [18] Riishede J. and Sigmund O. Inverse design of dispersion compensating optical fiber using topology optimization. *Journal of the Optical Society of America B*, Vol. 25, No. 1, pp. 88-97, 2008.
- [19] Diaz A.R. and Sigmund O. A topology optimization method for design of negative permeability metamaterials. *Structural and Multidisciplinary Optimization*, Vol. 41, No.2, pp. 163-177, 2009.

- [20] Nomura T., Nishiwaki S., Sato K. and Hirayama K. Topology optimization for the design of periodic microstructures composed of electromagnetic materials. *Finite Elements in Analysis and Design*, Vol. 45, No. 3, pp. 210-226, 2009.
- [21] Fuchi K., Diaz A.R., Yamada T. and Nishiwaki S. A level set-based topology optimization method for power flow control in electromagnetics. *8th Congress on Structural and Multidisciplinary Optimization*, Lisbon, Portugal, 2009.
- [22] Dhring M.B. and Sigmund O. and Feurer T. Design of photonic bandgap fibers by topology optimization. *Journal of the Optical Society of America B*, Vol. 27, No. 1, pp. 51-58, 2010.
- [23] Matzen R., Jensen J.S. and Sigmund O. Topology optimization for transient response of photonic crystal structures. *Journal of the Optical Society of America B*, Vol. 27, No. 10, pp. 2040-2050, 2010.
- [24] Andkjr J., Nishiwaki S., Nomura T. and Sigmund O. Topology optimization of grating couplers for the efficient excitation of surface plasmons. *Journal of the Optical Society of America B*, Vol. 27, No. 9, pp.1828-1832, 2010.
- [25] Aage N., Mortensen N.A. and Sigmund O. Topology optimization of metallic devices for microwave applications. *International Journal for Numerical Methods in Engineering*, Vol. 83, No. 2, pp. 228-248, 2010.
- [26] Erentok A. and Sigmund O. Topology optimization of sub-wavelength antennas. *IEEE Transactions on Antennas and Propagation*, Vol. 59, No. 1, pp. 58-69, 2011.
- [27] Pendry J.B., Holden A.J., Robbins D.J. and Stewart W.J. Magnetism from conductors and enhanced nonlinear phenomena. *IEEE Transactions on Microwave Theory and Techniques*, Vol. 47, No. 11, pp. 2075-2084, 1999.
- [28] Smith D.R., Padilla W.J., Vier D.C.,Nemat-Nasser S.C. and Schultz S. Composite medium with simultaneously negative permeability and permittivity. *Physical Review Letters*, Vol. 84, No. 18, pp. 4184-4187, 2000.
- [29] Shelby R.A., Smith D.R and Schultz S. Experimental Verification of a Negative Index of Refraction. *Science*, Vol. 292, No. 5514, pp. 77-79, 2001.
- [30] Haupt R. L. An introduction to genetic algorithms for electromagnetics. *IEEE Antennas Propagation Magazine*, Vol. 37, pp. 7-15, 1995.

- [31] Ouedraogo R. O., Rothwell E. J. , Diaz A. R., Chen S. Y., Temme A. and Fuchi K. In situ optimization of metamaterial-inspired loop antennas. *IEEE Antennas and Wireless Propagation Letters*, Vol. 9, pp. 75-78, 2010.
- [32] Kern D.J., Werner D.H., Monorchio A., Lanuzza L. and Wilhelm M.J. The design synthesis of multiband artificial magnetic conductors using high impedance frequency selective surfaces. *IEEE Transactions on Antennas and Propagation*, Vol. 53, No. 1, pp. 8-17, 2005.
- [33] Chen C.H., Chen P.Y, Wang H., Tsai J.H. and Ni W.X. Synthesis design of artificial magnetic metamaterials using a genetic algorithm. *Optics Express*, Vol. 16, No. 17, pp. 12806-12818, 2008.
- [34] Bayraktar Z. Gregory M.D., Wang X. and Werner, D.H. Matched impedance thin planar composite magneto-dielectric metasurfaces. *IEEE Transactions on Antennas and Propagation*, Vol. 60, No. 4, pp. 1910-1920, 2012.
- [35] Chung Y.S., Ryu J., Cheon C., Park I.H. and Hahn S.Y. Optimal design method for microwave device using time domain method and design sensitivity analysis - part I: FETD case. *IEEE Transactions on Magnetics*, Vol. 37, No. 5, pp. 3289-3293, 2001.
- [36] Chung Y.S., Cheon C., Park I.H. and Hahn S.Y. Optimal design method for microwave device using time domain method and design sensitivity analysis - part II: FDTD case. *IEEE Transactions on Magnetics*, Vol. 37, No. 5, pp. 3255-3259, 2001.
- [37] Nikolova N.K., Tam H.W. and Bakr M.H. Sensitivity analysis with the FDTD method on structured grids. *IEEE Transactions on Microwave Theory and Techniques*, Vol. 52, No. 4, pp. 1207-1216, 2004.
- [38] Silvester P.P. and Ferrari R.L. *Finite elements for electrical engineers, Third edition*. Cambridge University Press, Cambridge, New York, 1996.
- [39] Jin J. *The finite element method in electromagnetics, Second edition*. IEEE Press, John Wiley & Sons, Inc., Cambridge, New York, 2002.
- [40] Jin J.M. and Riley D.J. *Finite element analysis of antennas and arrays*. IEEE Press, John Wiley & Sons, Inc., Hoboken, 2009.
- [41] Bao G. Finite-element approximation of time-harmonic waves in periodic structures. *SIAM Journal on Numerical Analysis*, Vol. 32, No. 4, pp. 1155-1169, 1995.

- [42] Dossou K., Byrne M.A. and Botten L.C. Finite element computation of grating scattering matrices and application to photonic crystal band calculations. *Journal of Computational Physics*, Vol. 219, No. 1, pp. 120-143, 2006.
- [43] Allaire G., Jouve F. and Toader A.M.. Structural optimization using sensitivity analysis and a level-set method. *Journal of Computational Physics*, Vol. 194, No. 1, pp. 363-393, 2004.
- [44] Wang M.Y., Wang X. and Guo D. A level set method for structural topology optimization. *Computer Methods in Applied Mechanics and Engineering*, Vol. 192, No. 1-2, pp. 227-246, 2003.
- [45] Bourdin B. and Chambolle A. The phase-field method in optimal design. *IUTAM Symposium on Topological Design Optimization of Structures, Machines and Materials: Status and perspectives*, M. P. Bendse, N. Olhoff, and O. Sigmund (Eds.), pp. 207-215, Springer, 2006.
- [46] Comsol: www.comsol.com.
- [47] Sigmund O. and Hougaard K. Geometric properties of optimal photonic crystals. *Physical Review Letters*, Vol. 100, No. 15, pp. 3904, 2008.
- [48] Bendse M.P. Optimal shape design as a material distribution problem. *Structural Optimization*, Vol. 1, No. 4, pp. 193-202, 1990.
- [49] Rozvany G.I.N., Zhou M. and Birker T. Generalized shape optimization without homogenization. *Structural Optimization*, Vol. 4, No. 3-4, pp. 250-252, 1992.
- [50] Mlejnik H.P. and Schirrmacher R. An engineers approach optimal material distribution and shape finding. *Computer Methods in Applied Mechanics and Engineering*, Vol. 106, No. 1-2, pp. 1-26, 1993.
- [51] Svanberg K. The method of moving asymptotes - a new method for structural optimization. *International Journal for Numerical Methods in Engineering*, Vol. 24, No. 2, pp. 359-373, 1987.
- [52] Bruns T.E. and Tortorelli D.A. Topology optimization of non-linear elastic structures and compliant mechanisms. *Computer Methods in Applied Mechanics and Engineering*, Vol. 190, No. 26-27, pp. 3443-3459, 2001.

- [53] Bourdin B. Filters in topology optimization. *International Journal for Numerical Methods in Engineering*, Vol. 50, No. 9, pp. 2143-2158, 2001.
- [54] Sigmund O. Morphology-based black and white filters for topology optimization. *Structural and Multidisciplinary Optimization*, Vol. 33, No. 4-5, pp. 401-424, 2007.
- [55] Wang F., Lazarov B.S. and Sigmund O. On projection methods, convergence and robust formulations in topology optimization. *Structural and Multidisciplinary Optimization*, Vol. 43, No. 6, pp. 767-784, 2011.
- [56] Demaine ED and O'Rourke J. *Geometric folding algorithms: linkages, origami, polyhedra*. Cambridge University Press: New York, 2007.
- [57] Miura K. Method of Packaging and Deployment of Large Membranes in Space. *The institute of space and astronautical science report*, Vol.618, pp. 1-9, 1985.
- [58] Freeland R.E., Bilyeu G.D., Veal G.R. and Mikulas M.M. Inflatable deployable space structures technology summary. *IAF 49th Congress*, Melbourne, Australia, Sep. 1998.
- [59] Fuchi K., Tang J., Crowgey B., Diaz A.R., Rothwell E.J. and Ouedraogo R.O. Origami tunable frequency selective surfaces. *IEEE Antennas and Wireless Propagation Letters*, Vol. 11, pp. 473-475, 2012.
- [60] Fuchi K., Diaz A.R., Rothwell E.J., Ouedraogo R.O. and Tang J. An origami tunable metamaterial. *Journal of Applied Physics*, Vol. 111, No. 084905, 2012.
- [61] Mias C. Varactor-tunable frequency selective surface with resistive-lumped-element biasing grids. *IEEE Microwave and Wireless Components Letters*, Vol.15, pp. 570-572, 2005.
- [62] Schoenlinner B., Abbaspour-Tamijani A., Kempel L.C. and Rebeiz G.M. Switchable low-loss RF MEMS Ka-band frequency-selective surface. *IEEE Transactions on Microwave Theory and Techniques*, Vol. 52, No. 11, pp. 2474-2481, 2004.
- [63] Li M., Yu B. and Behdad N. Liquid Tunable Frequency Selective Surfaces. *IEEE Microwave and Wireless Component Letters*, Vol. 20, No. 8, pp. 423-425, 2010.
- [64] Lima A.C.D., Parker E.A. and Langley R.J. Tunable frequency selective surface using liquid substrates. *Electronics Letters*, Vol. 30, No. 4, pp. 281-282, 1994.
- [65] Bossard J.A., Liang X., Li L., Yun S., Werner D.H., Weiner B., Mayer T.S., Cristman P.E., Diaz A. and Khoo I.C. Tunable frequency selective surfaces and negative-zero-

- positive index metamaterials based on liquid crystals. *IEEE Transactions on Antennas and Propagation*, Vol. 56, No. 5, pp. 1308-1320, 2008.
- [66] Chang T.K., Langley R.J. and Parker E.A. Frequency selective surfaces on biased ferrite substrates. *Electronics Letters*, Vol. 30, No. 15, pp.1193-1194, 1994.
- [67] Bossard J.A., Werner D.H. and Mayer T.S. A novel design methodology for reconfigurable frequency selective surfaces using genetic algorithms. *IEEE Transactions on Antennas and Propagation*, Vol. 53, No.4, pp.1390-1400, 2005.
- [68] HFSS: www.ansys.com.
- [69] Gil I., Garcia-Garcia J., Bonache J., Martin F., Sorolla M. and Marques R. Varactor-loaded split ring resonators for tunable notch filters at microwave frequencies. *Electronics Letters*, Vol. 40, No. 21, pp. 1347-1348, 2004.
- [70] Gil M., Bonache J., Selga J., Garcia-Garcia J. and Martín F. Broadband resonant-type metamaterial transmission lines. *IEEE Microwave and Wireless Components Letters*, Vol. 17, No. 2, pp. 97-99, 2007.
- [71] Aydina K. and Ozbay E. Capacitor loaded split ring resonators as tunable metamaterial components. *Journal of Applied Physics*, Vol. 101, No. 2, pp. 024911-1-024911-5, 2007.
- [72] Li H., Zhang Y. and He L. Tunable filters based on the varactor-loaded split-ring resonant structure coupled to the microstrip line. *Microwave and Millimeter Wave Technology International Conference*, Vol. 3, pp. 1580-1582, 2008.
- [73] Hand T.H. and Cummer S.A. Frequency tunable electromagnetic metamaterial using ferroelectric loaded split rings. *Journal of Applied Physics*, Vol. 103, No. 6, pp. 066105 - 066105-3, 2008.
- [74] Hand T.H. and Cummer S. Controllable magnetic metamaterial using digitally addressable split-ring resonators. *IEEE Antennas and Wireless Propagation Letters*, Vol. 8, pp.262-265, 2009.
- [75] Ouedraogo R.O. *Topology optimization of metamaterials and their applications to RF component design*, (Doctoral dissertation). Michigan State University, East Lansing, MI, 2011.

- [76] Khoo I.C., Werner D.H., Liang X., Diaz A. and Weiner B. Nanosphere dispersed liquid crystals for tunable negative-zero-positive index of refraction in the optical and terahertz regimes. *Optics Letters*, Vol. 31, pp. 2592-2594, 2006.
- [77] Werner D.H., Kwon D.H., Khoo I.C., Kildeshev A.V. and Shalaev V.M. Liquid crystal-clad near-infrared metamaterials with tunable negative -zero-positive refractive indices. *Optics Express*, Vol. 15, pp. 3342-3347, 2007.
- [78] Zhao Q., Kang L., Du B., Li B. and Zhou J. Electrically tunable negative permeability metamaterials based on nematic liquid crystals. *Applied Physics Letters*, Vol. 90, pp. 011112-1 - 011112-3, 2007.
- [79] Khoo I.C., Diaz A., Liou J., Stinger M.V., Huang J. and Ma Y. Liquid crystals tunable optical metamaterials. *IEEE Journal of Selected Topics in Quantum Electronics*, Vol. 16, No. 2, pp. 410-417, 2010.
- [80] Marqués R., Martín F. and Sorolla M. *Metamaterials with negative parameters: theory, design, and microwave applications*, Wiley & Sons, Inc. Hoboken, New Jersey, 2007.
- [81] Harrington R.F. *Field Computation by Moment Methods*, IEEE Press, Piscataway, NJ, 2000.
- [82] Randall C.L., Gultepe E. and Gracias D. Self-folding devices and materials for biomedical applications. *Trends in Biotechnology*, Vol. 30, No. 3, pp. 138-146, 2011.
- [83] Gracias D.H., Tien J., Breen T.L., Hsu C. and Whitesides G.M. Forming electrical networks in three dimensions by self-assembly. *Science*, Vol. 289, No. 5482, pp. 1170-1172, 2000.
- [84] Jamal M., Bassik N., Cho J.H., Randall C.L. and Gracias D.H. Directed growth of fibroblasts into three dimensional micropatterned geometries via self-assembling scaffolds. *Biomaterials*, Vol. 31, No. 7, pp. 1683-1690, 2010.
- [85] belcastro S. and Hull T. Modelling the folding of paper into three dimensions using affine transformations. *Linear Algebra and its Applications*, Vol. 348, pp. 273-282, 2002.
- [86] Lang R.J. The tree method of origami design. In *The Second International Meeting of Origami Science and Scientific Origami*, Miura K (ed). Seian University of Art of Design: Otsu, Japan, pp. 72-82, 1994.

- [87] Lang R.J. Threemaker 4.0: A Program for Origami Design, 1998.
<http://www.langorigami.com/science/computational/treemaker/TreeMkr40.pdf>.
- [88] Tachi T. Simulation of Rigid Origami. In *The Fourth International Conference on Origami in Science, Mathematics, and Education*, Lang R (ed). Pasadena, USA, pp. 175-187, 2009.
- [89] Tachi T. 3D origami design based on tucking molecule. In *The Fourth International Conference on Origami in Science, Mathematics, and Education*, Lang R (ed). Pasadena, USA, pp. 259-272, 2009.
- [90] Tachi T. Origamizing polyhedral surfaces. *IEEE Transactions on Visualization and Computer Graphics*, Vol. 16, No. 2, pp. 298-311, 2010.
- [91] Tachi T. and Demaine E.D. Degenerative Coordinates in 22.5° Grid System, In *The Fifth International Meeting of Origami Science, Mathematics and Education*, Wang-Iverson P, Lang RJ and Yim M (eds). Singapore Management University: Singapore, pp. 489-497, 2010.
- [92] Dorn W.S., Gomory R.E. and Greenberg H.J. Automatic design of optimal structures. *Journal de Mecanique*, Vol 3, No 1, pp. 25-52, 1964.
- [93] Bendse M.P., Bental A. and Zowe J. Optimization methods for truss geometry and topology design. *Structural and Multidisciplinary Optimization*, Vol. 7, No. 3, pp. 141-159, 1994.
- [94] Gjerde E. *Origami Tessellations: Awe-inspiring geometric designs*. A K Peters, Massachusetts, 2008.
- [95] Maekawa J. *Genuine origami: 43 mathematically-based models, from simple to complex*. Japan Publications Trading, Tokyo, 2008.
- [96] Elsayed E.A. and Basily B. A continuous folding process for sheet materials. *International Journal of Materials and Product Technology*, Vol. 21, No. 1/2/3, pp. 217-238, 2004.
- [97] Byrd R.H., Hribar M.E. and Nocedal J. An interior point algorithm for large-scale nonlinear programming. *SIAM Journal on Optimization*, Vol. 9, No. 4, pp. 877-900, 1999.

- [98] Byrd R.H., Gilbert J.C. and Nocedal J. A trust region method based on interior point techniques for nonlinear programming. *Mathematical Programming*, Vol. 89, No. 1, pp. 149-185, 2000.
- [99] Waltz R.A., Morales J.L., Nocedal J. and Orban D. An interior algorithm for nonlinear optimization that combines line search and trust region steps. *Mathematical Programming*, Vol. 107, No. 3, pp. 391-408, 2006.
- [100] MATLAB:www.mathworks.com.